Faculty of Applied Engineering

Bouwkunde

Towards an enhanced understanding of the oxidative ageing mechanisms in bitumen

Thesis submitted for the degree of doctor in Applied Engineering

at University of Antwerp to be defended by

Georgios PIPINTAKOS

Supervisors:

Prof. Dr. Wim Van den bergh

Dr. Hilde Soenen

Antwerp, 2022

Jury

Prof. Dr. Christophe Vande Velde University of Antwerp, Faculty of Applied Engineering, iPRACS research group	**Chair**
Prof. Dr. Wim Van den bergh University of Antwerp, Faculty of Applied Engineering, EMIB research group	**Promotor**
Dr. Hilde Soenen Nynas NV	**Promotor**
Prof. Dr. Evangelos Manthos Aristotle University of Thessaloniki, Department of Civil Engineering, Highway Engineering Laboratory	**Secretary**
Prof. Dr. Sabine Van Doorslaer University of Antwerp, Faculty of Sciences, Bimef research group	**Member**
Prof. Dr. Aikaterini Varveri Delft University of Technology, Civil Engineering and Geosciences, Pavement Engineering research group	**Member**
Prof. Dr. Bernhard Hofko Technical University of Wien, Institute of Transportation, Christian Doppler Laboratory for Chemo-Mechanical Analysis of Bituminous Materials	**Member**
Dr. Xiaohu Lu Nynas AB	**Member**

Contact:
Georgios Pipintakos
University of Antwerp, Faculty of Applied Engineering, EMIB research group
Groenenborgerlaan 171, 2020 Antwerp, Belgium
Email: gpipintakos@gmail.com

ISBN: 9789057287671
Deposit number: D/2022/12.293/37

ISBN 978-9-05-728767-1
9 789057 287671 >

TABLE OF CONTENTS

ABSTRACT

The ageing phenomenon in asphalt and its binding medium, the bitumen, is well documented in the scientific literature with regard to its rheomechanical effects. To understand the 'whys' behind these alterations one should seek additionally on the chemistry of bitumen.

This dissertation supports experimentally the hypothesis of an oxidation scheme consisting of a fast and a slow rate-determining phase. This is achieved by utilising various unmodified bituminous binders of different origin of crude source, refinery process and performance both in oxidation kinetics and with standard lab ageing simulations. The findings of Electron Paramagnetic Resonance (EPR) and Fourier Transform Infrared (FTIR) Spectroscopy manage to distinguish the two phases, while Proton Nuclear Magnetic Resonance (^{1}H-NMR) Spectroscopy and Time-of-Flight Secondary Ion Mass Spectrometry (TOF-SIMS) unravel the main oxygenated products in bitumen. Chemical investigations of the SARA fractions show additionally the effect of ageing on the different fractions. Moreover, each contribution of the coupled reaction-diffusion is studied with FTIR and Dynamic Vapour Sorption (DVS).

Next, the fundamental mechanisms for the development of a peculiar microstructure, the bee structures in bitumen, were explored and validated via Differential Scanning Calorimetry (DSC) and Wide Angle X-ray Diffraction (WAXD). In this dissertation, the hypothesis that the crystallisable compounds in bitumen are the main reason for such structures is adopted, and thus various waxy binders were studied for the effect of lab ageing with Atomic Force Microscopy (AFM) and Confocal Laser Scanning Microscopy (CLSM). Image processing methods allowed to conclude that the bee coverage is reduced upon ageing.

Additionally, the oxygenated products as revealed by the ageing mechanisms in bitumen were linked via multivariate statistics to advanced rheological parameters extracted via the Dynamic shear Rheometer (DSR). Convergence of the fast rate-determining phase and the short-term lab ageing was found both for chemistry and rheology. The dissertation ends with the description of a thermodynamics of irreversible processes model for the fast rate-determining oxidation phase, with the model accounting for reasonable changes of the SARA fractions with oxidation.

All in all, this dissertation provides a deeper scientific insight into the oxidative ageing mechanisms in bitumen and clarifies the relationship between chemical and

rheological characteristics, which may contribute as a guideline to a more sustainable road infrastructure in the future.

SAMENVATTING

Het verouderingsverschijnsel van asfalt en zijn bindmiddel, het bitumen, is heden goed gedocumenteerd in de wetenschappelijke literatuur, met betrekking tot de reomechanische effecten. Om het 'waarom' achter deze veranderingen te begrijpen is aanvullend onderzoek naar de chemie van bitumen noodzakelijk.

Dit proefschrift ondersteunt experimenteel de hypothese van een snel en een traag oxidatieregime. Verschillende ongemodificeerde bitumineuze bindmiddelen zijn onderzocht, verschillend in oorsprong (crude source), raffinageproces en prestaties. Hierbij werden zowel de oxidatiekinetiek als de standaard labverouderingssimulaties toegepast. De bevindingen van Electron Paramagnetic Resosonance (EPR) (EPR) en Fourier Transform Infrared (FTIR) Spectroscopy slagen erin de twee fasen te onderscheiden. De Proton Nuclear Magnetic Resonance (^{1}H-NMR) Spectroscopy en Time-of-Flight Secondary Ion Mass Spectrometry (TOF-SIMS) laten toe om de belangrijkste reactieproducten te ontrafelen. Chemisch onderzoek van de SARA-fracties toont bovendien het effect van veroudering op de verschillende fracties. Daarnaast werd de bijdrage van een gekoppelde reactie-diffusie ook succesvol bestudeerd met FTIR en Dynamic Vapour Sorption (DVS).

De mechanismen voor de ontwikkeling van een bijzondere microstructuur in bitumen, de bijenstructuur (bee-structure), werd onderzocht en gevalideerd met Differential Scanning Calorimetry (DSC) en Wide Angle X-ray Diffraction (WAXD). In dit proefschrift wordt de hypothese aangenomen dat kristalliseerbare verbindingen in bitumen de belangrijkste reden zijn voor dergelijke structuren. Hiervoor werden verschillende washoudende bindmiddelen na verschillende verouderingsprocedures onderzocht met Atomic Force Microscopy (AFM) en Confocal Laser Scanning Microscopy (CLSM). Door middel van beeldverwerkingsmethoden werd aangetoond dat tijdens het verouderingsproces de bijendensititeit vermindert.

Zuurstofhoudende componenten, bepaald via de hierboven chemische testmethoden, konden gekoppeld worden aan reologische parameters, door gebruik te maken van multivariabele statistiek. Convergentie van de snelle reactiefase en de korte termijn veroudering in het labo, werd gevonden voor zowel de chemische als reologische paremeters. Het proefschrift eindigt met een thermodynamisch model, dat rekening houdt met veranderingen van de SARA-fracties tijdens oxidatie, en waarin de verouderingsmechanismen van bitumen voor de snelle reactiestap konden geïmplementeerd worden.

Dit proefschrift geeft een dieper inzicht in de oxidatieve verouderingsmechanismen in bitumen en verduidelijkt de samenhang tussen chemische en reologische kenmerken, wat in de toekomst als een leidraad kan bijdragen tot een duurzamere wegeninfrastructuur.

ACKNOWLEDGEMENTS

During this journey, I see myself like an unmanned ship at the port of Antwerp which needed deck staff to balance, sail and explore the oceans. Luckily, I had two experienced captains with me. Captain Soenen who had fought with big sea monsters (we can call them in our story DSRs and AFMs) and helped the boat to survive by them in each hardship and Admiral Van den bergh. The Admiral became more like a friend as he was affectionate with his boat and took care of it when the weather was bad. It was only then that the boat slowly sailed and passed from the port of Rotterdam where Lieutenant Varveri with pleasure boarded on the ship. She knew this boat as she had assisted in the design of it, in Delft some years ago. The idea of this boat actually was shaped back in Greece thanks to Lieutenant Manthos.

There were people who joined the boat's crew, shared their passion, wisdom and experience and left the boat or watched it sailing from far away. Honourable mention to Commanders Mühlich, Blom, Ching, Lommaert, Tsakalidis and Sjövall. The ship was eventually floating, however, what is a ship without night talks, with a flask of rum, with good friends at the gunwale? Sailors they call them, but actually, these were the most vivid and important to accomplish the mission of this journey. They were literally living inside the boat and giving joyful life to it. Sailors Jacobs, Margaritis, Papini, Hasheminejad, Ghalandari, Pieters, Borinelli, Barisoglu, Barros, Omranian, Hernando, Vuye thank you for your services that reached more than your predefined duties. What can be said also for all those sailors that were telegraphing their best vibes to the boat. The boat is proud to feel the support of Sailors Tziampiris, Chatzistavrou, Kougioumtzi, Gavras, Papathanassi, Karamoschos, Georgiadis, Pantsi, Emmanouilidis, Vasileiadis, Tsikoulas, Papadakis, Teletinis and the Royal Dutch Navy: Tzortzinakis, Mastoras, Presvyri, Papaioanou, Seleridis, Mouratidis. The boat is also grateful for the loyal companion of Comrade Maria that accompanied it almost till the end of its journey. International diplomacy of the boat resulted in some of the strongest alliances with Austria and a network of allies known as the 'Young Ageing Crew'. The boat is more than honoured to have established together with the Shipowners Mirwald, Camargo and Omairey this network.

And the boat from just floating started to sail full speed ahead. Of course, there were tsunamis, hurricanes and storms. Tough winters and summer dryness. The boat would have never managed to kick-off any journey if it was not the family of it that provided all the necessary supplies to be designed. Τουλίτσα και Λεφτεράκο, σας ευχαριστώ και είμαι περήφανος για σας. Circumferential family support to the boat was more than

crucial to complete the journey, as the boat was travelling around the world during these 1720 days. Thank you Warrant Officers Fenia, Nina, Sofie, Christiana, Kostas, Paschalina, Giannis, Kallinikos, Thomy, Vasilis, Efi, Zacharoula and Angelos. Fleet Admirals Efthimia and Giorgos, sincerely thank you and I will always remember you.

And the boat was approaching the end target. It started wondering, as rumours say, is it really the journey that matters or the final destination. Lieutenant Commanders Lu, Van Doorslaer, Hofko and Commander Vande Velde assisted the boat to find the real meaning of its journey.

And the boat arrived. People were waving as it was approaching and cheering with bottoms up. In the end, the boat realised one thing for sure: You can never enjoy the ups and downs of the heavy sea if you do not relax and let yourself being drifted by the flow. Flow is People. People are Flow.

Georgios Pipintakos

Antwerp, December 2022

LIST OF ABBREVIATIONS

1D FFT	One-dimensional Fast Fourier Transform
2D FFT	Two-dimensional Fast Fourier Transform
AFM	Atomic Force Microscopy
AlkP	α-alkyl Protons
ARI	Aromaticity Index
AroP	Aromatic Protons
ATR	Attenuated Total Reflectance
CBOR	Carbon-Based Organic Radicals
CLSM	Confocal Laser Scanning Microscopy
COI	Carbonyl Index
CW	Continuous Wave
DIC	Differential Interference Contrast
DSC	Differential Scanning Calorimetry
DSR	Dynamic Shear Rheometer
DVS	Dynamic Vapour Sorption
EPR	Electron Paramagnetic Resonance
FE	Finite Element
FTIR	Fourier-Transform Infrared spectroscopy
^{1}H-NMR	Proton Nuclear Magnetic Resonance
MetP	Methyl Protons
M-TFO(T)	Modified Thin Film Oven (Test)
MtlP	Methylene Protons
OleP	Olefinic Protons
PAV	Pressure Ageing Vessel
RTFO(T)	Rolling Thin Film Oven (Test)
SANS	Small-Angle Neutron Scattering
SARA	Saturates, Aromatic, Resins, Asphaltenes
SAXS	Small-Angle X-Ray Scattering
SHRP	Strategic Highway Research Program
SOI	Sulfoxide Index
TIP	Thermodynamics of Irreversible Processes
TOF-SIMS	Time-of-Flight Secondary Ion Mass Spectrometry
TTSP	Time-Temperature Superposition Principle
WAXD	Wide Angle X-ray Diffraction

1

INTRODUCTION

1.1 General background

In Belgium, as well as in the major part of the world, private transportation on the mainland is primarily conducted by individuals by making use of asphalt roads. The word 'asphalt' origins from the ancient Greek word 'άσφαλτος' which literally translates to something that cannot fail or collapse. Although asphalt has been invented and intended to be used as an impeccable material, it has been shown that the reality is far from this goal. To construct an asphalt mixture, whatsoever the type is, one needs typically three main components, namely mineral aggregates, filler and bitumen. For example in Belgium the preferred type for surface layers of lower load severity is the asphalt concrete whereas another type, that of stone mastic asphalt, is commonly used for heavily trafficked surface layers. While the asphalt mixture types, differ between them i.e. in terms of air voids content and gradation curves, they all have something in common: the existence of a binder known in European terminology as bitumen. The latter is a material derived from crude oil and acts as the binding medium in asphalt pavements due to its superior viscoelastic, adhesive and water-proofing performance [1]. Recently released data report that 85% of the annual bitumen world production (87 million tons) is used for road paving [2].

The condition of the road network is considered indirectly a metric of the level of society and therefore authorities make significant efforts to keep it to an acceptable degree. This is succeeded, among others, via various efforts to prolong the service life of asphalt pavement and predominantly via a preventive maintenance plan. However, it is often the case in Belgium, as in other developed countries, to face a number of distress types in pavement. Experts have identified the reasons behind certain distresses resulting in the lack of adequate asphalt performance. Some of the most pronounced ones, i.e. block cracking, are related solely to one of the ingredients of

asphalt, the bitumen. As such, bitumen has long been a matter of interest not only for the scientific community but also for the asphalt industry in general since several generated failure types are linked to it.

It all starts from the fact that bitumen is an organic material and that oxygen is omnipresent in the atmosphere. Hence, bituminous binders are composed of a variety of organic molecules consisting of about 85% carbon, 10% hydrogen, heteroatoms such as nitrogen (0-2%), oxygen (0-2%), sulfur (0-9%) and traces of metals such as vanadium, iron and nickel [3,4]. Among the myriad of chemical functional groups of virgin bitumen are the hydroxyl groups of phenols, imino groups of pyrrolic compounds, as well as carbonyl groups of ketones, carboxylic acids and 2-quinolones [5,6]. The lesser amount of heteroatoms in bituminous organic molecules not only modulate the polarity but also constitute chemical functional groups that can react and change. In particular, a wide variety of sulfur-containing compounds occur preferentially within the bituminous binders, such as sulfides, disulfides, sulfoxides, ring compounds (thiophenes, benzothiophenes and dibenzothiophenes) and their alkyl derivatives [7]. Due to its vast number of organic constituents bitumen becomes prone to oxidation during exposure to mixing and environmental conditions [8]. Oxygen, on the other hand, exists in about 21% in the atmospheric air and although essential for the continuity of fauna and flora of earth, in the case of bitumen it results in some irreversible changes.

Albeit other irreversible (volatilisation and condensation), and reversible (physical hardening) physicochemical processes take place in bitumen, the inevitable reaction-diffusion of oxygen in it, widely known as ‘oxidative ageing’, is considered of utmost importance since it generally deteriorates the pavement performance [9,10]. To date, a lot of studies have already demonstrated the negative impact of oxidative ageing resulting in increased brittleness of bitumen, responsible for cracking and ravelling in asphalt scale [6,11–13]. However, it should be noted that moderated ageing may indicate also positive effects on pavement if one is able to control it, i.e. by reducing severe deformations and rutting.

From the combination of the two, the organic nature of bitumen and the atmospheric oxygen, researchers were only able to intervene in the ‘lesser of the two evils’, the bitumen. In parallel, recent literature has shown that other reactive oxygen species in the atmosphere, like ozone and nitrogen oxides, have a strong oxidation potential to bitumen [14,15]. As such, following a brute-force approach, a plethora of additives and rejuvenating agents have been introduced with the potential to improve the bitumen’s performance or to compensate for certain irreversible chemical alterations [16,17]. Hitherto, a number of studies stressed that chemistry and microstructure may be the

key element to unwrap the association of ageing with the bitumen's performance [6,18–22] and the necessity to bridge the different scales, from molecular to nano-, micro- and further to meso- and macroscale [23–25]. However, this proved to be far from an easy-going task since the bitumen's exact composition depends on the refinery process, the origin of crude oil and additionally alters with ageing, a fact that makes the unboxing of this complex organic blend even more challenging [26,27].

1.2 Theoretical background

1.2.1 *Hypotheses of the ageing mechanisms in bitumen*

The unravelling of the underlying mechanisms of oxidative ageing has been a tedious task already from the 1960s. The scientific community, historically, turned from studies into isothermal oxidation kinetics to efforts to simulate the in-situ ageing in the lab and, later, to an incorporation of various antioxidants which were believed to prohibit the process of autoxidation as the binder reacts with oxygen, generating new compounds that may continue to react with oxygen [18]. It has been concluded that a thorough understanding of the oxidation products and the effect of oxygen on fundamental bitumen properties is of paramount importance. As a result of this acknowledgement, there is an increasing interest over the past decade back to the investigation of the bitumen's ageing mechanisms in order to tackle once and for all the precedential uncertainties [28–30].

With regard to the hypotheses of the underlying mechanisms, independent studies support that during the ageing process, the active functionalities of bitumen molecules are decomposed through the oxidative dehydrogenation of polycyclic perhydroaromatics generating intermediate hydroperoxides [31,32]. Through the years, different mechanisms have been proposed to describe this phenomenon ranging from an oxycyclic reaction mechanism [33] up to a dual sequential binder oxidation scheme [6,34]. According to the latter, two major oxidation phases may exist, namely the chemically distinct and rate-determining "fast-spurt" and "slow/long-term" [18,19,34,35]. The existence of free radicals during this dual-oxidation route will most likely provoke the chemical reactions resulting eventually in the formation of polar sulfoxides from non-polar sulfides and polar ketones (as well as anhydrides and carboxylic acids in smaller amounts) from benzylic carbon moieties [9]. This idea has gained considerable support since a direct link with the asphalt production stages can be established [36].

Previous kinetic studies have revealed also differences in the reaction rate and the formation of the two major oxidation products, namely carbonyls and sulfoxides [35]. It has been reported that the higher temperature during short-term ageing, in the production stage, has a stronger effect on the intensity of oxygenated products than the lower average temperature during long-term ageing, in service life [37,38]. Moreover, the literature emphasises that an increase of 10 °C may double the reaction rate and a relatively high temperature (above 120 °C) may cause thermal decomposition of the sulfoxides [34,39]. In reality, the temperature varies between the different stages of the service life; when open to traffic, extreme temperatures greater than 80 °C are never reached, while the temperatures during the paving stages depend on the asphalt mixture application (hot, warm, cold).

In order to mimic such in-situ changes of bitumen due to oxidation, a common practice is to utilise routine tests simulating the short- and long-term ageing. More specifically, the Rolling Thin-Film Oven Test (RTFOT) [40] followed by the Pressure Ageing Vessel (PAV) [41] are most commonly used to mimic the elevated temperature during production and paving and the weather conditions during use-life respectively. According to literature conditioning in PAV of 20 hours at a pressure of 2.1 MPa corresponds to 7-10 years of field ageing [42–44], where the exact equivalence depends on the bitumen and type of the asphalt mixture. It is still a matter of debate if these standardised protocols simulate in a similar manner the ageing in-situ, not only in terms of performance but also in terms of chemistry, as other factors i.e. humidity, ultraviolet light, reactive oxygen species may affect additionally the reaction routes [14]. Of pragmatic importance is to examine whether the artificial ageing simulations, widely used in the asphalt sector, account for a fair correspondence with the ageing mechanisms and products, reported previously as hypotheses in kinetic studies [19,35]. However, it appears that experimental validation of the underlying mechanisms has been confined primarily to sulfoxide and carbonyl formation. As such, considerable research has been devoted to the determination of these functional groups via chemical analysis such as Fourier-Transform Infrared (FTIR) spectroscopy [37,45,46].

When it comes to a classification of bitumen, a rather simplistic approach is to characterise bitumen's composition based on solubility classes, by utilising appropriate solvents. This technique was introduced already in the 1970s [47] and is known nowadays as the SARA fractionation due to the four main derived solubility-based categories, namely Saturates, Aromatics, Resins and Asphaltenes. Different techniques have been proposed for this classification, which can also result in slight differences even for the same bituminous samples [48,49]. Many studies have highlighted that,

due to ageing, bitumen exhibits a shift of these fractions from aromatics to resins and finally to asphaltenes, whereas saturates are considered in general unreactive when employing their relative content [20,24,42,50,51]. Moreover, asphaltenes are considered the largest and most polar constituents which account primarily for the overall bitumen's viscosity [52,53], while in the literature they have been also reported to precipitate in n-heptane because of their strong dispersive π-π interactions [53]. In the past, resins were believed to contribute as a stabilising medium in bitumen, by means of asphaltenes micelles surrounded by them [52,54]. Challenges mainly arise when specific products of the hypotheses proposed so far for the ageing mechanisms are needed to be confirmed experimentally and additionally in the way that these products are distributed within the SARA fractions.

1.2.2 *Hypotheses of the bitumen's structure*

In order to understand better the molecular associations of bitumen, researchers have extensively brainstormed over the years both with regard to the internal structure of bitumen at nanoscale level, but also for the microstructure (surface and bulk) of it at microscale level.

Already in the dawn of the 20th century, a *colloidal structure model* for the intrinsic architecture of bitumen was proposed [55], with more detailed descriptions of this assumption documented by Nellensteyn a decade later [56]. The latter study supported that asphaltenes constitute a colloidal suspension together with the maltenes, which consists of aromatics, resins and saturates, while resins play a stabilising role in bitumen [57]. This idea was developed further based on the association with the rheological response which was believed to vary between sol binders (Newtonian behaviour) and non-linear gel ones (non-Newtonian behaviour), while most of the bituminous binders behave in a situation between the two cases [58,59]. The difference between the two extrema was attributed to the interconnectivity of the asphaltenes micelles in the gel phase, whereas the full dispersion and successively lack of interaction of the asphaltenes micelles was responsible for a sol type of bitumen's structure. The intermediate situation implied the co-existence of the two phases [58]. Relationships between the different colloid types in bitumen and the ratio of asphaltenes and saturates content over the sum of resins and aromatics have been established, to characterise bitumen's colloidal stability [60].

The main opponents of the colloidal model argued already in the 1990s that bitumen is a purely homogeneous fluid known as *dispersed polar fluid*, which gave its name to

this theory concerning the intrinsic architecture of bitumen [61–63]. The main argumentation in disregarding the colloidal theory was generated around the lack of an elastic plateau for the gel binders [52] and the lack of a thermodynamic basis for the separation of bitumen in different phases. More specifically, an assumed phase separation would reduce the system's entropy and would require an enthalpy compensation which is in contradiction to the micelle theory where asphaltenes are considered to be gathered. In the homogeneous fluid theory, the bitumen molecules are considered to be in a mutual solution including a range of solubility parameters in such a way that everything can be kept soluble. Additionally, the supporters of the dispersed fluid theory believed that the monotonic time dependence and the unimodal relaxation spectrum with regard to the viscoelastic response of bitumen were the basis to support such a homogeneous theory.

The most recent colloid theories, known as the *Yen-Mullins model*, support that asphaltenes play a dominant role as 'island' structures in the molecular architecture of crude oils and therefore also of bitumen [64,65]. Asphaltenes are believed to appear in 'islands' which in sufficient concentration can form near-spherical nanoaggregates, consisting of six to ten molecules stacked together followed by clustering in higher concentration [65,66]. Validation of such disk-shaped, core-shell nano-sized structures for the asphaltene nanoaggregates has also been provided experimentally with advanced techniques of Small-Angle Neutron Scattering (SANS) and Small-Angle X-Ray Scattering (SAXS) [67].

On bitumen surfaces, on the other hand, micro-sized, wave-like, rippled patterns have been observed utilising different microscopic techniques [68,69]. These were referred by Loeber and his peers as bee structures [70], and have been a matter of debate in the research community concerning their origin and the underlying mechanisms. It has long been considered that the bee-like structures are related to the asphaltene fraction of bitumen [71], whereas other studies attribute their formation to a crystallisation of the waxy components in bitumen [72–75]. Little research, however, has been devoted to microstructural patterns observed in the bulk of the bitumen, mainly studied in fractured bituminous samples. In these fracture surfaces, bee structures were able to be captured only upon reheating [76].

Concerning the wax theory for the mechanisms behind the bee structure formation, bitumen, apart from the solubility-driven SARA fractions, can include another crystallisable fraction. This crystallisable fraction may be present in the heavy crudes used to process bitumen or it may be generated during certain refinery procedures i.e. visbreaking or hydrocracking in the type of paraffinic or microcrystalline wax [77–79]. Typically, paraffinic waxes consist of linear n-alkanes, while microcrystalline wax is

made up of aliphatic hydrocarbons with a considerable amount of iso- and cycloparaffins [4]. The paraffinic waxes crystallise upon cooling in large, thin, flat plates (macrocrystalline waxes) while the microcrystalline waxes form small micrometre-sized crystals. Differences between the two wax types are observed in the molecular weight and the boiling temperatures; microcrystalline waxes have a higher molecular weight and boiling range [80]. Past studies have also reported different geometries, shapes and sizes (1-10 μm) for the formed crystals [81,82].

In practice, Differential Scanning Calorimetry (DSC) is used as an effective tool to determine the presence and properties of crystalline waxes, including glass transitions, exo- and endothermic phenomena [74,83]. Alternative tools able to complementarily provide deeper insights into the wax crystallinity exist but are rather uncommon for bitumen. For example, ^{13}C Nuclear Magnetic Resonance and Gas Chromatography combined with Mass Spectrometry have hardly been used to characterise the presence of crystallinity in bitumen [77].

1.2.3 *Chemistry and performance of bitumen*

Bitumen has generated much interest in the scientific community in an effort to understand better its performance from different physicochemical and mechanical perspectives [53,84]. Previous research has also stressed the importance of bitumen's chemistry for its performance [10,18,85].

The studies presented so far provide evidence that the ageing-produced ketones and carboxylic acids are of high polarity, generating strong associations, expressed through their Van der Waals forces. Subsequently, the polar compounds of bitumen may interact with each other [86]. Possible chemical changes could induce stronger interactions and change the bitumen structure which may have implications for the mechanical behaviour. Given this, there is a growing body of evidence that an increase in apparent molecular weight due to increased molecular interactions can reduce the mobility of molecules to flow which, in turn, will influence the bitumen rheology [10,87–89].

There is also a widespread recognition that the severity of ageing can be tracked by capturing the change in certain functional groups [10,36,45,46,88]. Nevertheless, it remains an open question whether the fundamental chemistry and rheology in bitumen are affected at a similar level by oxidative ageing. Thus, many studies have focused on the association between simply derived FTIR ageing indices which represent the oxygenated functional groups, i.e. carbonyls, and parameters essential for workability, such as viscosity, taking into account the ageing effect [5,6]. Similar

efforts have been undertaken to link other cumulative FTIR ageing indices, i.e. sulfoxides and carbonyls, with more sophisticated rheological indices derived with a Dynamic Shear Rheometer (DSR), accounting for a single frequency or the whole range of frequencies in the area under a rheological master curve [90,91]. In parallel, other works have utilised the same techniques for differentiating the effects of different long-term protocols in corresponding ageing parameters [92].

In addition, empirical parameters i.e. penetration and softening point, have their merits but reach their limitations, when dealing with modified or special binders containing additives and/or extenders, and thus are no longer considered to be the best performance indicators [93]. Instead, advanced rheological parameters have been introduced in the last decades, which not only are associated with basic bitumen concepts, such as ductility and relaxation but also with distress phenomena and concepts of durability, rutting and thermal-cracking [16,84,93–96]. It appears that in order to examine the correspondence of the intensity of the ageing products and the simultaneous evolution of advanced rheological indices, extensive fundamental information of chemistry is needed besides the oxygenated FTIR functional groups. Of particular complexity is to incorporate fundamental products, i.e. the free radicals, which have been assumed to play a crucial role in the hypotheses for the mechanisms of a potential ageing scheme [18,97]. One able to implement in a scheme such factors will have at least a fair overview of the bitumen's chemistry so that controlled conclusions can be drawn for the corresponding changes of rheology.

When it comes to the effect of the SARA fractions in performance, via a systematic blending of them it has been demonstrated that asphaltenes are primarily responsible for the high viscosities and the non-Newtonian rheological properties of bitumen [18,98]. By remixing different weight ratios of the asphaltenes and the maltenes obtained from different source bitumen, the binders' characteristic microstructures have been found to correlate well with their bulk thermal and mechanical properties [99]. It has also been shown that, among different fractions, asphaltenes display the lowest temperature susceptibility [98,100,101], and significantly contribute to bitumen's stiffness, rigidity, and elasticity [27,85,102]. On the other hand, for a better fatigue resistance, limiting the content of asphaltenes in bitumen would be rather beneficial [103]. In a study conducted during the Strategic Highway Research Program (SHRP), the thickening effect of asphaltenes has been examined in a set of bitumen produced from different crude oils using different techniques [104]. By defining a relative viscosity of bitumen as the quotient of the viscosity of the whole bitumen divided by the viscosity of the maltene fraction at a given temperature and rate of shear, the compatibility of the bitumen could be assessed. Evidently, a deep

understanding of asphaltenes and maltenes is essential to additionally establish the relationships between bitumen chemistry and rheology.

Finally, the crystallisable compounds are of utmost importance to be investigated not only for scientific reasons. From a practical point of view, in crude oils, the presence of wax may relate to undesirable effects such as precipitation and pipe plugging or deposition problems, depending on the applied temperature and pressure [105]. In bitumen, the presence of waxes affects, among other properties, the stiffness at low service temperatures which can induce slow hardening, increasing the risk for low-temperature cracking at the corresponding asphalt mixtures. On the other extreme, at high service temperatures, waxes in bitumen may result in additional softening, which increases the risk of permanent deformation [106–109]. These indicate the importance of wax crystallinity and knowledge of the melting and crystallisation temperatures in bitumen.

1.3 **Problem statement**

Following the fast-evolving technological and environmental trends, the alarming need for designing more sustainable and durable structures, including roads, has led towards an attitude to prolong the lifetime of materials and improve their composition in order to resist the majority of the possible deteriorative mechanisms. Furthermore, as bitumen is a non-renewable organic material, a disciplined usage is required against its depletion which is stimulated additionally due to ageing. However, a thorough understanding of the fundamental mechanisms governing bitumen's chemistry and performance is still missing and hypotheses are yet to be reviewed and validated.

An improved, in-depth knowledge of bitumen oxidation is considered crucial for reviewing the protocols for artificial lab ageing in order to adapt them in a controlled manner. In addition, acquiring this knowledge may be the key answer to intervene into bitumen's composition more systematically in the near future i.e. via targeted modifications which will prohibit certain oxidation paths of ageing and by implementing more appropriate modifiers or rejuvenators when recycling in order to reverse certain performance characteristics. In parallel, the underlying mechanisms controlling the surface microstructure in bitumen have been confined to single ambient temperature observations by limited techniques, while a real-time evolution of microstructure is still missing. In addition, the effect of oxidative ageing on the microstructure is often contradictory in the literature and it is limited in human-based interpretations.

Currently, a comprehensive and mechanism-based approach for modelling the multiphysics ageing process in bitumen is not available. Existing efforts to model oxidative ageing focus either on particular aspects at certain scales or employ a purely phenomenological approach aiming to capture the entire process over all scales, without accounting for compositional changes. Meanwhile, the scientific community has not yet understood and implemented completely the basics of bitumen in such phenomenological models in order to make the correct decisions that are of paramount importance for the final output of interest, the performance of it.

1.4 Research objectives and scope

Hence, the scope of the current research project is to design a useful handbook for every stakeholder dealing with bitumen and is interested in exploring the 'why' behind certain changes related to ageing and the microstructure of bitumen which have a direct effect on its behaviour.

Contrary to the brute-force approaches used up to now in the literature the methodology adopted in this doctoral dissertation initiates from the molecular level and scales up to the microscale of bitumen (Figure 1-1). More specifically, this research project investigated and attempted to give answers to a series of unexplored, conflicting and open questions that exist in the literature up to this moment.

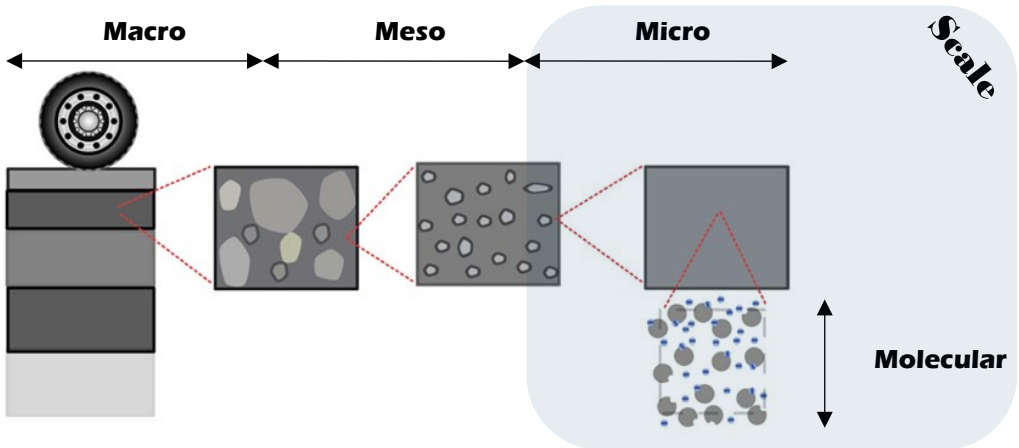

Figure 1-1 The hierarchical scales of asphalt ageing

The main objectives of this dissertation are summarised herein.

1. It attempts to employ a number of state-of-the-art experimental techniques as the ground truth of the hypotheses proposed so far for the ageing

phenomenon in oxidation kinetics and also by utilising standardised lab ageing simulations.

2. Via ageing kinetics, it estimates fundamental properties of the coupled contributions of reaction and diffusion of oxygen in bitumen.
3. It aims to investigate how the polarity-based fractions of bitumen are chemically affected upon ageing.
4. The dissertation discusses the main oxygenated products in bituminous binders accounting for variability between the selected materials in terms of type, refinery process and origin.
5. It provides support for the mechanisms of the bitumen's microstructure and offers a sophisticated way to comprehensively evaluate the effect of ageing on certain morphological patterns.
6. This thesis seeks to elucidate the influence of different laboratory ageing protocols on chemistry and rheology and to provide a framework to link them.
7. After reviewing the ageing mechanisms, efforts to implement this compositional information in a mechanism-based model accounting for diffusivity and reaction completion time, are undertaken.

1.5 Research outline

The dissertation is outlined in nine Chapters, while the content of the thesis conceptually is distinguished into five main parts. All of them are illustrated schematically in Figure 1-2. Part I introduces the reader to the topic and the problem statement of this work (Chapter 1) and it provides the research methodology used in this study versus the possible obtained results (Chapter 2).

In part II, the main laboratory oxidation products for a variety of conventional bituminous binders differing considerably in terms of origin, distillation process and composition are explored in Chapters 3 and 4 by FTIR, Electron Paramagnetic Resonance (EPR), Time-of-Flight Secondary Ion Mass Spectrometry (TOF-SIMS) and Proton Nuclear Magnetic Resonance (^{1}H-NMR) spectroscopy. In parallel, back-calculation of diffusivity and solubility of oxygen as well as the activation energy via kinetics is performed by utilising a Dynamic Vapour Sorption (DVS) analyser and thin film oxidation kinetics, respectively. In Chapter 4, the same binders are investigated in the lab with RTFOT and PAV. In the same Chapter 4, for two of the aforementioned

binders extensive chemical analysis, performed additionally in its bitumen fractions before and after PAV, is also discussed.

Part III of this book dives into the mechanisms accompanying the changes in bitumen's surface microstructure for two bituminous binders differing in compositional information in terms of natural wax. In Chapter 5, Differential Scanning Calorimetry (DSC) and Wide Angle X-ray Diffraction (WAXD) are combined with optical observations via a CLSM in an effort to link the thermal transition phenomena, the crystallinity of bitumen and the observed microstructural patterns of it, known as the bee structures. In the same part III of the dissertation in Chapter 6, a wider range of the two types of binders are examined for their microstructural properties related to the bee area percentage, waveform characteristics and probabilistic values of the bee structures. Commercial software packages and deep learning techniques are employed for the bee structure identification. Coupling of Confocal Laser Scanning Microscopy (CLSM) and Atomic Force Microscopy (AFM) demonstrates a clear effect of ageing on specific traits of these patterns.

Part IV of this book in Chapters 7 and 8 respectively, directs to the phenomenological and mechanism-based modelling approaches performed. In Chapter 7 the fundamental information obtained for the three binders in part II is first compared with regard to the convergence of different ageing protocols for their chemistry and rheology. Various statistical methods (Bivariate analysis, Wilcoxon exact Rank-sum test, Factor analysis) assisted in identifying relationships among the chemo-rheological parameters. The work is completed in Chapter 8 with the first efforts to model in a Thermodynamics of Irreversible Processes (TIP) model the ageing mechanisms supported in part II for bitumen, accounting simultaneously for its fractions.

Finally, in Chapter 9 (part V), the main conclusions extracted from this dissertation are reviewed and the way to assist in future research are discussed. Recommendations for future work are proposed as well as suggestions to link the current observations with field performance.

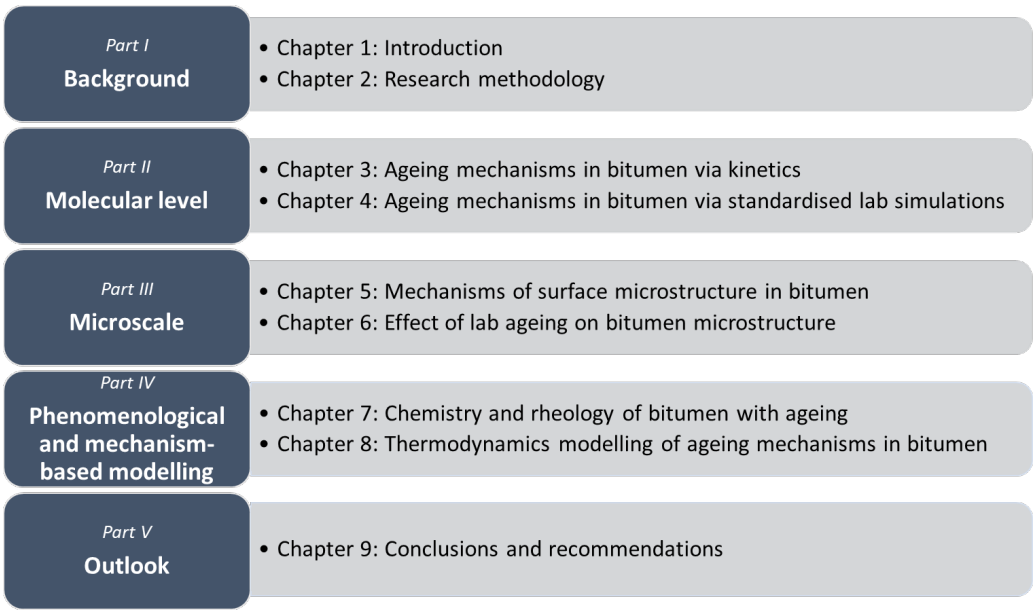

Figure 1-2 Schematic structure of the research

2

RESEARCH METHODOLOGY

2.1 **Summary**[*]

In this Chapter 2, the research methodology adopted during this project is scrutinised with respect to its working principles and capabilities for bitumen. The theoretical background of the techniques and analyses used is briefly explained so that the reader becomes familiar with them. An overview of the usage of the most appropriate techniques in order to evaluate the ageing process in bitumen both from a chemical and rheological perspective, is given in Table 2-1. Finally, the challenges to harmonise the information obtained between the various techniques are acknowledged and discussed.

Table 2-1 Overview of experimental techniques in this dissertation and target goals

Experimental technique	Purpose of use
FTIR	Oxygenated products, oxidation phases and activation energies
EPR	Identification of free radicals and oxidation phases
^{1}H-NMR	Chemical classification of proton regions
TOF-SIMS	Oxygenated products
DVS	Diffusivity and reactivity
DSC	Thermal transitions
WAXD	Crystallinity
AFM	Identification of bee structures and their characteristics
CLSM	Identification of bee structures and their characteristics
DSR	Rheological characterisation

[*]*This chapter is redrafted from: G. Pipintakos et al., Application of Atomic Force (AFM), Environmental Scanning Electron (ESEM) and Confocal Laser Scanning Microscopy (CLSM) in bitumen: A review of the ageing effect, Micron (2021). https://doi.org/10.1016/j.micron.2021.103083*

2.2 Material selection

For a holistic viewpoint of the ageing process, it is necessary to vary the type of the examined binders so that the obtained results can be generalised as much as possible. With this in mind, the binders selected for all the subsequent experimental techniques were varying in four main aspects: 1. their empirical performance, 2. their origin of crude source, 3. their wax presence and 4. their manufacturing process. To better accommodate for the reader the association between the results of the performed experiments and the type of binder, the exact details of the binders are given in the corresponding section of 'Materials and Methods' of each Chapter.

2.3 Spectroscopic techniques

2.3.1 *Fourier Transform Infrared (FTIR) spectroscopy*

2.3.1.1 Working Principles

The general operation of FTIR is based on the absorption and interaction of infrared radiation with the chemical bonds of the material under investigation. An infrared beam is emitted to the specimen and activates certain chemical bonds in its molecules, which start to vibrate at specific frequencies. Thus, the change of the bond or structure at the molecular level is depicted by the infrared absorption during vibration, which is related to a specific frequency for each bond. The vibrations of these bonds are crucial for identifying the type of functional groups in a material, which works as a kind of 'chemical fingerprinting'. These vibrations can be either stretching of the atoms in a molecule or bending by means of a change in angle between two bonds.

The two general modes used for performing FTIR analyses are in transmittance and in reflection. In the first mode, the radiation is sent through the sample and specific wavelengths are absorbed. For the second mode, typically, the addition of an Attenuated Total Reflectance (ATR) fixture allows total reflection, as radiation enters the FTIR crystal and reflects off the internal surface in contact with the sample. The reflection can be a single or multiple ones depending on the utilised crystal. In this mode, in the case of multiple reflections, the infrared beam is reflected by the sample multiple times inside the crystal. It should be noted that the infrared wave is capable to penetrate only a few μm in the sample, and the prism is manufactured in such a way to ensure the total reflectance of the beam. Commonly used crystals of diamond and germanium have refractive indices which are larger than the testing materials to ensure internal reflectance. Finally, the sample absorbs specific frequencies and the

beam loses energy at this particular frequency for each functional group. The radiation after reflection is collected by a detector connected to a software which can demonstrate in a spectrum the wavenumber against absorbance or transmittance.

2.3.1.2 Bitumen application

Undeniably, FTIR is a versatile, easy-going spectroscopic tool not only for chemists and bitumen producers but also for road engineers in order to evaluate, among others, the ageing severity of bitumen and to trace certain additives. For the ageing severity, the functional groups of sulfoxides and carbonyls are more often used as indices whereas other indices are used to track i.e. the aromatisation process in bitumen.

In the current research project, the FTIR analysis was performed in reflection mode with a Thermo Scientific Nicolet iS10 and iS50 FTIR spectrometer equipped with an ATR fixture and a Smart Orbit Sampling Accessory. At least three replicates were measured per sample in different ageing states used in this study. The collected spectra were acquired with 32 repetitive scans and ranged from wavenumbers between 400 cm^{-1} and 4000 cm^{-1} with a resolution of 4 cm^{-1}.

After the spectra acquisition, the protocol as described in [45] for the determination of the normalised intensity of certain functional groups, was followed. More specifically, the areas around certain peaks of an infrared spectrum are calculated. To do this, a baseline is introduced based on the limits of each band given in Table 2-2 and the area that is enclosed is computed based on the trapezoidal rule that approximates a definite integral. For the quantification of the corresponding normalised index, Equation 2-1 to Equation 2-4, are finally applied.

Table 2-2 Band limits of the utilised FTIR functional groups [45,110,111]

Functional group	Bond vibration	Band limits for baseline (cm^{-1})	Area around peak n, (A_n)
Long chain alkanes	$(CH_2)_n$ rock (n ≥ 4) bending	734-710	724
Aromatic structures	C=CH adjacent out of plane bending	783-734	743
Aromatic structures	C=CH adjacent out of plane bending	838-783	814
Aromatic structures	C=CH singlet out of plane bending	912-838	864
Sulfoxides	S=O stretching	1047-995	1030
Branched aliphatic structures	CH_3 symmetric bending	1390-1350	1376
Aliphatic structures	CH_3 asymmetric bending	1525-1395	1460
Aromatic structures	C=C stretching	1670-1535	1600
Carbonyls	C=O stretching	1753-1660	1700

Aliphatic structures	C-H symmetric stretching	2880-2820	2862
Aliphatic structures	C-H asymmetric stretching	2990-2880	2953

$$\text{norm. sulfoxide index (SOI)} = \frac{A_{1030}}{\sum^{n} A_n} \qquad \textit{Equation 2-1}$$

$$\text{norm. carbonyl index (COI)} = \frac{A_{1700}}{\sum^{n} A_n} \qquad \textit{Equation 2-2}$$

$$\text{norm. branched aliphatic index (BAI)} = \frac{A_{1376}}{A_{1460} + A_{1376}} \qquad \textit{Equation 2-3}$$

$$\text{norm. aromaticity index (ARI)} = \frac{A_{1600}}{\sum^{n} A_n} \qquad \textit{Equation 2-4}$$

2.3.2 *Electron Paramagnetic Resonance (EPR) spectroscopy*

2.3.2.1 Working Principles

EPR is a spectroscopic technique able to identify paramagnetic centres and molecules in a material, i.e. the components containing unpaired electrons. It is particularly useful to characterise organic radicals and transition-metal ions. The basic idea of this technique is based on the fact that atoms, ions, molecules or molecular fragments which have an odd number of electrons exhibit characteristic magnetic properties. In parallel, it is known that each electron is a charged particle which spins around its axis causing a magnetic moment (intrinsic property) and orients when placed inside a strong magnetic field of an EPR, where electromagnetic radiation is applied monochromatically. The alignment of the unpaired electrons creates two spin states which have also different energies. Hence, an electron can move between the two energy levels by absorption or emission of a photon of energy when resonance conditions are fulfilled. Although different frequencies and magnetic field values can in principle be used the majority of EPR experiments are performed in the X-band (9-10 GHz) by keeping the photon frequency fixed and varying the external magnetic field incident on the sample under investigation until it matches the energy of the microwaves in the X-band. In this state the unpaired electrons can move freely between the two spin states and the absorption that is recorded is converted into a spectrum.

Concerning the different existing EPR types, these can be mainly categorised in high-field high-frequency, pulsed and Continuous-Wave (CW) measurements depending on the source of radiation and the type of it. Many EPR applications make use of CW EPR as it has the advantage over pulse EPR to detect with high sensitivity at room temperature and is less expensive than pulsed EPR.

2.3.2.2 Bitumen application

CW EPR spectra of bitumen samples were recorded in this research project with a Bruker Elexsys E680 spectrometer mounted with an ER 4102ST TE102 mode resonator working at ~9.75 GHz (X-band). Polypropylene Eppendorf tubes were used as sample holders ensuring that the total bitumen quantity did not overfill the cavity. Preliminary measurements in the studied binders showed a two-component EPR spectrum consisting of contributions of a vanadyl centre (VO^{2+}, S = 1/2) and an organic carbon-centred radical. The former is characterised by an axial powder pattern (Figure 2-1 [left]) with typical hyperfine splitting due to the interaction of the electron with the ^{51}V nucleus (I = 5/2), and the latter gives rise to an unresolved single line close to the free electron value (g_e = 2.0023).

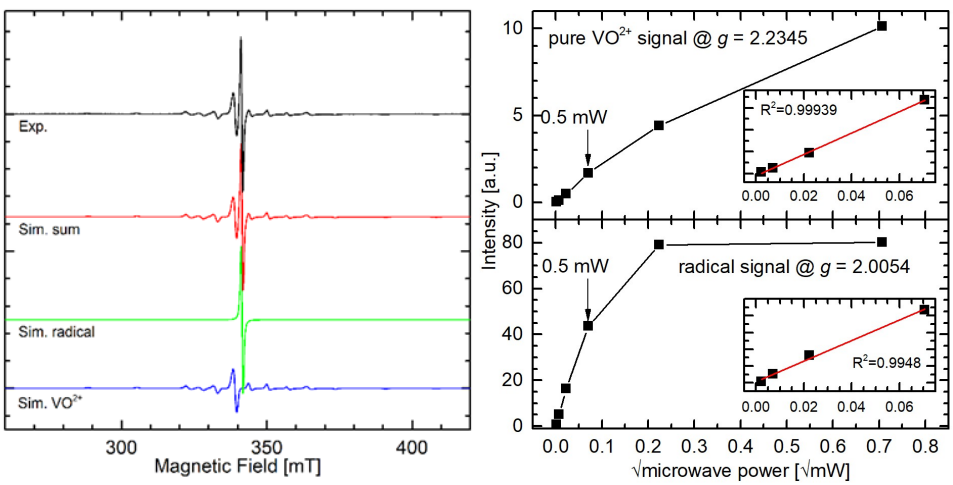

Figure 2-1 Room temperature CW X-band EPR spectra of indicative bitumen sample with its simulations [left] and its signal intensity contrasted with the square root of the power at different g-values, with insets showing a linear fit of selected powers [right]

Power saturation measurements showing different relaxation rates (Figure 2-1 [right]) confirmed the presence of the two species, namely organic carbon-centred radicals and VO^{2+}. For all the subsequent measurements, 0.5 mW was chosen, because this was close to the highest microwave power level before either species became saturated (i.e. signal intensity vs √microwave power was linear). At least three replicates were measured per sample state with the centre field at 341 mT, sweep width of 20 mT,

resolution of 2048 points, modulation amplitude of 0.1 mT and modulation frequency of 100 kHz over 2 scans. Simulation of the experimental spectra with Matlab2018b using the EasySpin-6.0 module [112], gave the EPR parameters of the two species as well as the relative amounts of spins between the two ('weights'). Next, the number of spins in each sample was estimated by comparing the double integral of each spectrum with those of TEMPO (2,2,6,6-tetramethyl-1-piperidinyloxyl, a chemical compound used commonly as a structural probe for radicals' characterisation) in toluene solution standards. More specifically, the number of VO^{2+} or organic radical spins in each sample was estimated by comparing the weights used in the spectral simulations. As last step, division by the mass of the sample gave the number of spins per gram of sample.

2.3.3 *Time-of-flight Secondary Ion Mass Spectrometry (TOF-SIMS)*

2.3.3.1 Working Principles

The analysis principle of typical TOF-SIMS includes the bombardment of the outermost surface layers of a sample with high-energy primary ions and analysis of the emitted (secondary) ions with respect to mass-to-charge ratio (m/z). In general, the emitted particles by the collision process of the primary ions vary considerably and can include atoms, molecular fragments, intact molecules and molecular complexes which when energetically charged can be analysed by a TOF analyser providing eventually a mass spectrum.

The obtained mass spectra provide molecular information about the sample surface whereas imaging of specific ions is accomplished by scanning the primary ion beam over a selected analysis area and acquiring separate mass spectra in each pixel [113]. In principle, the selection of the number of pixels in the TOF-SIMS analyses, i.e. the number of data points within the analysis area, is based on the fact that the pixel size should be matched with the diameter of the primary ion beam. The acquired data can be displayed in a variety of ways, i.e. total area mass spectra and ion images that show the spatial signal intensity distribution of selected secondary ions on the sample surface by means of chemical mapping. Another option is to display mass spectra from selected regions of interest, providing detailed chemical information about specific structures within the analysis area.

2.3.3.2 Bitumen application

In this research project, the TOF-SIMS analyses were conducted in a TOF-SIMS IV instrument (IONTOF GmbH, Germany) using 25 keV Bi_3^+ primary ions and low-energy electron flooding for charge compensation. During analysis, the sample temperature

was kept between -50 °C and -80 °C to prevent diffusion/segregation of the sample in the vacuum environment of the TOF-SIMS instrument. For the sample preparation, bituminous samples of 1 mm thickness were deposited on silicon wafer substrates 10 mm x 10 mm and subsequently allowed to cool down according to the protocol reported in [4]. The surface information obtained by Bi_3^+ primary ions penetration has been estimated to be just a few nanometres [113].

Positive and negative ion spectra were acquired over analysis areas of 200 µm x 200 µm (128 x 128 pixels) or 500 µm x 500 µm (256 x 256 pixels) at three locations of each sample, with the instrument optimised for high mass resolution (m/Δm ≈ 3000-6000). The spectra for all the samples were analysed based on the intensity of the areas of selective mass-to-charge-ratios, assigned to specific ions, normalised by the total recorded ions' intensity (counts). To obtain more in-depth insights into the chemical mapping in selected specimens additional positive and negative ion data were acquired (i.e. high-resolution images) with the instrument optimised for high image resolution (lateral resolution ≈ 0.5 µm). In all the cases, the instrument was controlled and the data was acquired by the IONVAC software (IonTOF), while they were processed using Surfacelab 7 (IonTOF).

2.3.4 *Proton Nuclear Magnetic Resonance (^{1}H-NMR) spectroscopy*

2.3.4.1 *Working Principles*

NMR spectroscopy was initially developed to study the properties of the atomic nuclei whereas later was realised that can be used to study the structures of organic compounds. The principle is based on the fact that nuclei, such as hydrogen, which have an odd number of protons and/or an odd number of neutrons possess a property, called spin, which allows them to be studied by NMR quite similar to the principles of EPR. In other words, a nucleus with a spin has a magnetic moment and generates a magnetic field which when placed between the poles of a strong applied magnetic field makes the nuclei align with or against this applied field, while the difference between the two spin states depends on the strength of the applied magnetic field and successively on the frequency of the spectrometer. Flipping the spin states of nuclei requires an amount of energy to be absorbed which is the radiation in the radio frequency region of the electromagnetic spectrum. This radiation absorption generates signals whose frequency depends on the difference between the spin states. Hence, the chemical shift of a particular nucleus results from the modification of the local magnetic field at the location of the nucleus by the shielding of the external magnetic field by the electrons around the nucleus, which is dependent on the binding

state of the atom in question. Finally, an NMR spectrometer is able to detect these signals and depict them in a graph of frequency versus intensity, known as the NMR spectrum. In modern pulsed NMR, the magnetic field is held constant while the radio frequency pulse covers a range of frequencies so that all the nuclei can come eventually into resonance. Most frequently, the NMR spectra are recorded in solutions with deuterated solvents. It is the deuterium signal that is later used to monitor the difference with the onset of the chemical shifts. It is finally worth mentioning that the origin of the terminology of nuclear magnetic resonance derives from the fact that the nuclei are in resonance (flipping their spin state) with a corresponding radio frequency radiation.

2.3.4.2 *Bitumen application*

^{1}H-NMR is a superior spectroscopic technique able to characterise the molecular structure of a material, even for a complex one, such as bitumen. It can assist with the characterisation of the relative amount of different types of aliphatic, olefinic and aromatic protons in bitumen [114–116] and therefore can also be applied to capture the proton distribution upon ageing in bitumen. In this research work, data collection of all the bituminous binders at room temperature was conducted with a high-resolution liquid-state Bruker Avance III HD 400 MHz smart probe spectrometer (32 scans). Preliminary measurements with $CDCl_3$ (deuterated chloroform) as solvent showed interference with the aromatic region signal of bitumen, while different concentrations of dissolution with 5 and 40 mg of bitumen showed a poor and an overloaded ^{1}H-NMR signal respectively. Therefore, ± 20 mg of bitumen or its fractions were dissolved in 650 µl of deuterated tetrachloroethane ($C_2D_2Cl_4$) inside borosilicate NMR tubes (ASTM Type 1 Class B glass) of diameter 5 mm and a wall thickness of 0.4 mm. To ensure an adequate dissolution of the solvent with the specimen all vials containing the dissolved samples were additionally placed inside an ultrasonic water bath for 10 minutes before the ^{1}H-NMR analysis. The repeatability was provided by means of standard deviations.

After the analysis, steps were first taken to accurately calibrate the starting chemical shift based on the difference of the residual solvent peak (6.00 ppm) with respect to TMS (tetramethylsilane) (0.00 ppm) [117]. The analysis of the results was performed in the MestreNova spectral analysing software following the integration of the typical proton chemical shift regions reported in [118], neglecting each time the protons associated to heteroatoms and the residual solvent at 6.00 ppm. The latter study classifies a typical ^{1}H-NMR spectrum of bitumen in five main groups, given in Table 2-3. Normalisation of all the integrated areas with the exact sample mass allows for a fair

comparison of the relative percentage distribution of the different types of protons identified in bituminous samples.

Table 2-3 Typical groups of protons in bitumen

Designation	Chemical shift range	Type of protons	Major proton peak in this region
H_{methyl}	0.5-1.0	Aliphatic hydrogen on C_γ and the CH_3 beyond the C_γ to aromatic rings	Methyl
$H_{methylene}$	1.0-2.0	Aliphatic hydrogen on C_β and the CH_2 beyond the C_β to aromatic rings	Methylene
$H_{\alpha\text{-}alkyl}$	2.0-4.0	Aliphatic hydrogen on C_α to aromatic rings	-
$H_{olefinic}$	4.0-6.0	Olefinic hydrogen	-
$H_{aromatic}$	6.0-9.0	Aromatic hydrogen	-

2.4 **Gravimetric techniques**

2.4.1 ***Dynamic Vapour Sorption (DVS)***

2.4.1.1 *Working Principles*

DVS is an automated gravimetric analyser able to determine with high precision mass balance changes of resolution of ±0.1 mg due to a gas flow in the sample under investigation. Modern DVS devices allow the calibration of the humidity level, partial pressure, the mix of different gasses and the temperature control under which a specified program is executed in a predefined time. It is a particularly useful device to examine vapour sorption/desorption, adsorption and absorption phenomena of a material.

2.4.1.2 *Bitumen application*

In this work access to DVS, Surface Measurement Systems was provided by the Pavement Engineering research group of Delft University of Technology. The DVS was utilised to study the uptake of oxygen vapour into bituminous mastics. To that end, the relative humidity was kept to a minimum in the samples prior to testing by placing them inside a vacuum environment with silica gel for one week before the experiment. The humidity was recorded during this drying stage to ensure that there was no effect of induced humidity in the subsequent gravimetrical changes. This was only possible with bituminous mastics and not with bitumen. The samples and the reference pan of the DVS were successively exposed to dry air (20% O_2 + 80% N_2) for a total period of 7 days under isothermal conditions at 75 °C. Preliminary studies with the added filler of the mastics under the exact same conditions showed no change of mass due to dry air, whereas an increase of the initial mass of mastics was observed for the bituminous

mastics. In the current research project, this was attributed completely to oxygen reaction-diffusion in bitumen.

2.5 **Thermoanalytical techniques**

2.5.1 ***Differential Scanning Calorimetry (DSC)***

2.5.1.1 *Working Principles*

Nowadays the three most common types of DSC are heat-flux, power compensation and fast-scan. Whatever the type is, the working principles are somewhat similar for the material characterisation and vary with respect to the sensor and supplied power to the specimen. In general, with this thermodynamical tool, a specified temperature program is applied by means of heat flow both to the investigated sample and a known reference material and the amount of heat difference to match the exact same temperature between the two is measured as a function of temperature. DSC enables the investigation of endothermic or exothermic phase transition phenomena (melt, crystallisation, demixing, remixing and others), second order phenomena (glass transitions) and chemical reactions (thermal curing, specific heat capacity and others). At the end of the temperature program, the recorded data of a DSC result in a curve of heat flux versus temperature known as thermogram which can be also used to calculate the enthalpy of a specific transition.

2.5.1.2 *Bitumen application*

A TA Instrument, model 2920 DSC was used in this research project. For each analysis, samples of approximately 15 mg were hermetically sealed into a sample pan, then heated to 110 °C and kept at this temperature for 15 minutes. The data were first recorded during cooling to -110 °C and heating to 110 °C, both at a rate of 10 °C/min. To examine the effects of annealing for DSC, thermograms were also acquired for selected samples in the same cooling and heating cycles, after 24 hours at 25 °C and the data of the heating ramp were recorded. The measured thermal characteristics of bitumen before and after the annealing period of 24 hours include onset, end and peak temperatures as well as enthalpies for the wax crystallisation and melting. For the quantification of the enthalpies, integration of the area enclosed between the experimental DSC curve and a linear extrapolation from the melt data was performed. Additionally, the glass transition temperatures were reported from the same thermograms.

2.5.2 *Wide Angle X-ray Diffraction (WAXD)*

2.5.2.1 Working Principles

This technique is commonly used to obtain information for crystalline materials by making use of the fact that these ordered patterns cause a beam of incident X-rays to diffract in specific directions. The analysis of the scattered angles and intensities of the diffracted rays by a detector can be used to obtain information about the cause of them which is commonly ascribed to nanosized structures. The principle of the technique is based on the scanning of the sample with a wide-angle goniometer where the scattering intensity is typically plotted as a function of the 2θ angle. With WAXD the degree of crystallinity can be estimated at a specific temperature or in a range of temperatures during cooling/heating scans. Additionally, the patterns of the internal structure of the crystal can be determined.

2.5.2.2 Bitumen application

To collect the WAXD patterns, a X33 double-focusing camera of the EMBL in HASYLAB was used on the storage ring DORIS of the Deutsches Elektronen Synchrotron (DESY), Hamburg, Germany, at a wavelength of 1.5 Å [119]. The bituminous samples in their liquid state at high temperature were inserted in small sample holders and sealed with aluminium foil [120]. After cooling to room temperature, the samples were stored for 3 days at room temperature prior to collecting a WAXD pattern at 25 °C. In addition, WAXD patterns were collected during a cooling/heating scan at 10 °C/min from 100 °C down to -40 °C and again up to 250 °C after 2 min at -40 °C. For this time resolved measurement, patterns were collected in consecutive frames of 6s, which corresponded to a temperature resolution of one pattern per °C. The temperature was controlled by a Mettler FP-82HT hot stage, flushed with cooled nitrogen to achieve the required cooling rate. After a background correction, the WAXD patterns were normalised to their integral to ensure a constant scattering mass. A crystallinity index was extracted from the normalised patterns by integrating the intensity of the 110 and 200 orthorhombic reflections, separated from the liquid scattering using linear sectors.

For the calibration of the scattering angles, the 110 and 200 reflections of a quenched linear polyethylene were used. The obtained data were treated as a function of the scattering angle but converted to the scattering angle expected in the case $Cu_{K\alpha}$ radiation would have been used (λ = 1.542 Å) instead of λ = 1.5 Å. Such a representation facilitates comparison with literature data, which most often make use of $Cu_{K\alpha}$ radiation.

2.6 **Microscopic techniques**

2.6.1 ***Atomic Force Microscopy (AFM)***

2.6.1.1 *Working Principles*

Imaging with the AFM microscope has evolved over the past years but the general working principles remain the same, rooted back in its invention in 1986 [121]. More specifically, the imaging of the target uses a cantilever, with a sharp tip that is used to scan the sample surface by interacting with it. When the cantilever experiences a force between the tip and the sample, measured by a laser beam that is placed at the end of the cantilever, it deflects and shifts up according to the Hooke's law. This results in a deviation of the laser beam from its original position, which is measured as a voltage. This voltage is translated into a variety of forces (e.g. mechanical contact force, capillary forces etc.) or relative height and an image can be made based on all the measured differences [121,122].

There are different operational modes of an AFM, but among others (near-contact, pulsed force, lateral force mode) the most common ones are the dynamic (tapping) and the static (contact) mode [21]. With contact mode, one refers to the mode where the tip stays in contact with the sample at constant load, while the surface is moving in the plane directions. This mode is able to generate both frictional and topographic data. Tapping mode, on the other hand, occurs when the cantilever, oscillating up and down at its resonance frequency, is gently tapped on the surface to reach contact and then shifts in the plane directions when the tip is lifted away from contact. This mode provides phase and topographic data and generally reduces the risk of destroying the surface compared to the static mode where the developing forces are higher [122].

2.6.1.2 *Bitumen application*

The surface microstructure of bitumen is still a subject that is not fully understood and completed. Over the years, there were a lot of attempts to examine the microstructure of bitumen, with the most commonly used technique being the optical microscope. AFM proved to be a promising alternative and was adopted by bitumen researchers soon after its invention [70]. The results give information about the topography and phase contrast of the sample and are therefore especially useful for multi-phase materials such as bitumen. Using AFM, experts aimed to characterise the topography, stiffness, tackiness and molecular interaction at the micro-level of materials [123]. In parallel, mechanical properties of bitumen such as adhesion, rigidity, hardness and modulus of elasticity can be estimated by employing AFM with the nanoindentation

technique [124]. This technique penetrates the bitumen surface with a tip of defined geometry [125].

The fact that AFM is time-efficient and has a relatively simple sample preparation, makes its use favourable. Attention should be though given to the consistency of the preparation procedures as it may introduce differences if the handling procedure and storage conditions vary significantly between the samples. In general, sample preparation can be done by two different techniques for bituminous binders, either the spin or the heat casting method.

Spin casting includes a spinning plate, in which the sample is cast on. The centrifugal forces of the plate provoke the sample to spread evenly so that it eventually results in a thin film for the imaging. Beforehand, the bitumen is dissolved in a solvent which evaporates after the spinning. Allen and his coworkers suggested the elimination of the residual solvent to preserve the sample in an airtight heated vacuum desiccator followed by a purification step with dry nitrogen [126]. For the heat casting method, the bitumen is heated and stirred at a temperature of 110-130 °C, according to the bitumen type to be workable, and profoundly mixed so that a specimen has no more oxidants or dust compared to a replica of the same bitumen tank [74]. Next, a bitumen drop of 15-30 mg is placed on a conductive sample holder and held horizontally on a heating plate (set at the same temperature as the heating temperature of bitumen) so it would spread evenly and become a flat surface. The samples are normally tested directly in the AFM and then held in a dust-free environment before testing again at different time intervals so that the microstructures can settle and their evolution can appear on the bitumen's surface.

In the current research project, AFM imaging was recorded using an Asylum Research MFP-ED AFM in tapping mode. A resonance frequency 300 kHz and spring constant 26 Nm^{-1} of an AC 160 TS cantilever tip were utilised for this study. With regard to the instrumental settings, the vertical Z-axis displacement of the measuring head is constrained to 15 μm, while the sensor noise is less than 25 nm with an average deviation in a 0.1-1 kHz bandwidth for this device. In order to scan the bitumen surface, X and Y activators are used with a travel distance limited to 90 μm, with sensor noise in these directions less than 0.5 nm as an average deviation in a 0.1-10 kHz bandwidth. All the binders were recorded in a scan size between 20x20 to 40x40 μm so that for each sample the number of observed microstructures has a statistically meaningful calculation.

To minimise the effects of thermal history and other effects like the nature of the sample substrate [73,127], the preparation method in [69] was adopted. In this procedure, a small quantity of bitumen is heated to 160 °C for 15 minutes and after

proper stirring with a metal spoon, a hot droplet is placed on a 76x26 mm pre-cleaned glass slide (Thermo Scientific) with ground edges and a frosted end. To achieve a flat surface the glass slide with the droplet is reheated on a hot stage for one minute. The samples are then let to cool down and stored in a dark and dust-free place before the measurements. All the scans are performed in air at 25 °C after a storage time of 24 hours, to allow the microstructures to develop and stabilise [73]. The analysis and processing of the AFM images were performed using the open-source, image editing software package Gwyddion (version 2.58) [128].

2.6.2 *Confocal Laser Scanning Microscopy (CLSM)*

2.6.2.1 Working Principles

The CLSM has become a popular method in biology, biomedical, and material sciences in the past few decades [129,130]. The basic concept of confocal microscopy was first developed and patented by Marvin Minsky in 1957 to image the neural networks in unstrained preparations of brain tissues [131]. Unlike conventional optical microscopes, confocal microscopes apply a spatial pinhole in front of the detector to focus the laser beam on just one predefined depth. It was during the 1970s and 1980s that the advances in computer and laser technology led to the development of the CLSM [132]. In CSLM, the light source, which is a laser beam, based on depth selectivity allows for optical sectioning. The information gained from this focal point is projected on a pinhole in front of the detector, which ensures that only the light from the small area of the sample, which is irradiated, is detected [133]. Apart from the reflectance or transmission mode, CLSM can also operate in fluorescence mode. This is done by using a different laser light source with a lower wavelength. In fluorescence mode, the molecules absorb the high energy (short wavelength) light and after a short lag period (fluorescence lifetime) emit a lower energy (longer wavelength) light.

Comparison of images taken by conventional optical microscopy and CLSM in reflected light mode has indicated the higher resolution and thus the better quality of the images obtained with CLSM [134]. Finally, in a CLSM, the image is created by scanning the surface point by point. If this is done in the x-y plane for different depths in the z-direction, the 2D images can be reconstructed rather fast into a 3D representation and without direct contact with the surface, which is the biggest advantage of CLSM over other microscopic techniques [134]. By successive scanning, at different focal points, a topographic image is finally obtained [132].

2.6.2.2 Bitumen application

CLSM is a relatively new technique to investigate the microstructure of bitumen. This technique has been used both in reflectance and fluorescence mode on bitumen. Next to its capability of creating 3D reconstructions, using CLSM to investigate bitumen requires little pre-treatment.

CLSM in reflectance mode has been used by researchers to determine the size, distribution, and shape of the asphaltene particles [134] or the classification of wax morphology [81]. Furthermore, in the last few years, researchers started to use this technique to observe fluorescence centres in bitumen. It was demonstrated that bitumen exhibits fluorescence when irradiated with 488 nm wavelength light [135]. Therefore, to investigate bitumen using CLSM in fluorescence mode, the samples are typically irradiated with 488 nm wavelength laser light, while observation of emitted signals is mostly done in the 500-550 nm wavelength range [136–138].

Other than using CLSM to investigate virgin bitumen, this technique was also used to study the morphology of polymer-modified bitumen [139–141] and recycled asphalt shingle blended with asphalt binder [137]. Moreover, CLSM has been widely used to explore the morphology of epoxy asphalt binder [142], phase-separated microstructure and dispersion of the asphalt rubber in epoxy asphalt [143,144], as well as the morphology and phase separation of polymer-modified epoxy asphalt binders [145–147].

In the current study, a Keyence VK-X1000 CLSM was used, mounted with a VK-D1 motorised XY-stage. Recording of topographical images was conducted with a laser and white light source. Among a variety of available lenses, the Nikon Lens Plan Apo EPI with a magnification of 150 times, 5 nm lateral resolution and 10 nm axial resolution was utilised. The lens magnification was chosen so that the obtained images were of a similar scan size and contain a statistically meaningful number of bee structures. All the images were captured in ambient conditions using the same sample preparation and storage time as for the AFM measurements. The images were further processed with the commercially available software package VK MultiFileAnalyzer (version 2.2.0.93). During image processing, a surface shape correction was applied as well as a smoothing of the surface to eliminate any noise.

2.7 Rheological characterisation

2.7.1 *Dynamic Shear Rheometer (DSR)*

2.7.1.1 Working Principles

This type of testing is based on the oscillation of the upper of two parallel plates in a DSR where a sandwiched sample is placed in between, while the base plate remains clamped. The sample is subjected to sinusoidal torque or sinusoidal angular displacement of constant frequency or strain under a specified temperature, frequency/strain program. As such, rheological properties can be extracted as the result of the applied torque and displacement, converted into shear stress or strain respectively. The ratio of these amplitudes is then used to calculate the norm of the complex modulus (G*) and the phase angle (δ) of the investigated material in a range of temperatures and frequencies (under a strain-controlled test). Apart from the norm of the complex modulus, other basic dynamic parameters of paramount importance are the storage or elastic modulus G' (in-phase component of G*) and the loss modulus G'' (out-of-phase component of G*). From a practical point of view, the appropriate selection of the controlled stress or strain is crucial to fulfil the linearity requirements of the viscoelastic range within which the majority of rheological tests are performed.

Thus, DSR gives an indication of the resistance of the material to deformation due to stress, understood by the complex modulus. In parallel, one of the primary functions of a DSR is to address the nature of the material varying from viscous to elastic depending on the temperature and frequency. For example, in low phase angle values, the material behaves as an elastic solid, whereas a high phase angle indicates a behaviour of a viscous fluid. These parameters are often not the last step but rather an intermediate one by making further use of the time-temperature superposition principle (TTSP), when applicable. More specifically, the data extracted from isothermal plots can be shifted, based on the TTSP, and further used to model the complex modulus and the phase angle in a wider range of frequencies/temperatures with a continuous curve, known as a master curve.

2.7.1.2 Frequency sweeps

Two DSR devices, an Anton Paar MCR 101 and an MCR 500 were used for the rheological assessment of the bituminous binders. The former was used for the low-temperature range, -30 °C to +10 °C, with a plate-plate geometry of 4 mm diameter, whereas the latter was used for higher temperatures ranging between 0 °C to +40 °C and +30 °C to +70 °C with 8 and 25 mm diameter of plates respectively. Strain levels of 0.02 %, 0.05 % and 1 % with increasing diameter were found adequate to perform strain-controlled frequency sweeps within the linear viscoelastic region (LVER). Therefore, frequency sweeps from 0.1 to 10 Hz were conducted according to EN14770 in sandwiched samples of 1.75, 2.00 and 1.00 mm thickness by increasing diameter.

Processing of the DSR raw data was performed with the rheological software RHEA (version 2.0.2) in order to construct master curves based on the Christensen-Andersen model [148]. Various advanced rheological parameters related i.e. to non-load related cracking of bitumen can be extracted by this master curve. Recent studies have shown the evolution of these meaningful rheological parameters with ageing as well as the relationships between them [93,149–151]. Hence, a selection among these rheological indicators is considered of paramount importance to evaluate the performance of bitumen. An overview of the rheological parameters used in this work alongside their definition and the effect of ageing on them is provided in Table 2-4.

Table 2-4 Advanced rheological parameters

Rheological value	**Formula**	**Definition**	**Plate geometry**	**Evolution with ageing**	**Indication**
Crossover modulus (G_c)	Respective values derived by a master curve where a phase angle is δ=45°	The modulus, frequency and temperature at the point where the loss modulus G´´ coincides with the storage modulus G´	8 and 25 mm	↓	Elastic/viscous transition, brittleness, hardness [95,152]
Crossover frequency (ω_c)					
Crossover temperature (T_c)				↑	Rutting and cracking [153]
Shape parameter (R)	$R = \log G_g - \log G_c$ where G_g is the glassy modulus and G_c is the crossover modulus	Difference between the moduli of glassy behaviour and crossover point	4, 8 and 25 mm	↑	Width of relaxation spectrum, fatigue cracking [95,148]
Glover-Rowe (G-R)	$G - R = \frac{G^* \cdot (\cos\delta)^2}{\sin\delta}$ where G^* and δ the complex shear modulus and phase angle at 15 °C, 0.005 rad/s	A parameter based on the complex modulus and phase angle under a specific frequency in correspondence with ductility at the same temperature	8 mm	↑	Durability, non-load related cracking [94,154]

		and specific elongation rate			
ΔT_c	$\Delta T_c = T_{c,G} - T_{c,m}$ where $T_{c,G}$ and $T_{c,m}$ the temperatures where the DSR values of G(60) = 143 MPa and m(60) = 0.275 respectively [155]	Difference of two lower continuous grading temperatures related to creep stiffness and relaxation	4 and 8 mm	↓*	Ageing-induced cracking [154]

*As real number

2.7.1.3 Cup and bob test

An MCR 102 from Anton Paar was selected to be used from the available DSR devices due to the relatively high torque (200 mNm) of this device compared to the previously mentioned DSRs. The fixture of cup and bob was used for the viscosity measurements in a range of shear rates 1-100 s^{-1} according to EN13302. All the bituminous binders of this research project behave as Newtonian fluids in all the ageing states and in the whole range of tested temperatures 110-180 °C. The determination of viscosity is an important factor in the asphalt process as it has a direct effect on mixing with the rest asphalt components and eventually on the mixture's workability and a satisfactory asphalt compaction. Especially the threshold viscosity value of 3 Pa·s at 135 °C has been used to ensure the pumpability of the examined bitumen as well as a guideline to determine mixing and compaction temperatures in the field [156]. The dynamic viscosity value at 135 °C ($\eta_{135°C}$), which has been reported to increase with ageing, was used further in this work.

2.8 **Experimental challenges**

Although the techniques used in this research project are robust enough, limitations may still exist, especially when investigating a multi-component mixture like bitumen. This needs to be acknowledged when reviewing and comparing the findings of each of the techniques as the results may be contradictory.

First of all, FTIR and TOF-SIMS are in fact both surface analysis methods with different penetration depths, of a maximum of 2-3 micrometres for FTIR-ATR [157], and only a few nanometres for TOF-SIMS [113]. In TOF-SIMS an air-cooled surface is investigated,

while in FTIR, the interface as formed against the ATR diamond crystal is investigated. In literature, it has been demonstrated that bitumen may exhibit a different composition depending on the substrate and the environment [4,68,76,158]. Especially, the reproducibility of TOF-SIMS results is an issue that needs special care as the thin film flatness may affect the obtained spectra. In the current study the preparation procedure, the thermal history of the binders and the control of film thickness were kept constant.

Secondly, sample preparation and sample thermal history are different for both the FTIR and TOF-SIMS tests: in FTIR a small hot drop or thin film is placed directly onto the crystal and tested. In TOF-SIMS, hot bitumen drops are first placed on a substrate, which is then shortly reheated and air-cooled, to achieve a flat surface. The analysis temperature is much lower in TOF-SIMS compared to the other spectroscopic techniques, which could for example influence the extent of crystallisation of potential waxy components. For the ^{1}H-NMR tests, the bitumen is dissolved in deuterated tetrachloroethane, and although several steps were taken to obtain dissolved samples (*i.e.* a solvent with appropriate solubility, ultrasonic bath and visual inspection), there is still a risk of some undissolved species. Preliminary trials to dissolve asphaltenes failed although the temperature and dissolution time were considerably increased to obtain a homogeneous solution. Asphaltene particles were still visible and as such no ^{1}H-NMR measurements were carried out on pure asphaltenes due to a risk of high variability between replicates or misinterpretation of the obtained spectra.

Moreover, the detection sensitivity for various chemical compounds is dependent on the respective technique, i.e. FTIR is very sensitive to capture basic oxygenated products (carbonyls and sulfoxides) while it is rather insensitive to changes such as a further aromatisation process [159]. Additionally, in TOF-SIMS only the charged species formed (and not the neutral ones) after a chemical bombardment on the surface are detected. The ^{1}H-NMR by definition will only capture hydrogenated compounds, as such the formation of PAH due to the aromatisation process is not expected to be captured since they do not contain a hydrogen in the middle. In addition, CW EPR shows both bulk and surface paramagnetic centres and its spectral intensity will depend on the time after generation of the radicals and, therefore, centres that are too short living will not be detected in the EPR experiment.

Another point of consideration is the standard ageing protocols performed when investigating bitumen oxidation, which are not conducted in a closed system. Therefore, there is a possibility that volatiles, present or formed during ageing may leave the sample. This effect would be the same for all the analyses performed on the sample after the ageing tests. Bituminous samples could also not be studied in DVS as

the change of recorded mass was within the drift of the microbalance and the samples were not porous enough to obtain more drastic changes.

When it comes to the thermoanalytical techniques, in DSC the acquired signals are typically very broad, they can be combined with exothermic transitions upon reheating and the thermal history of the samples before testing may significantly affect the DSC signals. It is also important to highlight the differences that exist between the thermoanalytical and microscopic techniques which can be related to the specifications and working principles of each technique; the DSC and WAXD tests are related to bulk properties, while the bee structures via AFM or CLSM are a surface phenomenon.

With regard to the surface investigation of bitumen, there is a wide range of microscopic techniques available to evaluate the microstructure which vary in terms of working medium and resolution. A comparison of AFM and CLSM in Table 2-5 reveals that the tapping mode in which the AFM operates allows to record more detailed height patterns and thus depict phase changes as a result of the shift of tip oscillation. This residual effect of tip oscillation may affect slightly the reported topography, although it is considered a near-contact method. In contrast to AFM, the multi-focus imaging capability of the CLSM makes the recording of non-contact images of non-smooth surfaces with large height differences possible. The difference in the resolution of the two microscopies can explain also to some extent differences in the exact length of certain microstructures of the same sample.

Table 2-5 Comparison between AFM and CLSM

Microscope	Radiation source	Working medium	Specimen mounting	Best resolution	Cost of equipment
AFM	Microcantilever probe	air	Aluminium stubs or glass slides	0.5 nm	++
CLSM	Laser light	air	Glass slide	1 nm	++

Currently, AFM is the most common instrument used to investigate the microstructure in bituminous binders. AFM requires minimum sample preparation and can operate in ambient conditions. Other than the microstructure, AFM is also able to provide information on the mechanical properties of the sample on the nanoscale. However, this method is highly sensitive to vibrations during the measurements and can only conduct measurements on a limited scanning area. Other limitations of AFM bitumen application are the fact that the surface of the prepared sample should be relatively smooth and of sufficient thickness to exclude surface-driven effects [160,161].

Moreover, tacky and liquid samples cannot be measured with an AFM in the tapping mode.

It has also been proven that the handling temperature has a significant impact on the final obtained images, and as such for a fair comparison between microscopic findings by different research groups, the thermal history, among other factors, during the sample preparation must remain the same. It is known that the microstructural properties of bitumen are strongly dependent on the isothermal annealing, and cooling rate. This becomes alarming since bitumen can age or undergo steric hardening during or after the sample preparation stage or bitumen samples might collect dust particles before the images are acquired.

For the rheological characterisation of bitumen not only the volatilisation during the ageing simulations but also the type of bitumen, temperature equilibrium time and plate geometry compliance may challenge the validity of the TTSP and thus certain extracted rheological parameters should be handled with extra caution.

Finally, to additionally provide the potential reader with an idea of the repeatability of the conducted measurements, since average values are used in the following, the coefficient of variation was ranging between 0-30% for the spectroscopic, thermoanalytical and microscopic techniques whereas the obtained rheological parameters were within 0-10 %.

3

AGEING MECHANISMS IN BITUMEN VIA KINETICS

3.1 **Summary**[*]

Chapter 3 aims to offer insights into the validity of commonly held hypotheses regarding the oxidation phases of ageing in bitumen, the fast- and the slow-rate phase, and explore the main oxidation products formed upon ageing. In order to evaluate possible differences between bitumen types, the penetration grade as well as the bitumen production process was varied. Thus, the ageing of three different binders was first studied by FTIR and EPR spectroscopy in oxidation kinetics. The formation of oxygen-containing molecular structures on the bitumen surface during ageing was studied with TOF-SIMS. The results of FTIR reveal a gradual increase of sulfoxides upon ageing, while the EPR results show an increase of organic carbon-centred radicals. In parallel, TOF-SIMS results provide evidence for an increase of oxygenated compounds, such as SO_x-, HO_x- and NO_x-containing compounds. It appears also that paramagnetic metal species, such as vanadyl-porphyrins, are insusceptible during ageing. The cumulative FTIR index of carbonyls and sulfoxides showed also a different gradual increase with varying conditioning temperatures and allowed to estimate the reaction rates and activation energies for two of the studied binders. DVS tests were also efficiently utilised for bitumen-filler (mastics) systems and were coupled with FE simulations to allow for a rather accurate prediction of the diffusivity parameters. Overall, the findings of this Chapter are in agreement with a mechanism comprising two rate-determining phases and support the formation of different oxygenated products. It is believed that the experimental approach used in this Chapter may contribute further to an improved understanding of the ageing mechanisms in bitumen.

[*]*This chapter is redrafted from: G. Pipintakos et al., Experimental investigation of the oxidative ageing mechanisms in bitumen, Construction and Building Materials (2020). https://doi.org/10.1016/j.conbuildmat.2020.119702*

3.2 Objectives

Chapter 3 addresses a number of questions regarding the ageing mechanisms of bitumen via oxidation kinetics. An important issue is the validation of the previously proposed oxidation schemes [6]. This was achieved by utilising a number of spectroscopic and gravimetric techniques. In particular, support was provided by FTIR, EPR and TOF-SIMS spectroscopy as well as DVS. Links between the results of the spectroscopic techniques under predefined oxidation time and temperature review certain hypotheses for the ageing mechanisms of bitumen. Additionally, this Chapter attempts to address the effect of increased temperature during short-term ageing on subsequent isothermal reaction kinetics in bitumen as well as to discuss the differences in reactivity and diffusivity of bitumen by means of their activation energy and diffusion coefficients/solubility respectively. A graphical summary including the main objectives for each technique is presented in Figure 3-1.

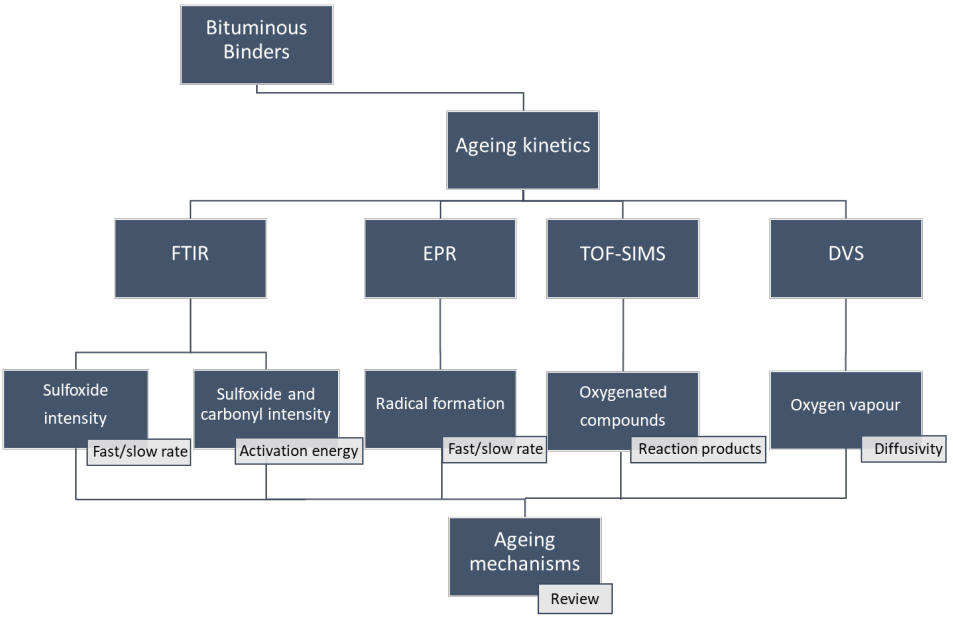

Figure 3-1 Flowchart of the experimental part of Chapter 3 and objectives

3.3 Materials and Methods

Three bituminous binders were used as specified in Table 3-1, namely, a hard binder A and two soft binders B and C. Binders A and B originate from an acidic, wax-free crude oil, and differ only in the degree of distillation processing. Binder C is a visbroken

residue, containing natural wax (crystallisable compounds) and coming from a different crude oil. The bituminous binders were selected so as to vary as much as possible with regard to their empirical properties in order to observe possible differences arising from the bitumen type.

Table 3-1 Basic properties of the bituminous binders

Material	Property	Binder			Test Method
Bitumen		A	B	C	
	Penetration 25 °C (0.1 mm)	16	189	190	EN1426
	Softening point (°C)	61.1	37.5	39.2	EN1427
	Penetration index, Ip	-1.06	-1.46	-0.63	EN12591
	Viscosity 135 °C (mm^2/s)	1285	203	N/D*	EN12595
	Performance Grade (PG)	76-16	52-28	52-22	AASHTO MP1

*N/D=Not Determined

For the mastic sample preparation for DVS, binders A and B were blended at 130 °C with a filler-to-bitumen ratio (mg/mg) of 1, so that the contribution of both can be equally balanced. A commercially available inert filler (Quartz) consisting of 100 % quartz after mineralogical analysis [162], was used to eliminate possible chemical reactions between oxygen and filler and simultaneously to accelerate the diffusion part due to the increased accessibility of oxygen into the more porous mastics compared to virgin bitumen.

To simulate the oxidative ageing of the binders, a Modified Thin Film Oven test (M-TFOT) was used: a binder film of approximately 1 mm thick was aged in a ventilated oven. For the investigation of oxidation kinetics, three different temperatures were employed i.e. 25, 50 and 75 °C for different time intervals based on each temperature. Table 3-2 provides the exact time intervals measured per temperature considering as a rule of thumb that the overall reaction rate doubles per 10 °C increase. For exploratory purposes, the effect of bitumen film thickness was also investigated at the highest temperature of 75 °C using a thin film apparatus (Figure 3-2) able to produce films as thin as 100 μm (0.1 mm). This was done by heating both the apparatus and the binder and then the apparatus passed on top of the binder pool to create the required thickness in a pastry-like fashion. Additionally, the effect of short-term ageing by means of laboratory RTFOT on the reaction kinetics was investigated for both film thicknesses at 75 °C, indicated as RTFOT+75 in Table 3-2.

After performing the ageing conditioning, the top surface of the bituminous samples A and B was measured in all the time intervals, temperatures and film thicknesses in FTIR, while for bitumen C was studied only for the time intervals at 50 °C. In addition, all the binders were tested in TOF-SIMS at the virgin state and after 8 days M-TFOT at 50 °C. In all cases, the film thickness was kept minimum in order to exclude, as much

as possible, the diffusion effect from the coupled reaction-diffusion phenomenon of ageing. By minimising the film it is assumed that the diffusion effect will be eliminated and primarily oxidation will be the dominant process [163–165]. However, instrumental constraints for the EPR analyses resulted in thicker films (3-5 mm) which were aged directly in polypropylene tubes and may have experienced different diffusion. Since in EPR analyses the entire bitumen sample was measured, the number of spins derived from the EPR spectra was divided by the exact mass of the sample in order to extract a fair comparison value independently of the small fluctuation of thickness compared to FTIR and TOF-SIMS films.

Table 3-2 Studied time intervals per oxidation temperature

Temperature (°C)	Time intervals (hours)	Film thickness (mm)
25	0/672/1344/2016/2688/3360	1.0
50	0/168/336/504/672/840/1008/1176/1344	1.0
75	0/8/24/96/168/336/504/672	1.0 & 0.1
RTFOT+75	0/8/24/96/168/336/504/672	1.0 & 0.1

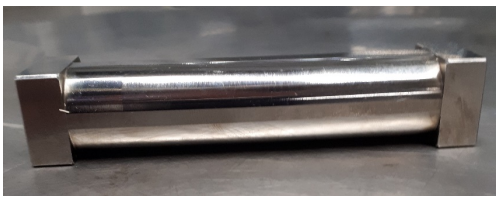

Figure 3-2 Thin Film applicator for bitumen

For the ease of the reader, a comparative overview by means of ageing ranking of the three binders per technique upon completion of the ageing kinetics at 50 °C, is given in Table 3-3.

Table 3-3 Ageing ranking per technique for the three binders after kinetics completion

Experimental technique	Ageing severity (increasing order)		
FTIR	A	B	C
EPR	C	A	B
TOF-SIMS	C	A	B
DVS	A	B	-

3.4 **Oxidation phases**

3.4.1 ***FTIR***

To track the oxidation phases assumed previously in the literature, focus was initially given exclusively on sulfoxides, which are more prone to be produced during oxidation

at lower temperatures, like the one studied (50 °C). A typical evolution of this index in kinetics at 50 °C is depicted in Figure 3-3 for bitumen A.

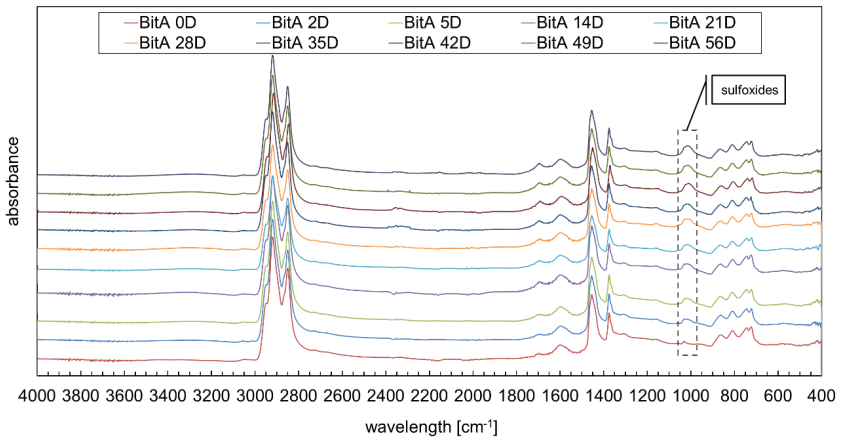

Figure 3-3 Spectra of the evolution of sulfoxides at 50 °C M-TFOT for bitumen A

The results of FTIR analyses show a steep increase of the sulfoxide index (normalised intensity) followed by a steady milder increase for all three binders (Figure 3-4). Binders A and C were found to have almost completed the initial rapid increase at about 5 days, whereas binder B reached this transition point at about 2 days. It becomes apparent that at 8 days of controlled ageing kinetics the slow-rate oxidation reaction has been initiated for all the binders.

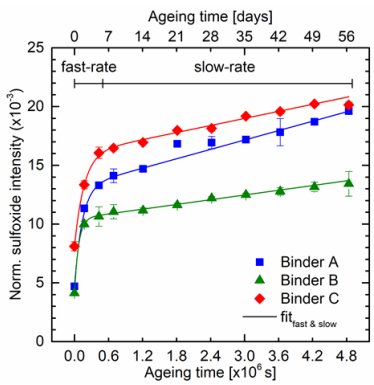

Figure 3-4 Evolution of the FTIR sulfoxide index over ageing time at 50 °C M-TFOT and the fitting used, based on a dual-sequential model [6,19]

Given that sulfoxides are considered to be one of the end products of both a fast and a slow reaction [18], oxidation kinetics were approximated in the following way for the product evolution. Assuming pseudo first-order kinetics and that the rate of the slow reaction is rather small, the evolution of an end product *P*, of a dual-sequential oxidation in a specific temperature can be described by Equation 3-1 [19].

$$P(t) = P_{f\infty}(1 - e^{-k_f' t}) + P_{s\infty} k_s' t + C \qquad \text{Equation 3-1}$$

where $P(t)$ is the amount of product as a function of time; $P_{f\infty}$ and $P_{s\infty}$ are amounts of product from the fast and slow reactions, respectively at the reaction endpoint; k_f' and k_s' are pseudo first-order rate constants of the fast and slow reactions, respectively; and C is a constant [19]. The FTIR results for all three binders can be reasonably fitted to Equation 3-1 with their parameters given in Table 3-4.

Table 3-4 Parameters used for fitting Equation 3-1 to the FTIR sulfoxide index at 50 °C M-TFOT and their R^2

Binder	$P_{f\infty}$ [×10^{-3} a.u.]	k_f' [×10^{-6} s^{-1}]	$P_{s\infty}k_s'$ [×10^{-6} s^{-1}]	C [×10^{-3} a.u.]	R^2
A	8.5 ± 0.2	7.3 ± 2.2	1.33 ± 0.03	4.69 ± 0.08	0.99
B	6.3 ± 0.1	13.8 ± 1.5	0.67 ± 0.04	4.14 ± 0.01	0.99
C	7.9 ± 0.7	5.9 ± 1.2	1.00 ± 0.07	8.12 ± 0.65	0.98

From this analysis, k_f' was determined to be fastest for binder B, followed by A then C. Moreover, the percentile increase of the normalised sulfoxide intensity of the virgin binder up to the completion of the ageing treatment used here, was evaluated. This percentile increase demonstrates that binder A suffered from a harsher oxidation effect (317.9 %) followed by binder B (224.5 %) and C (148.4 %), under the same ageing conditions.

Semi-quantitative methods to analyse the FTIR spectrum can be useful for identifying and characterising the evolution of specific oxidation products. Consistent with previous studies, this work demonstrated an initial rapid increase of sulfoxides followed by a slow-rate formation [6,18]. Hence, the kinetics of the sulfoxide index can establish a simple way to distinguish different oxidation rates. At least, they can give a rough estimation for the completion time of the fast-rate phase and the initiation of the slow one under the given oxidation kinetics.

3.4.2 *EPR*

The time-dependent evolution of the EPR spectra of the three binders was investigated in the same timeframe as with the FTIR, up to 56 days at 50 °C. The graphs in Figure 3-5 [right] and Figure 3-5 [left] respectively, show the evolution of the organic carbon-centred radicals and VO^{2+} species over ageing time. Interestingly, in all cases, the amount of VO^{2+} spins remained relatively constant as the samples were aged (a zeroth-order line can be fitted with the error bars), while an increase was observed for the organic carbon-centred radicals (Figure 3-5 [left]). A comparison of the binders used in this study indicates also that the relative increase of organic carbon-centred radicals

in binder C was about 1.5-2.0 times higher in comparison with binders A and B, while binder A keeps slightly increasing after 56 days.

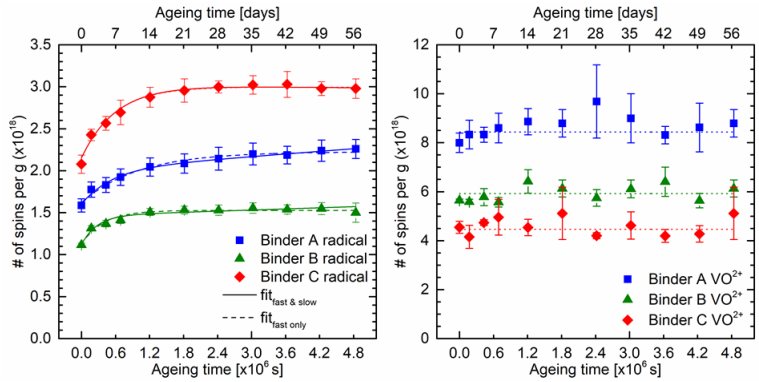

Figure 3-5 Evolution of the carbon-centred radical at 50 °C M-TFOT and the used fitting, based on a dual-sequential or a fast reaction model [left] and VO^{2+} centres over ageing time at 50 °C M-TFOT [right]

Although the results for the evolution of the carbon-centred radical EPR signal could also be fitted using Equation 3-1 (parameters given in Table 3-5), for each binder the contribution from the slow reaction term was almost negligible and for binder C it was even negative, which is contrary to a dual fast and slow production of end products model. These carbon-centred radicals are believed to be only produced and also subsequently consumed during the slow-rate phase. Since they are observable, their rate of production must be faster than their rate of consumption. In all cases, the evolution of the carbon-centred radical EPR signal is dominated by a mono-exponential component for the total radical evolution which strongly suggests that their rate of production is kinetically controlled by the fast-rate phase. This means that the previously hypothesised oxygen-centred free radicals, assumed by Petersen and his colleagues to be generated in the fast-rate phase [6], are able to immediately abstract protons attached to benzyl rings to yield carbon-centred radicals. In contrast, since the subsequent consumption of these carbon-centred radicals appears to be much slower, it must be governed by the overall kinetics of the slow-rate phase. Once the system enters the slow-rate phase, the rate of oxygen-centred free radical production and thus carbon-centred radical production will become comparable to their rate of consumption, and therefore, as can be seen in Figure 3-5 [left], no net increase in the amount of carbon-centred radicals is observed. Therefore, a two-phase oxidation scheme can still be supported by the obtained EPR results.

In line with these hypotheses, the k_f' values obtained for the radical production were within a similar range to those for sulfoxide production. Similarly, the k_f' for binder B was again the fastest, which suggests that both organic carbon-centred radicals and

sulfoxide production in the fast reaction may be controlled by the same rate-limiting process.

Table 3-5 Parameters used for fitting the EPR spin counting of the radical signal at 50 °C M-TFOT and their R^2

Binder	Reaction(s)	$P_{f\infty}$ [×10^{17} spins g^{-1}]	k'_f [×10^{-6} s^{-1}]	$P_{s\infty}k'_s$ [×10^{10} spins $g^{-1}s^{-1}$]	C [×10^{17} spins g^{-1}]	R^2
A	Fast & slow	4.1 ± 0.5	1.9 ± 0.4	5.2 ± 1.4	16.0 ± 0.2	0.98
	Fast only	6.1 ± 0.3	1.0 ± 0.1	N/A	16.0 ± 0.2	0.97
B	Fast & slow	3.4 ± 0.4	3.7 ± 0.9	2.2 ± 1.4	11.0 ± 0.2	0.97
	Fast only	4.0 ± 0.2	2.6 ± 0.4	N/A	11.0 ± 0.2	0.96
C	Fast & slow	8.7 ± 0.9	1.7 ± 0.3	-0.73 ± 0.02	21.0 ± 0.4	0.97
	Fast only	8.5 ± 0.4	1.8 ± 0.2	N/A	21.0 ± 0.4	0.97

It is interesting to mention that, in contrast to FTIR results, the harsher, relative to the unaged state, oxidation effect was observed for binder C. This difference can be explained by the fact that binder C was the result of a visbreaking process, which is a mild cracking process, resulting in radical formation. This can explain the higher initial organic carbon-centred radical concentration observed in bitumen C (Figure 3-5 [left]).

In addition, the VO^{2+} signal appears to stay constant over the ageing time in Figure 3-5 [right], for the three investigated binders. It can be exploited as an indicator of the vanadium content in petroleum [166]. Of particular interest is that this assignment seems to remain unaffected by ageing and could be potentially used as a marker for the origin of the bitumen.

Together the two spectroscopic techniques (FTIR and EPR) give evidence for the two rates of a dual-oxidation route. Given this, FTIR supports that between 2 and 5 days for all the examined binders the fast-rate reaction has finished, whereas EPR proves that carbon-centred radicals, which are believed to be produced and subsequently consumed during the slow-rate phase, actually evolve with the fast-rate phase kinetics. The fact that free organic carbon-centred radicals still exist after 56 days of M-TFOT ageing, suggests towards the continuation of the slow-rate oxidation phase until complete reaction/termination. The ageing time interval of 8 days was used afterwards for TOF-SIMS surface analyses to unravel the main products after the combined effects of the fast- and slow-rate phase.

3.5 **Oxidation products**

3.5.1 ***TOF-SIMS***

TOF-SIMS was used to analyse the molecular changes and oxidation products on the bitumen surfaces upon ageing. Positive and negative ion spectra were acquired for the three binders (A, B and C) in the unaged state and after 8 days of ageing, at which point the fast-rate phase is mainly completed and the slow-rate phase has been initiated. Representative spectra of the unaged and aged samples of bitumen A and C are presented in Figure 3-6 and ion assignments of peaks relevant to ageing are listed in Table 3-6 and Table 3-7. No clear changes due to ageing can be observed in the major peaks of the spectra, indicating that the effect of ageing on the molecular surface structure is relatively small. In contrast, clear differences can be observed between the spectra of bitumen A and C, mainly reflecting the wax content of bitumen C. As has been reported previously in the literature wax segregates effectively in bitumen to form a thin layer of wax, largely covering the surface, which can be observed in the spectra of bitumen C [167]. The higher intensities of peaks in bitumen C represent aliphatic species, whereas the spectrum of the wax-free bitumen A displays higher intensities of peaks representing aromatic species, as well as N- and S-containing organics.

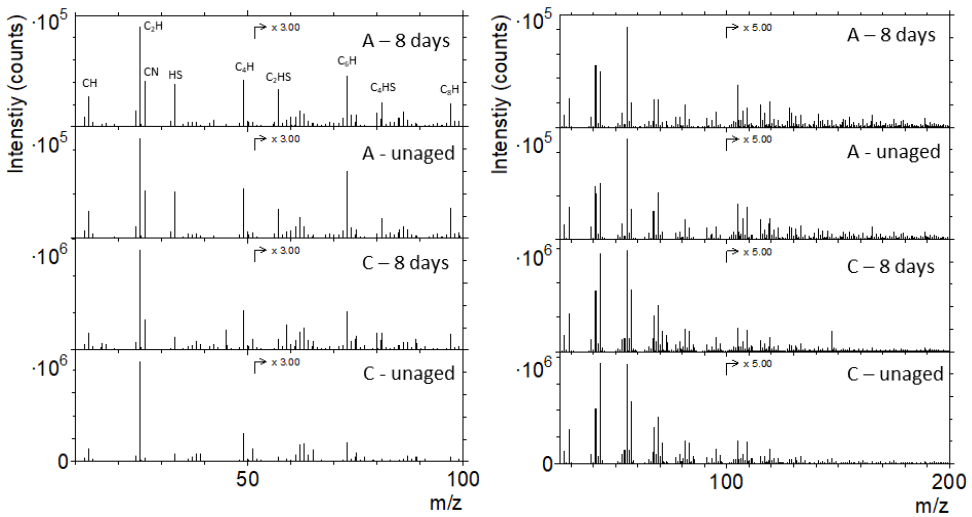

Figure 3-6 Negative [left] and positive [right] ion spectra of bitumen A and C before and after M-TFOT at 50 °C for 8 days

Table 3-6 Utilised oxygenated peaks for positive ions of TOF-SIMS

Ion	Observed mass (m/z)	Assignment of molecular structure
CH_3O^+	31.020	O_x-containing
$C_3H_5^+$	41.047	Aliphatic
$C_2H_3O^+$	43.020	O_x-containing
$C_3H_7^+$	43.066	Aliphatic
$C_4H_7^+$	55.068	Aliphatic
$C_4H_9^+$	57.087	Aliphatic
$C_3H_7O^+$	59.049	O_x-containing
$C_5H_7^+$	67.066	Aliphatic
$C_5H_9^+$	69.087	Aliphatic
$C_5H_{11}^+$	71.117	Aliphatic
$C_6H_9^+$	81.087	Aliphatic
$C_6H_{11}^+$	83.112	Aliphatic
$C_6H_{13}^+$	85.135	Aliphatic
$C_7H_{11}^+$	95.106	Aliphatic
$C_7H_{13}^+$	97.129	Aliphatic
$C_8H_{13}^+$	109.128	Aliphatic
$C_9H_7^+$	115.059	Aromatic
$C_9H_{11}^+$	119.105	Aliphatic
$C_{10}H_8^+$	128.068	Aromatic
$C_{13}H_9^+$	165.079	Aromatic

Table 3-7 Utilised oxygenated peaks for negative ions of TOF-SIMS

Ion	Observed mass (m/z)	Assignment of molecular structure
O^-	15.994	O_x-containing
OH-	17.004	HO_x-containing
CN^-	26.003	N-containing
$C_3H_2^-$	38.016	Aliphatic
$C_3H_3^-$	39.024	Aliphatic
C_2HO^-	41.006	HO_x-containing
CNO^-	42.002	NO_x-containing
CHO_2^-	45.001	HO_x-containing
$C_4H_3^-$	51.023	Aliphatic
CSO^-	59.967	SO_x-containing
SO_2^-	63.963	SO_x-containing
C_4HO^-	65.003	HO_x-containing
$C_5H_5^-$	65.038	Aliphatic
$C_2H_3SO^-$	74.989	SO_x-containing
$C_6H_5^-$	77.037	Aliphatic
SO_3^-	79.961	SO_x-containing
SO_4H^-	95.959	SO_x-containing
C_3NO^-	96.999	NO_x-containing

Although the major peaks in the TOF-SIMS spectra are essentially unchanged, the effect of ageing can be observed by consideration of oxygen-containing fragment ions, including SO_x-, NO_x- and O_x-containing organic ions, which are present at lower signal intensities and mainly in the negative spectra (see Table 3-6 and Table 3-7)**.**

The oxygen-containing fragment ions of the three binders were analysed based on normalised signal intensities and categorised into SO_x-containing (Figure 3-7 [left]) and HO_x-containing fragments (Figure 3-7 [right]). A strong increase in the intensity of the fragments with the generic formula RSO_x and RHO_x can be observed, indicating the formation of sulfoxide- and oxygen-related compounds as a result of ageing. Additionally, for all binders the amount of cyanate fragments, with generic formula RNO^-, also increased during oxidation. It is important to note here that signal intensities of the same ion can be compared to indicate concentration differences between samples of the specific species that it represents.

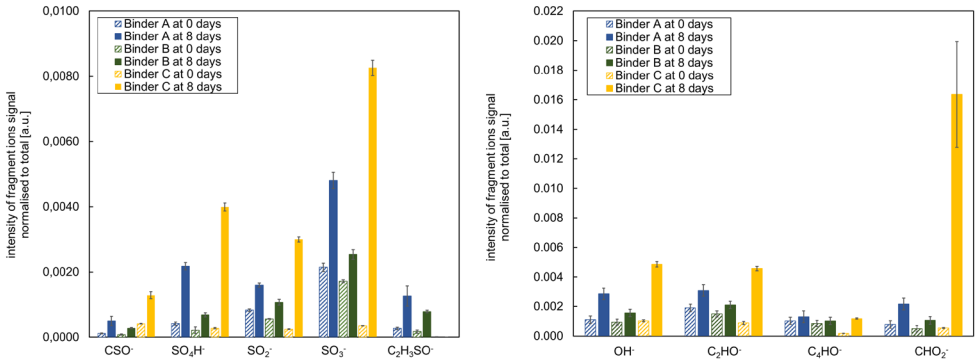

Figure 3-7 Intensity of SO_x-containing [left] and HO_x-containing compounds via TOF-SIMS for all three binders [right] before and after 8 days M-TFOT at 50 °C

Comparing the different binders, the relative effect of ageing is generally higher for bitumen A compared to bitumen B, but the strongest effect is observed for the wax-containing bitumen C. Furthermore, bitumen A and B show no effect of ageing on the intensities of fragment ions without oxygen content, including CN^- and aliphatic/aromatic hydrocarbon fragments. For bitumen C, however, ageing results in increased intensities of CN^- (Figure 3-8 [left]), as well as in hydrocarbon fragments representing aromatic species, and decreased intensities of aliphatic hydrocarbon fragment ions, see Figure 3-8 [right].

Next to sulfoxide formation during the slow reaction, alcohol groups may also be produced [6,168]. The sulfoxide intensity observed with FTIR has been assigned, up to now, completely to this functional group. However, an overlap with other HO_x-containing groups may exist in the corresponding infrared absorption band (around 1100 cm^{-1}), indicating that alcohols and sulfoxides may coincide. Whereas the origin of the increase of this infrared absorption band upon ageing is not clear, the observed increase of HO_x-containing fragments with TOF-SIMS is consistent with the formation of alcohols and/or carboxylic acids. However, a clear differentiation is not possible without a more elaborated statistical analysis and/or complementary chemical information. It can thus be speculated, in general, that ageing results in the formation of more polar species, e.g. alcohols or carboxylic acids, which then may affect the molecular interactions and eventually the rheology of bitumen.

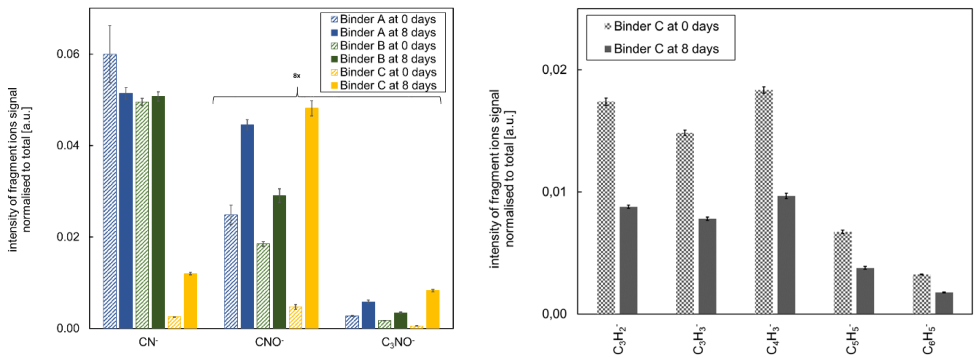

Figure 3-8 Intensity of nitrogen-containing compounds in all binders [left] and intensity of aliphatics in binder C [right] before and after 8 days M-TFOT at 50 °C

Previously [169,170], it was found that nitrogen-containing compounds can be identified in oxidised binders without significantly changing upon ageing [18]. In this study, the increase of RNO^- fragments indicates that additional oxidation products, those of nitrogen-containing compounds are present upon ageing, which should be possibly considered in a future oxidation scheme. It can also be expected that the concentration of the different heteroatoms may have an impact on the intensity of the different fragments.

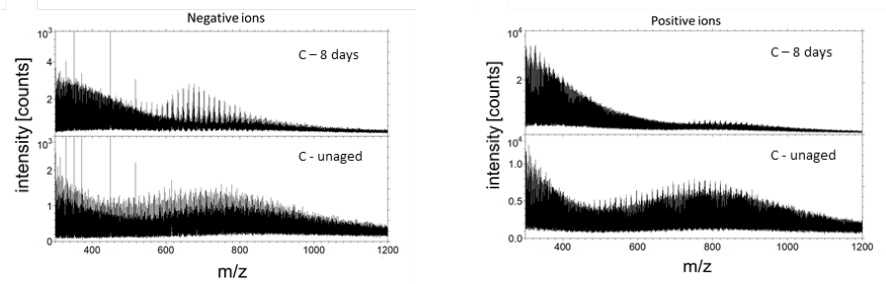

Figure 3-9 High mass range of negative [left] and positive ion spectra of bitumen C before and after 8 days M-TFOT at 50 °C [right]

In Figure 3-9, TOF-SIMS spectra of bitumen C are presented at a higher mass range, m/z = 350-1200, where the peaks to a larger extent correspond to intact or nearly intact molecular species. The envelope of peaks at m/z 500-1000 in both negative and positive ion spectra can be assigned to intact wax molecules, as previously articulated by Lu [167], for which the intensity reduction upon ageing is consistent with the reduced intensities of the aliphatic fragment ions upon ageing (Figure 3-8 [right]). Interestingly, ageing of bitumen C produces a new envelope of peaks at m/z 600-800 in the negative ion spectrum. Although unambiguous identification of these peaks is not possible due to the limited mass resolution, mass separation of m/z = 14 between equivalent peaks and the exact mass of the peaks is consistent with molecules comprised of nearly saturated aliphatic hydrocarbon chains with an added SO_x

functional group. For example, a peak observed at m/z 689.63 is consistent with $C_{45}H_{85}SO_2$, containing both an aliphatic and a small aromatic structure in which the S=O may be included. The latter may be taken as a consequence of oxidation and its subsequent sulfoxide formation.

For the positive ions, the effect of ageing was mainly observable in binder C. A clear increase in the intensities of O-containing organic ions was observed, reflecting the formation of oxidation products on the bitumen surface (Figure 3-10). Furthermore, positive ions of aliphatic fragments show a decreasing trend as can be seen in Figure 3-10, in contrast to PAH which increase upon ageing (Figure 3-11), consistent with the observations for the negative ions (Figure 3-8 [right]).

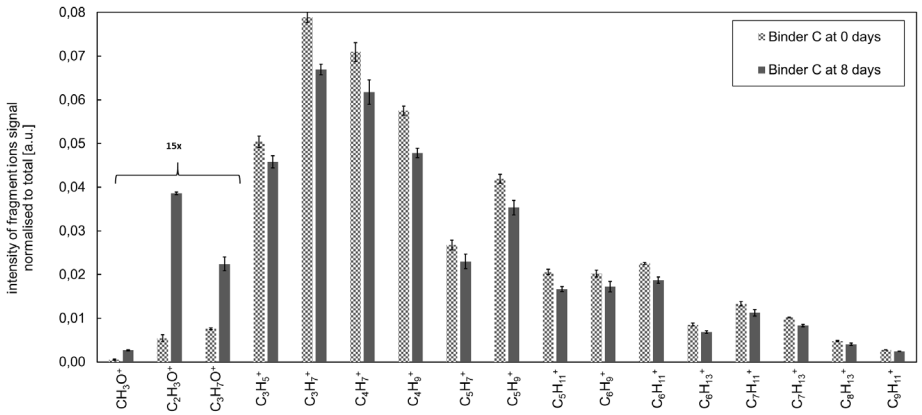

Figure 3-10 Intensity of O-containing and aliphatic fragments in selected positive ions before and after 8 days M-TFOT at 50 °C for bitumen C

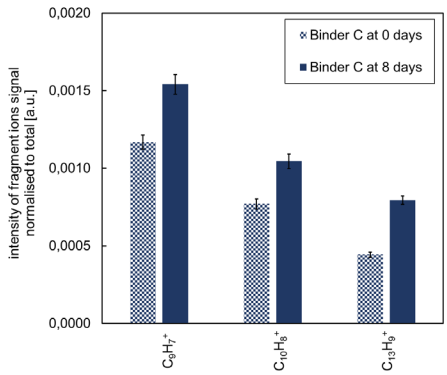

Figure 3-11 Intensity of PAH fragments in selected positive ions of bitumen C before and after 8 days M-TFOT at 50 °C

Finally, in order to investigate the spatial distribution of the wax fraction and the ageing-related molecular species on the surface of bitumen C, high-resolution TOF-SIMS images were generated (Figure 3-12). A clear phase separation with a governing

aliphatic phase is observed, with particles about 5-10 µm in size which covered most of the surface. Apparent wax-related particles (represented by aliphatics) cover most part of the surface and the spaces between these particles display increased signal intensities of ageing-related ions, such as O^-, CN^- and $(H)SO_x^-$ (Figure 3-12), as well as aromatics.

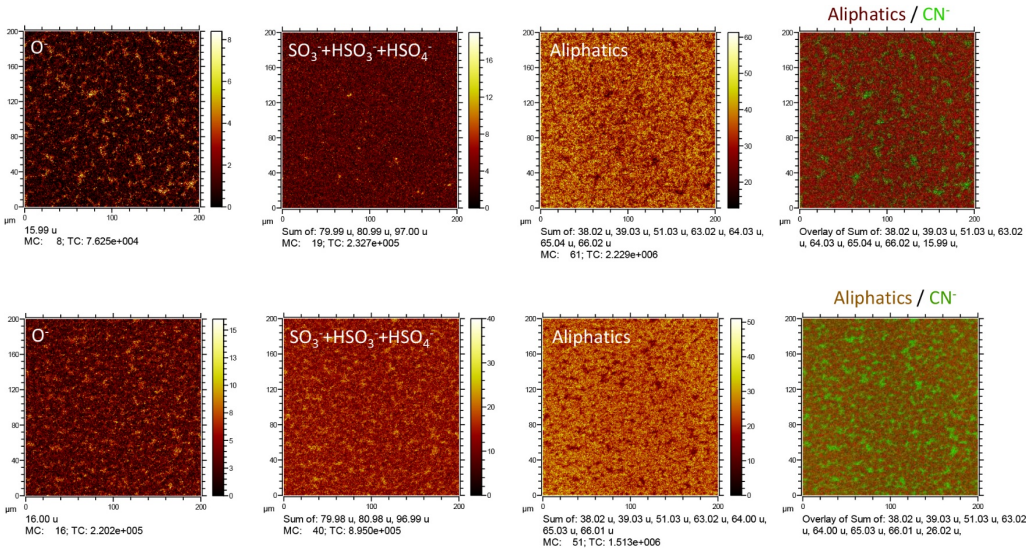

Figure 3-12 High-resolution TOF-SIMS images of selected negative fragment ions on the surface of bitumen C before [top] and after 8 days M-TFOT at 50 °C [bottom]. The signal intensities in the images are given as the maximum number of ion counts per pixel (MC) and total ion counts in the entire image (TC)

3.6 **Reactivity and diffusivity**

3.6.1 ***FTIR***

Exploration of the reaction kinetics of three different isotherms and two film thicknesses in FTIR was conducted for binders A and B by employing the sum of the ageing indices of carbonyls and sulfoxides. The results of the oxidation kinetics in Figure 3-13 were fitted assuming a first-order reaction rate expression according to Equation 3-2, where *k* is the reaction rate coefficient, *t* is the ageing time interval and *P* is the sum of the oxidation products of carbonyl and sulfoxide, assumed herein independent of oxygen concentration.

$$\frac{\partial P}{\partial t} = k(1-P) \qquad \textit{Equation 3-2}$$

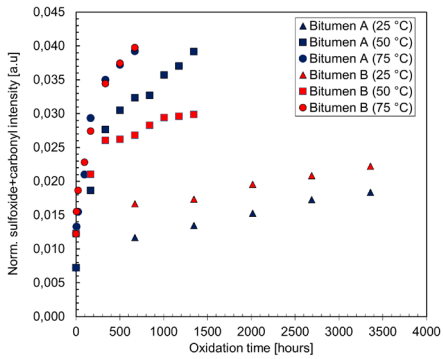

Figure 3-13 Experimental data points of FTIR ageing indices at the three isotherms for M-TFOT at 50 °C of 1 mm thickness

Assuming the effect of oxidation temperature *T* on the oxidation reactions, an Arrhenius type equation can explain the reaction rate based on Equation 3-3, where E_a is the activation energy, *R* is the universal gas constant and *A* is the reaction factor.

$$k = A \cdot e^{E_a/RT} \qquad \textit{Equation 3-3}$$

Fitting the oxidation kinetics data of Figure 3-13, based on Equation 3-2 and extracting the reaction rates (Table 3-8) allows the estimation of the activation energy by linear fitting of the natural logarithm of the rate constant versus *1/RT* at three temperatures (Figure 3-14).

Table 3-8 Reaction rates of a first-order reaction

Temperature (°C)	Film thickness (mm)	k (bitumen A) (1/h)	k (bitumen B) (1/h)
25	1.0	3.78 E-06	3.34 E-06
50	1.0	2.05 E-05	1.06 E-05
75	1.0	6.11 E-05	5.08 E-05
75	0.1	7.65 E-05	5.89 E-05
RTFOT+75	1.0	2.81 E-05	2.62 E-05
RTFOT+75	0.1	3.55 E-05	3.21 E-05

The results of Table 3-8 reveal that there is an increasing trend of the reaction constants for both binders with increasing reaction temperature, which confirms the validity of the Arrhenius temperature dependency of the *k* constants. Interestingly, the reaction constants at 75 °C show that kinetics of the samples previously subjected to RTFOT, experience a slower reaction rate which is almost halved. Moreover, the findings of the two investigated film thicknesses at 75 °C support that for thinner films of 100 µm the reaction is the governing process of the coupled reaction-diffusion phenomenon, which is in line with the slightly higher rate constant compared to the 1 mm films for both the unaged and RTFOT aged binders.

Comparing the two binders, bitumen B shows a lower rate constant at all temperatures, while Figure 3-14 depicts the goodness of fitted activation energies as expressed by the high coefficients of determination. Based on this fitting, bitumen B shows a lower E_a=46.7 KJ/mol compared to the slightly higher one of bitumen A (E_a=48.2 KJ/mol), which indicated that bitumen B has slightly higher temperature sensitivity.

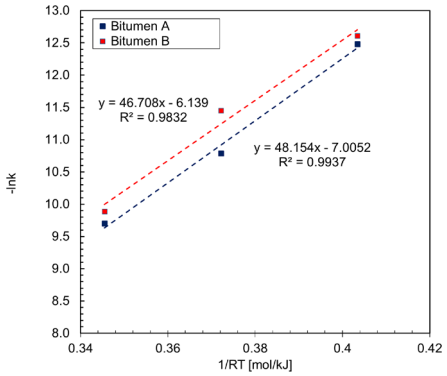

Figure 3-14 Linear fit for the extraction of activation energies

3.6.2 ***DVS***

The experimental results of the DVS tests for the corresponding bituminous mastics are given over time in Figure 3-15. It can be seen that both mastics of bitumen A and B are not able to reach the saturation level (plateau) within the specified testing time. However, the acquisition of data points for the change of mass allows for the back-calculation of parameters governing the reaction procedure and, thus, the prediction of the terminal time with completed oxidative reactions. To succeed this, traditional Fickian laws have been revised by scholars with the potential to account for both effects and to discuss more accurately the effect i.e. on oxygen diffusivity [19]. Past studies have reported values for the diffusion coefficients of oxygen in bitumen ranging between 10^{-10} m^2/s and 10^{-15} m^2/s [171].

Simulations and optimisations in a multiphysics Finite Element (FE)-based software package (COMSOL version 6.0) were performed assuming a reaction-diffusion model for the DVS data of the following Equation 3-4 [110], where c_{O_2} is the concentration of O_2, D is the oxygen diffusion coefficient, k *is* the oxygen reaction constant and c_B is the concentration of reactive bitumen components.

$$\frac{\partial c_{O_2}}{\partial t} = D\nabla^2 c_{O_2} - k c_B c_{O_2} \qquad \textit{Equation 3-4}$$

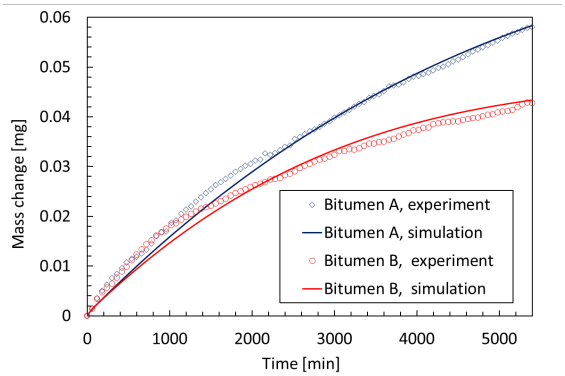

Figure 3-15 DVS experimental data and optimised FE simulations for the mastics of binders A and B

Figure 3-15 depicts the convergence between the experimental results and model simulations that can accurately predict the overall diffusion and reaction evolution. Based on the optimisation of the reaction-diffusion model by unitising experimental data from DVS, useful parameters can be extracted, presented in Table 3-9. The diffusion coefficient can therefore be predicted for bitumen mastics and considering that the filler remained unchanged during the DVS tests, this coefficient has also an application for the corresponding binders A and B. In addition, the range of these coefficients lies well within the values reported previously in the literature [110]. With regard to the reaction rates, they are rather underestimated as compared to a pure reaction model of Equation 3-2, while they are in agreement with the trend found previously in Table 3-4. This can be explained by the fact that a coupled reaction-diffusion model accounts for more details i.e. the oxygen supply and gradient in the film, as oxidation kinetics evolve at 75 °C.

Table 3-9 Simulated FE reaction-diffusion parameters based on modified Fickian law

Property	Mastic of bitumen A	Mastic of bitumen B
O_2 solubility [mol/m^3]	0.940	1.079
D [m^2/s]	8.26 E-11	7.90 E-11
k [m^3/(s·mol)]	7.83 E-06	1.03 E-05
c_B [mol/m^3]	59.381	37.497

Finally, the values of oxygen concentration at the ideal saturation level can be obtained via the FE simulated model and by definition are equal to the oxygen solubility in mastics and respectively in bitumen. The predicted values are also within the range of previously reported values in literature [19,110]. All in all, comparing the two binders A and B they present similar values for the diffusion coefficient while bitumen B exhibits higher oxygen solubility. It is finally worth noting that the reactive component concentration of bitumen A is higher than that of bitumen B. SARA analysis of bitumen

A (see Chapter 8), corroborates this observation as it showed higher asphaltenes and resins percentage.

3.7 Highlights of the chapter

- FTIR supports the hypotheses of two rate-determining oxidation phases, a fast- and a slow-rate and a rapid sulfoxide formation during the fast-rate phase.
- The completion point of the fast-rate phase has been reached for all binders around 8 days under oxidation kinetics at 50 °C via FTIR and EPR.
- EPR measurements demonstrate that the overall amount of organic carbon-centred radicals evolves predominantly with the fast-rate phase.
- EPR also shows that in this study vanadyl-porphyrin species remain unchanged during lab ageing kinetics.
- FTIR and TOF-SIMS spectrometry indicate that sulfoxide-, nitrogen- and oxygen-containing compounds, e.g. alcohols and/or carboxylic acids, are formed after the occurring fast- and slow-rate phases.
- An increase of aromatics and the accompanying decrease of aliphatics is only observed for the visbroken, waxy binder.
- RTFOT short-term ageing influences the reaction rate constants of a universal first-order reaction kinetics model.
- DVS in combination with FE model simulations can rather adequately estimate the diffusion coefficient of mastics and bitumen in the case that an inert filler is used.
- The oxygen solubility, diffusion coefficient and reactive components concentration of the binders of this work agree well with reported values in literature.

Overall, the insights gained from this Chapter may be particularly interesting for laying the groundwork for the underlying oxidation mechanisms in bitumen with standardised lab ageing simulations, examined in Chapter 4.

4

AGEING MECHANISMS IN BITUMEN VIA STANDARDISED LAB SIMULATIONS

4.1 **Summary**[*]

Chapter 4 focuses on the identification of the intermediate and final oxygenated products after short- and long-term laboratory ageing simulated with RTFOT and PAV respectively. Three binders were investigated in this study, two originated from the same wax-free crude source, while the third was obtained from a different source, containing natural wax, and followed a different manufacturing process. FTIR spectroscopy demonstrated a clear increase of the sulfoxide and carbonyl functional groups upon ageing for all the binders independently of origin, manufacturing or performance. EPR spectroscopy showed an increase of the organic carbon-centred radicals after short-term ageing (RTFOT), whereas after PAV ageing these radicals remained constant in the two wax-free binders originating from the same crude source, and even decreased for the third, waxy binder. ^{1}H-NMR spectroscopy reported differences in the relative distribution of protons between the binders in the unaged state, and similar minor changes after both ageing steps regardless of the binder's crude source and distillation. The results of TOF-SIMS revealed that SO_x- and $(OH)_x$-containing compounds are produced after the sequentially occurring short- and long-term ageing in both wax-free binders, whereas an almost constant behaviour of aliphatics after PAV ageing can be seen for the same binders. In addition, the SARA

[*]*This chapter is redrafted from: G. Pipintakos et al., Exploring the oxidative mechanisms of bitumen after laboratory short- and long-term ageing, Construction and Building Materials (2021). https://doi.org/10.1016/j.conbuildmat.2021.123182*

X. Lu et al., Analysis of asphaltenes and maltenes before and after long-term aging of bitumen, Fuel (2021). https://doi.org/10.1016/j.fuel.2021.121426

fractions of the waxy and the softer straight-run binder were also investigated by FTIR, ^{1}H-NMR and DSC before and after RTFOT+PAV and the findings support that a large part of carbonyls and sulfoxides upon ageing shifts to the asphaltenes, while waxes can mainly be found in the maltenes fraction.

4.2 **Objectives**

Artificial lab ageing simulations are widely used in the asphalt sector, as it is believed to capture more realistically the view of bitumen in-situ than kinetics and accelerate considerably the lab simulation. It is of importance to examine if the hypotheses about the ageing mechanisms via kinetics account for a fair correspondence with standardised lab simulations of bitumen. Thus, Chapter 4 aims primarily to identify the basic ageing compounds (radicals, ions, protons and chemical products) formed after artificial ageing. Specifically, the proposed approach employs the most appropriate advanced spectroscopy (FTIR, EPR, ^{1}H-NMR and TOF-SIMS), described in Chapter 2, in an attempt to capture the structural and chemical changes upon ageing with routine laboratory tests. It manages also to account for the effect of both the crude source, the binder's penetration grade and the distillation process on the mechanisms upon standardised ageing. The distribution of the oxygenated products in the different bitumen fractions (asphaltenes and maltenes) is also investigated via spectroscopy and DSC. The methodology adopted in this Chapter alongside the main objectives is shown schematically in Figure 4-1.

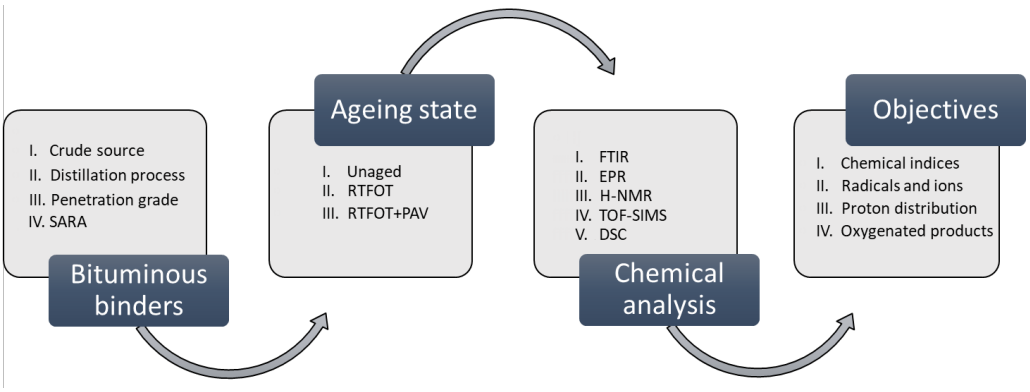

Figure 4-1 Flowchart of the experimental part of Chapter 4 and objectives

4.3 Materials and Methods

The same bituminous binders A, B and C (Table 3-1) explored via kinetics were used also in this Chapter to reveal differences related to the crude source, refinery process and wax presence.

The oxidative ageing in the lab was simulated for the short term-ageing by RTFOT according to EN 12607-1 [40] and for the long-term ageing with the PAV according to EN 14769 [41]. Typically for RTFOT, 35 grams of unaged virgin bitumen are placed in each bottle inside a rotating carousel for 75 minutes, where temperature and fresh air flow are set at 163 °C and 4 L/min. This test simulates the high temperatures occurring during the production and is linked with the initial fast-rate oxidation phase of a dual-sequential oxidation scheme. The PAV protocol, on the other hand, was followed for all the RTFOT aged samples, in an attempt to reproduce in a short period of time the effect of many years in the field. The PAV procedure requires 50 grams of bitumen to be placed in pans inside a pressure chamber, which results in a thin film of bitumen able to be sufficiently aged. In the current investigation, the temperature was set at 100 °C with an air pressure of 2.1 MPa for a total duration of 20 hours. In order to simplify the nomenclature for each ageing state of the three binders, the following code 'X-ageing state' indicates the type of binder X (A, B or C) and the ageing state (Unaged, RTFOT or PAV).

An overview of the ageing ranking of the three binders per technique as well as their overall rheological evaluation after PAV, is given in Table 4-1.

Table 4-1 Ageing ranking per technique for the three binders after PAV

Experimental technique	Ageing severity (increasing order)		
FTIR	A	B	C
EPR	C	A	B
TOF-SIMS	C	A	B
^{1}H-NMR	C	B	A
DSR	C	B	A

To investigate additionally the effect of lab ageing on the fractions, SARA separation in the straight-run bitumen B and the waxy bitumen C was additionally performed according to DIN 51595. Based on this protocol, about 60 g of hot bitumen are poured into an Erlenmeyer flask, where n-heptane solvent is added in a ratio of 100 mL of solvent per 1 g of sample. After slightly heated on a hot plate, the Erlenmeyer flask is shaken until all the bitumen is partially dissolved and the other part precipitates. The solution with the precipitates (asphaltenes) is cooled to room temperature for 30 minutes. Then a first filtration is performed on a Whatman 41 filter paper. The asphaltenes on the filter paper are washed repeatedly with the hot solvent until the

filtrate becomes colourless. After drying the filter paper, the precipitates can be collected in a beaker. The dried asphaltenes are washed one more time with n-heptane and are filtered on a vacuum filter. Maltenes fraction can also be collected from all n-heptane solutions after removing the solvent by a rotary evaporator. Therefore, asphaltenes in a powder-like state and maltenes in the virgin and after the sequentially occurring RTFOT+PAV state were further used in the analytical methods.

4.4 **Oxidation products in bitumen**

4.4.1 ***FTIR***

The indices presented in Equation 2-1 to 2-4 were determined for the three bituminous binders under investigation before and after laboratory short (RTFOT) and long-term ageing (PAV). The results are consistent with the view that an increase in ageing severity is observed after standardised ageing for the main oxidative indices, namely the sulfoxide and the carbonyl index [46,172]. Figure 4-2 depicts the evolution of the two indices and the effect of each ageing state is discussed herein in percentage increase of the virgin state.

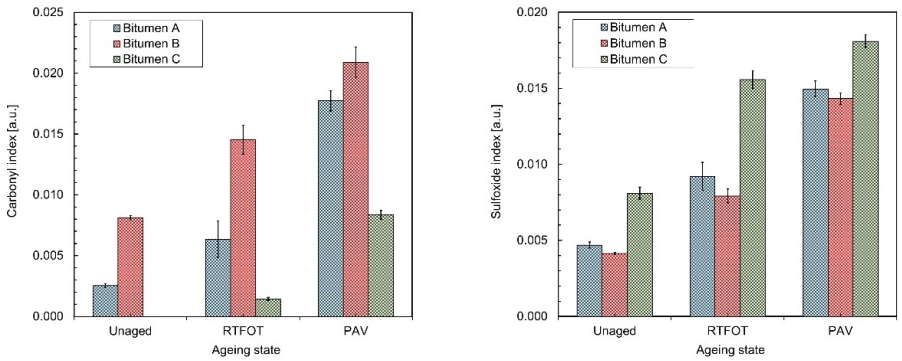

Figure 4-2 Evolution of carbonyl [left] sulfoxide index [right] with lab ageing

A relative comparison of the formation rates can be performed in terms of percentage differences. The results of bitumen A for the carbonyl index show an increase of 150.7% and 600.1% after RTFOT and PAV respectively, which indicates a more rapid and steep increase compared to bitumen B (79.2% and 157.5%) which differed only in empirical performance (Figure 4-2 [left]). The presence of carbonyl groups for these two binders in the unaged state can be explained by the acidic nature of the crude oil from which they originated. On the contrary, for bitumen C-Unaged, a negligible initial carbonyl index was obtained based on the same analysis procedure. As such percentage differences are meaningless for bitumen C after RTFOT (with an initial

unaged index equal to zero), but an increase in carbonyls after RTFOT ageing is clear. The significant increase of carbonyls is apparent in bitumen C after PAV which increased (484.7%) compared in this case with the index in RTFOT. Therefore, it can be speculated that the carbonyl formation rate was even faster for bitumen C than A, although a numerical straight-forward comparison of the percentage increase cannot be performed.

A detailed inspection of the initial sulfoxide index for C-Unaged implies that this is significantly higher than for bitumen A and B. Concerning the sulfoxide index the three bituminous binders show a similar percentage increase after RTFOT (A-95.3%, B-91.4% and C-91.9%). The effect of the bitumen type seems to be very small on the sulfoxide formation rate after short-term ageing but after PAV ageing the sulfoxide indices increase more for binders A and B (A-218.9%, B-246.0%) compared to the increase of the sulfoxide index of bitumen C (123.1%).

Overall, the bitumen type has little effect on the sulfoxide formation rate but seems to affect the carbonyl formation differently. On the other hand, straight-run bitumen from the same crude shows a similar increase of sulfoxide upon ageing in the lab, with the hard bitumen A exhibiting a more rapid carbonyl increase compared to bitumen B.

The representative indices (Equation 2-3 and 2-4) for the aromatisation of bitumen were also investigated in this Chapter. In the past, it has been assumed that aromatisation increases primarily the planarity of perhydroaromatic rings in the fast-rate reaction but it can also cause the aromatisation of alkyl-substituted naphthenic rings during the slow-rate phase [18,173]. Moreover, an interplay between the formation of aromatic structures and a reduction of aliphatics (occurring in a lesser amount) can be hypothesised, which would result in a mutual change of the aromaticity and the branched aliphatic index. Surprisingly in this investigation, the FTIR indices related to these compounds were constant for both the aromaticity and branched aliphatic index in all the ageing states (Figure 4-3). It was postulated that FTIR was not sensitive enough to capture changes related to aromatisation with the suggested protocol followed herein for the index calculation. Moreover, alcohol regions around 3200-3500 cm^{-1}, seem not to be affected by ageing for all the binders, whereas an overlap in the C-O stretch of possible alcohol formation could exist with the sulfoxide increase in the FTIR spectra.

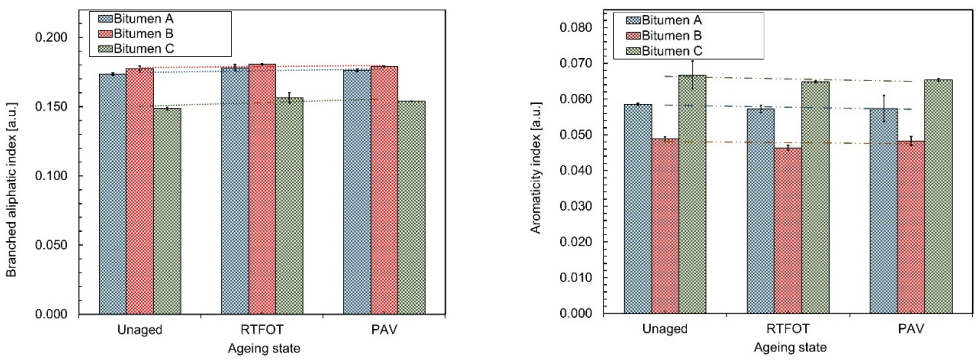

Figure 4-3 Branched aliphatic [left] and aromaticity index [right] with lab ageing

4.4.2 ***EPR***

The evolution of the organic carbon-centred radicals and the VO^{2+} species after routine laboratory ageing simulations is given in Figure 4-4. Overall, the carbon-centred organic radicals showed an increase after short term-ageing with RTFOT for all the three bituminous binders of this work with a significant drop in the number of spins for bitumen C observed upon PAV. Bitumen A and B kept a constant number of spins of carbon-centred organic radicals between short- and long-term ageing. The previous kinetics' study of Chapter 3 suggested that the oxygen-centred radicals, such as $^{\bullet}OH$, may abstract protons attached to benzyl rings and could yield to carbon-centred radicals [30]. The point at which the plateau of this type of radicals appears is considered the onset of the slow-rate phase. Hence, the differences between bitumen A, B and C suggest that the intermediate oxidation products, such as the organic carbon-based radicals, are affected differently by ageing. Furthermore, the different initial higher number of organic radical spins in bitumen C is possibly related to the visbreaking process of this bitumen. In general, the free organic carbon-centred radicals appear already in the unaged samples and this may be a critical parameter for the subsequent ageing severity of each bitumen.

When it comes to the VO^{2+} centres, identified with the EPR analyses, the present work confirms for these metal ions earlier observations of Chapter 3, namely that these centres remain in general unaffected by the oxidation process, as it is evidenced by the stabilisation of the number of spins in all the ageing states (Figure 4-4 [right]). This again raises a significant point about a possible correlation between the vanadyl species and the vanadium content, present in bitumen's composition since it can be exploited as an indicator and marker of the origin following [166].

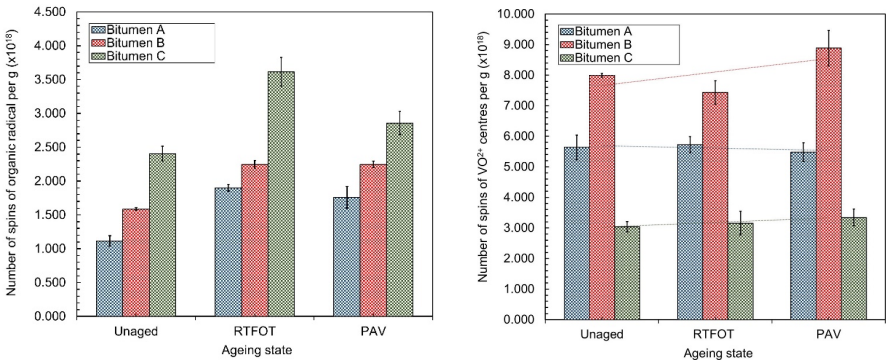

Figure 4-4 Evolution of carbon-centred radicals [left] VO^{2+} centres [right] with lab ageing

Up to this point, the differences between bitumen C and binders A and B may affect the initial number of spins of organic radicals in the unaged state. The different penetration grade between bitumen A and B implies also that the distillation grade of the same crude oil may have an effect on the VO^{2+} centres with the softer bitumen B presenting the higher number of VO^{2+} centres spins.

4.4.3 *^{1}H-NMR*

Spectroscopic ^{1}H-NMR analyses were evaluated to gain insights into possible changes of proton distribution upon ageing and thus the chemical composition of bitumen. An inspection of the spectra in all the ageing states for bitumen A (Figure 4-5) revealed a large peak at 0.90 ppm assigned to alkyl (methyl) protons and a peak at 1.28 ppm related to alkyl (methylene) protons, something which was observed also for binders B and C. After long-term ageing with PAV, bitumen A showed a peak around 1.67 ppm ascribed to alkyl (methine) protons. The same peak was observed already for bitumen B-RTFOT and C-RTFOT with the intensity of the peak increasing after PAV. The broader peak between 2.00-2.30 ppm can be assigned to protons on C_{α} next to carbonyl and the peak at 2.30 ppm can be assigned to a benzylic proton. No significant peaks were observed in the olefinic proton region (4.00-6.00 ppm) in any of the ageing states. The broader signal from 6.50 to 8.50 ppm is related to the aromatic protons.

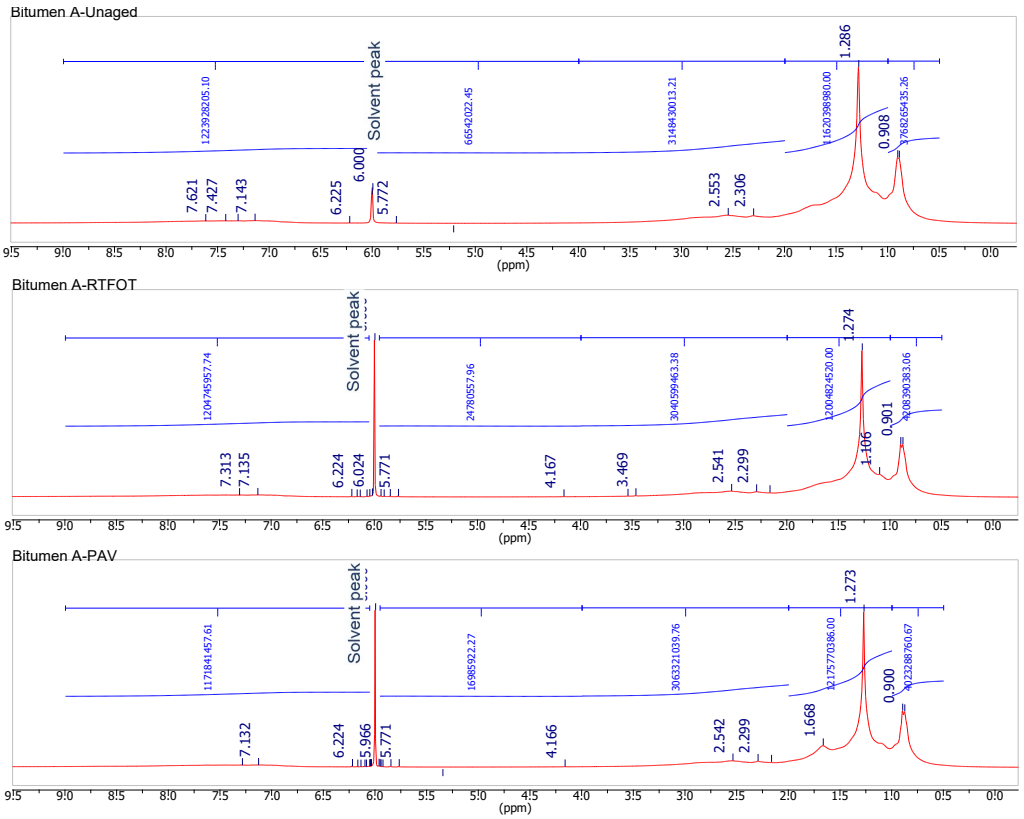

Figure 4-5 Example of ^{1}H-NMR spectra in all the ageing states of bitumen A with their main proton peaks and regions

Although spectral peaks appear somewhat similar apart from the prominent peak at 1.67 ppm upon ageing, integration of specific regions given previously in Table 2-3 (for which relative percentage distribution was determined) allows for the discussion of the chemical alterations upon standardised ageing. The relative occurrence of protons in different chemical environments/ageing states is given in Figure 4-6. All the analysed samples present a negligible presence of olefinic protons independent of the bitumen's ageing state. For clarity, the standard deviations of this specific region are not presented, whereas standard deviations of all the other regions are included in Figure 4-6. In binders A and B, the governing region seems to be the methylene, followed by methyl, α-alkyl and aromatic proton regions, while for bitumen C the methyl and α-alkyl region appeared in different decreasing percentage order. The main differences between bitumen A and B are the lower methyl region and the higher methylene region for bitumen A. Since methylene is the region that contributes predominantly to the total spectral region of the aliphatic protons ($=H_{methylene}+H_{methyl}+H_{\alpha\text{-}alkyl}$) its lower percentage for bitumen B is reasonable based on the different distillation grade of the two bituminous binders. In addition, bitumen A

and B differ from bitumen C mainly by the lower fraction in the aromatic and the higher fraction in the methyl regions.

The effect of the ageing state with regard to the relative percentage of protons was also assessed and presented in Figure 4-6. More specifically, in the hard bitumen A, the methylene proton region appears to increase slightly from 59.0% in A-Unaged to 59.5% in A-RTFOT and remains constant in A-PAV (59.6%). The aromatic protons follow the opposite trend (6.0% for A-Unaged to 5.5% for A-PAV). The region linked with the methyl protons fluctuated for bitumen A (19.3% - A-Unaged, 19.8% - A-RTFOT, 19.1% - A-PAV).

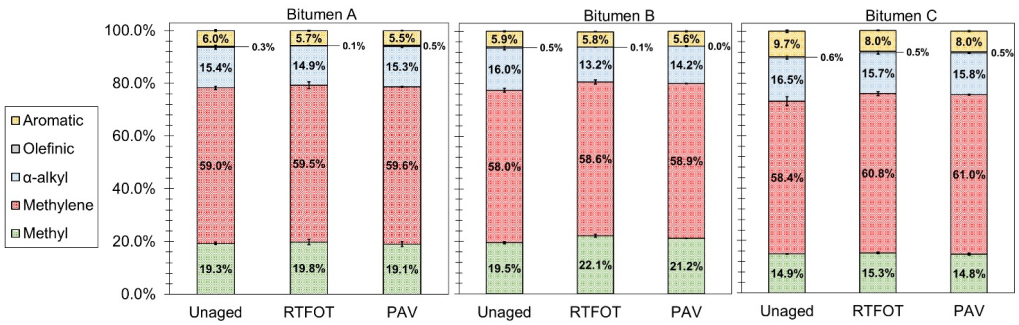

Figure 4-6 Relative percentage distribution of protons in different ageing states of bitumen A, B and C

Bitumen B originating from the same crude oil presents a similar relative percentage proton distribution after laboratory short- and long-term ageing. It is interesting that the α-alkyl proton zone from 16.0% in B-Unaged decreased in B-RTFOT (13.2%) and PAV (14.2%) compared to the unaged state. A fluctuation for the methyl protons was observed for bitumen B (increased percentage after RTFOT and decreased percentage values upon PAV), a trend which was observed also for bitumen A. Changes in the methylene proton region showed also an upward relative percentage trend with ageing.

Bitumen C, which gave the most apparent difference in the FTIR and the EPR results, showed a different initial proton relative percentage distribution compared to A and B-Unaged (higher aromatic and α-alkyl proton percentages, lower methyl proton percentages) but demonstrated, in general, the same trends with ageing. More specifically, bitumen C showed a decreasing trend after short-term ageing with RTFOT for the α-alkyl proton region shifting respectively from 16.5% in the C-Unaged to 15.7% in C-RTFOT and in 15.8% in the C-PAV, something which was observed also for bitumen B. Similar to binders A and B, increasing trends in the methylene and methyl proton regions of bitumen C were also observed, with the methyl proton region increasing with RTFOT ageing. The aromatic region appeared to decrease with ageing for bitumen C.

Obstacles of exploratory studies to identify chemical differences upon ageing in ^{1}H-NMR were overcome by grouping the main proton categories, acknowledging always the limitations that may exist for the application of this technique to bitumen. Therefore, bitumen A and B exhibited in general similar relative percentage distribution of protons as expected for the same crude oil in the unaged state but also upon laboratory ageing where the percentage distribution of protons was quite similar.

4.4.4 *TOF-SIMS*

Molecular investigation of the oxygenated products after the combined effect of short- and long-term ageing was conducted with TOF-SIMS on the surface of the three bituminous samples. It has been noted that ageing may affect the compatibility of the wax present in bitumen C to appear more pronounced upon ageing on the surface of the films. Although clear differences cannot be seen between the different ageing states i.e. in the spectra of bitumen A (Figure 4-7) a thorough inspection of certain fragment ions assisted to form a more clear view of the products. M/z values in the negative ion spectra of all the bituminous tested samples were classified into groups of ion fragments with generic formulas RSO_x and RHO_x given in Table 4-2. Selected m/z values in the positive ion spectra were assigned to aromatic and aliphatic ion fragments (Table 4-2).

The findings of the $(OH)_x$-containing fragments of bitumen A and B and partially for bitumen C point out that other products such as alcohols/ethers or carboxylic acids can be formed. This is evident by the higher intensity of most of the $(OH)_x$-containing fragments (attributed possibly to alcohols) after PAV compared to the unaged state which was not observed for specific ion fragments (C_2OH^-, C_6OH^-) of bitumen C (Figure 4-8 [left]), most probably as a result of the prominent presence of wax in its surface.

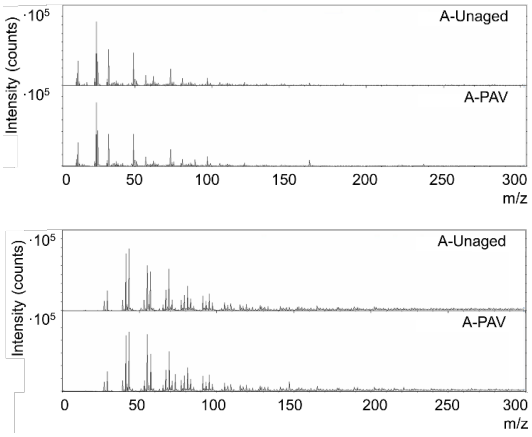

Figure 4-7 Example of negative [top] and positive [bottom] TOF-SIMS ion spectra of bitumen A in the unaged state and after PAV.

Table 4-2 Utilised negative and positive oxygenated ion fragments before and after PAV

Ion	Observed mass (m/z)	Assignment of molecular structure
OH^-	17.003	$(OH)_x$-containing
C_2OH^-	41.005	$(OH)_x$-containing
$CHSO^-$	60.974	SO_x-containing
C_2H_3SO	74.989	SO_x-containing
C_6HO^-	89.001	$(OH)_x$-containing
$C_3H_7^+$	43.055	Aliphatic
$C_4H_7^+$	55.054	Aliphatic
$C_4H_9^+$	57.070	Aliphatic
$C_5H_7^+$	67.049	Aliphatic
$C_5H_9^+$	69.068	Aliphatic
$C_5H_{11}^+$	71.088	Aliphatic
$C_6H_9^+$	81.065	Aliphatic
$C_6H_{11}^+$	83.085	Aliphatic
$C_6H_{13}^+$	85.104	Aliphatic
$C_7H_{11}^+$	95.079	Aliphatic
$C_7H_{13}^+$	97.102	Aliphatic
$C_9H_7^+$	115.033	Aromatic
$C_{10}H_8^+$	128.036	Aromatic
$C_{13}H_9^+$	165.035	Aromatic

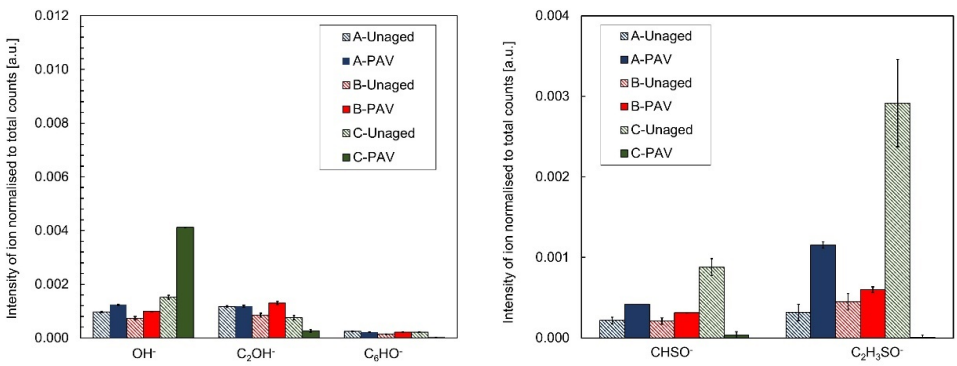

Figure 4-8 Intensity of $(OH)_x$-containing compounds [left] and SO_x-containing compounds [right] with lab ageing

Similar trends follow for the increase of the ion fragments with generic formula RSO_x given in Figure 4-8 [right]. The results of bitumen A and B support the formation of considerable amounts of sulfoxide-containing compounds after the sequential short and long-term ageing as the intensities of A-PAV and B-PAV remain higher than the unaged state. Caution should always be taken concerning the specific sulfoxide-containing fragments observed with TOF-SIMS which give a partial view of the total sulfoxides present in bitumen which FTIR might capture in a greater penetration depth; this means that limitations should be again acknowledged when comparing the

different techniques. Potentially, the results of the two surface techniques together could be used to exploit the surface effects of oxidation in bituminous films. Bitumen C seems to reduce the sulfoxide-containing ion fragments with ageing something which does not agree with the FTIR results. This may be explained by the segregation of wax, present in this bitumen, on the surface of the bituminous film, resulting in aliphatic compounds which cover most of the surface [30,167].

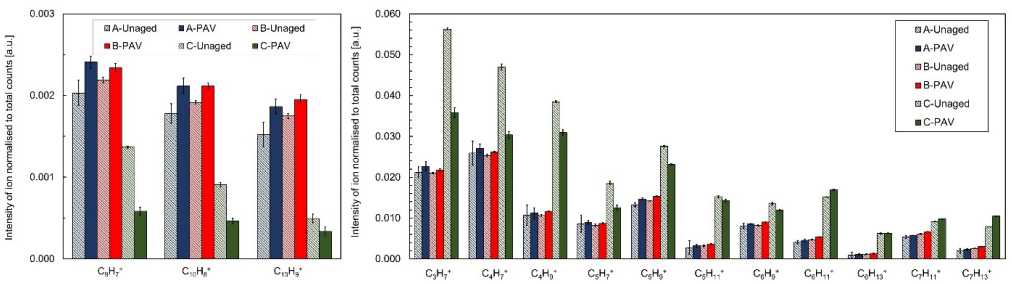

Figure 4-9 Intensity of PAH fragments [left] and aliphatic fragments [right] with lab ageing

The analysis of selected ions in the positive ion spectra (Figure 4-9 [left]) assigned to PAH is also discussed. The intensity of PAH of B-Unaged and A-Unaged increased slightly after PAV, whereas a significant drop of PAH with ageing for bitumen C was captured, probably due to the increase of the waxy particles on the surface upon ageing. Finally, binders A and B showed an almost constant behaviour (or a slight increase) of aliphatic ion fragments upon PAV contrary to bitumen C which showed a decrease for specific aliphatic ion fragments (Figure 4-9 [right]). The intensity of the aliphatics for bitumen C appeared the highest, a fact that can be explained by the wax present in this binder and the association of wax-related particles with aliphatics on the surface of this bitumen.

4.5 Oxidation products in SARA fractions

4.5.1 *FTIR*

The chemical fingerprinting of asphaltenes and maltenes of binders B and C that differ in terms of wax presence, as well as of their parent bitumen samples were investigated in FTIR. The effect of ageing on the bitumen was somewhat as expected. Increases were mainly seen in carbonyl and sulfoxide signals. As shown already in Figure 4-2 only bitumen B shows a carbonyl signal in the unaged state, related to the fact that this binder is produced from an acid crude oil or a crude with high acidity.

For asphaltenes, the IR spectra were different from the bitumen samples and maltenes (which displayed very similar spectra). The signals associated with the stretching or bending vibrations of saturated hydrocarbons at about 2920 cm^{-1}, 2850 cm^{-1}, 1460 cm^{-1} and 1376 cm^{-1} are much smaller compared to those for the binders.

Differences between the bitumen fractions and the effect of long-term lab ageing are further shown by normalised peak areas in Figure 4-10. Due to the considerable differences in the symmetric and asymmetric bending vibrations of the aliphatic groups at 1460 cm^{-1} and 1376 cm^{-1} for the different fractions, the normalised areas were preferred to be used for the fractions instead of the indices introduced in Chapter 2. For the area normalisation, the procedure described in [17] was adopted. For this procedure, first, all the spectra are shifted to zero absorbance at a fixed wavenumber of the lowest spectrum absorbance. Then an absorbance correction factor is applied to scale the spectra at the asymmetric stretching vibration of the aliphatic structures at 2923 cm^{-1}. The entire spectrum is then multiplied by this ratio factor.

For bitumen C, it is clear that in the unaged state, the asphaltenes do not contain carbonyls, which all fall into the maltene fraction (see Figure 4-10). After long-term lab ageing, the asphaltenes contain a large part of the carbonyl and sulfoxide signals, suggesting that a lot of molecules become insoluble in warm n-heptane after they have reacted with oxygen to form carbonyl and sulfoxide groups (Figure 4-10). This is the case for both binders B and C and can explain the increase of the more polar fractions in asphaltenes due to ageing. The observation is in agreement with that made by Mirwald and his group [92]. For the maltene fraction, on the other hand, the effect of ageing is rather small for bitumen B in comparison to bitumen C.

Besides those observations already made on carbonyls and sulfoxides, an obvious difference was found in the normalised aromaticity area, being ranked as asphaltenes > bitumen > maltenes, while this area was slightly decreased upon ageing in the maltenes.

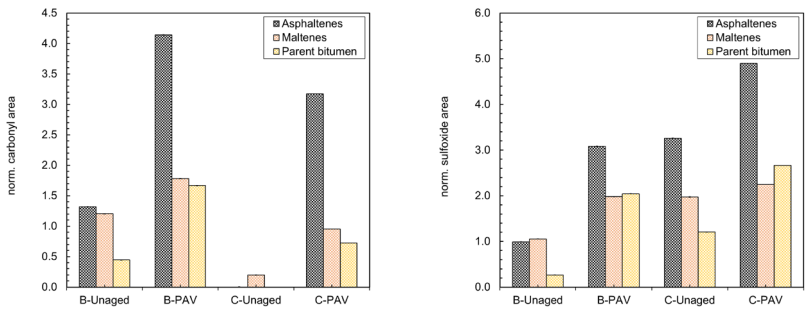

Figure 4-10 Normalised absorbance peak areas of carbonyls [left] and sulfoxides [right] before and after PAV for binders B and C

4.5.2 *^{1}H-NMR*

In Figure 4-11, the relative hydrogen percentage distributions of different types of protons (methyl, methylene, α-alkyl, olefinic, aromatic) are plotted as the average of the two replicates with their standard deviation. The percentage distributions are shown for the maltenes, whereas for the corresponding bitumen before and after long-term lab ageing, the results can be found previously in Figure 4-6. No results are shown for asphaltenes since this fraction was not completely dissolved in deuterated tetrachloroethane. Figure 4-11 indicates that the hydrogen percentage distributions of the two binders are quite different in the maltene fractions. The maltenes from bitumen B show a higher methyl region, lower α-alkyl region and lower aromatic region compared to the maltenes from bitumen C. The differences between the maltenes fractions can already be seen in the two bitumen samples (Figure 4-6), possibly indicating that the binders were produced from different crude sources and/or by different refining processes. The two graphs together also show that ageing affects in a similar manner the two maltene fractions and their parent binders, i.e. an increase is observed for methyl and methylene regions and a decrease seems to hold for aromatic and α-alkyl regions. In all the cases, the olefinic region is negligible. The changes upon ageing are more obvious for the maltene fraction of bitumen C as compared to that of bitumen B. This is also the case when the two bitumen samples were compared.

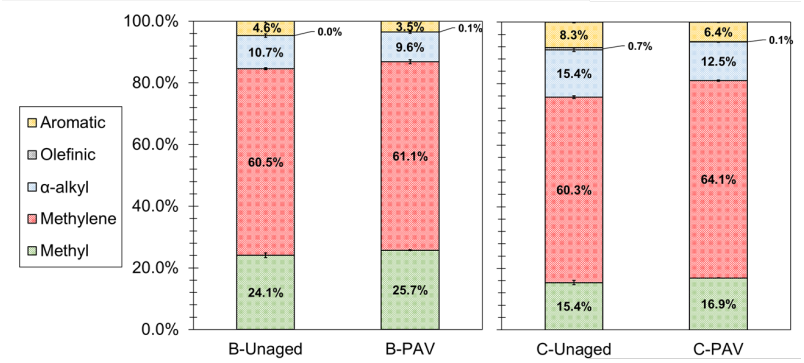

Figure 4-11 Relative percentage distribution of protons in maltenes of bitumen B and C before and after PAV

4.5.3 ***DSC***

The DSC thermograms of the parent bitumen C and its maltenes in the heating scan revealed an endothermic reaction, which is interpreted as melting of the wax in this bitumen. Thus, the melting enthalpy can be used as a measurement of the wax present in this sample. No results of the thermal properties are shown for asphaltenes since asphaltenes were not melted under the testing conditions. Bitumen C and its maltenes fraction displayed a similar melting starting temperature of slightly above -15 °C, but they differ in melting out temperatures, which was about 90 °C for the parent bitumen C and 80 °C for the maltenes. The wide range of temperatures during which the melting takes place points towards the presence of molecules with different melting points. The melting of a given molecule also depends on the surrounding chemical compositions, and this is the case when comparing the bitumen and the maltene fraction. On the other hand, the wax melting starting temperature and melting out temperature were not affected by ageing. For bitumen B, as well as its maltene fraction, no wax crystallisation and melting were detected by DSC but only a glass transition temperature. This supports that bitumen B is a wax-free bitumen.

Regarding the melting enthalpy in Figure 4-12 [left] the maltene fraction of bitumen C shows a higher value than the corresponding bitumen. Figure 4-12 [left] also shows that, after long-term ageing, the melting enthalpy of the bitumen becomes lower, while for the maltenes the effect of ageing is likely the opposite, i.e. higher melting enthalpy. These results suggest that for the investigated bitumen C, more wax is present in the maltenes when the bitumen is fractionated, especially after long-term ageing. Finally, the effect of glass transition temperature is clear between the maltenes and the parent binders B and C, namely the maltenes experience consistently a lower glass transition temperature both before and after long-term lab ageing for both

binders. Ageing seems to decrease the glass transition temperature for the maltenes of the two binders whereas the opposite trend is found for the parent binders (Figure 4-12 [right]).

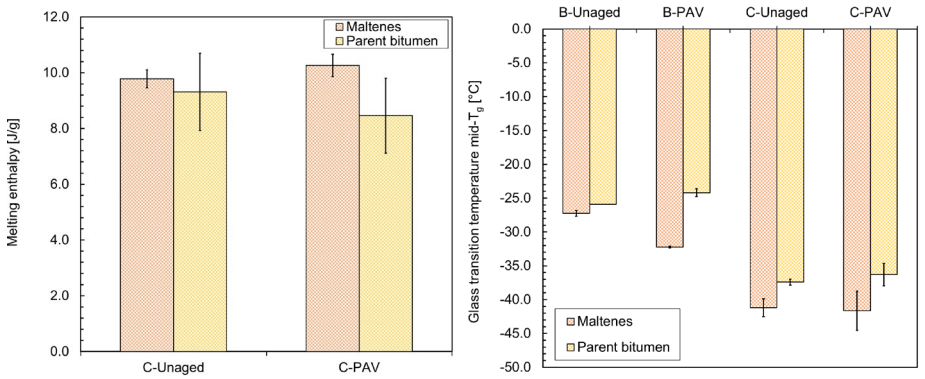

Figure 4-12 Melting enthalpies of parent bitumen C and its maltenes [left] and glass transition temperatures [right] of binders B and C and their maltenes with lab ageing

4.6 Highlights of the chapter

- FTIR supports the increase of the oxygenated indices of sulfoxide and carbonyl with lab ageing, for all binders, independently of bitumen source, distillation process and performance.
- Differences in the extent of carbonyl and sulfoxide formation are observed between the various binders, especially for those of different empirical performance, with long-term lab ageing.
- EPR analyses explore the role of the intermediate oxidation products, the organic carbon-centred radicals, which were increased for all binder types with short-term lab ageing.
- The EPR VO^{2+} centres remain relatively constant and are almost insusceptible to lab ageing.
- ^{1}H NMR demonstrates slight changes in the relative proton distribution upon lab ageing for all the studied binders.
- Sulfoxide-containing compounds via TOF-SIMS are increased significantly after the sequentially short-and long-term lab ageing for the straight-run binders.
- $(OH)_x$-containing fragments suggest that apart from carbonyls, other products, such as alcohols and carboxylic acids, can be produced with lab ageing regardless of the bitumen type.

- After lab ageing of bitumen, a large part of the carbonyl and sulfoxide signals can be found in the asphaltene fraction.
- ^{1}H-NMR relative proton distribution changes with lab ageing in a similar manner both for maltenes and the parent bitumen.
- FTIR indicates that asphaltenes are the most aromatic fraction followed by the parent bitumen and maltenes.
- After bitumen fractionation, more wax is found in the maltenes fraction compared to the parent bitumen, and this is even more evident when the bitumen is lab aged.

The ageing mechanisms of bitumen with standardised lab simulations were explored in this Chapter. A comparison between the oxidation products of routine lab ageing simulations and the ones found via kinetics is of certain value to be performed in order to understand more clearly the intensity of the chemical changes that take place in bitumen. This will be partially covered in Chapter 7 of the current dissertation.

5

MECHANISMS OF SURFACE MICROSTRUCTURE IN BITUMEN

5.1 **Summary**[*]

It is well documented that most bituminous binders contain crystallisable material and all of them consist of asphaltenes. The crystallisable fraction, often referred to as paraffinic or natural wax, is associated with the bitumen's origin and has an influence on its rheological performance and microstructure. Before diving into a systematic investigation of the ageing effect on bitumen's microstructure, an improved understanding of the underlying mechanisms is of paramount importance. In general, there are two main theories with regard to the appearance of bitumen's surface microstructure, namely due to asphaltenes and because of wax in bitumen. Chapter 5 adopts the second theory and explores the potential crystallisation and melting process of a waxy and a wax-free bitumen via three different approaches: DSC, WAXD and CLSM. The findings of this Chapter reveal that the DSC transitions of the waxy bitumen are in good agreement with the corresponding occurrence of WAXD signals and to some extent with the formation and disappearance of the surface microstructures which were followed in real-time at two cooling and heating rates. WAXD results additionally demonstrate that the crystalline material in bitumen is organised in an orthorhombic unit cell, typical for straight-chain aliphatic structures. On the other hand, DSC and WAXD support the lack of crystallinity for the wax-free bitumen which is a hypothesis that could explain its featureless CLSM surface. Overall, the originality of this Chapter resides in the disclosure of connections between

[*]*This chapter is redrafted from: G. Pipintakos et al., Crystallinity of bitumen via WAXD and DSC and its effect on the surface microstructure, Crystals (2022). https://doi.org/10.3390/cryst12060755*

crystallographic properties and thermal transitions and examines a certain hypothesis of the possible mechanisms behind the surface micromorphology of bitumen.

5.2 **Objectives**

The aim of Chapter 5 is first to compare the thermal transitions observed in DSC, associated with the melting and crystallisation behaviour of natural waxes in bitumen, to the crystallographic findings via WAXD, during cooling and heating in the same temperature range. This was based on the hypothesis that wax crystallinity is one of the possible reasons in the literature for the formation of various morphological structures on a bitumen surface, with the other one being the link of asphaltenes with the microstructure [102]. Following the first hypothesis, two bituminous binders, a waxy binder A and a wax-free binder B, were used in this Chapter. The effect of annealing at room temperature was also investigated in DSC and CLSM for the waxy bitumen. Overall, this Chapter manages to provide an explanation for a certain hypothesis about the mechanisms governing the formation of certain microstructural patterns in bitumen, known as bee structures. As mentioned in Chapter 1, if a relationship between these microstructures with the wax presence holds, will be of paramount importance to be better understood for the prevention of a number of implications in the performance of bitumen (i.e. increased low-temperature cracking) and its production (i.e. deposition problems). A schematic overview of the research methodology adopted in this Chapter 5 together with the main goals of it is provided for the ease of the reader in Figure 5-1.

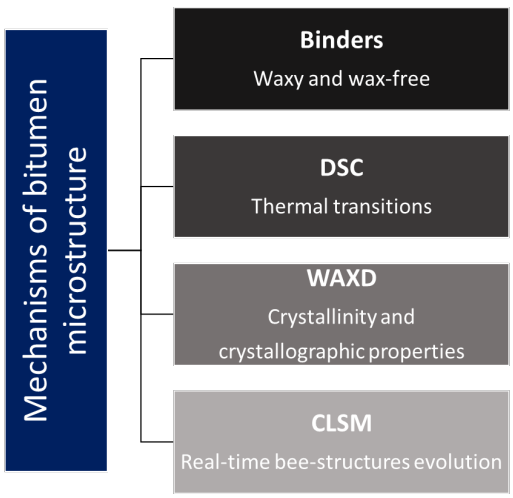

Figure 5-1 Flowchart of the experimental part of Chapter 5 and objectives

5.3 **Materials and methods**

Based on the preliminary DSC wax determination proposed in Chapter 4, in this Chapter a waxy bitumen A and a wax-free bitumen B were selected with the potential to observe differences in crystallinity and surface morphology. Their empirical properties are summarised in

Table 5-1. In this work, the selected softer bitumen A was the residue of a visbreaking conversion process during which additional wax may have been formed, while bitumen B is a harder straight-run bitumen, originating from a different crude, containing no wax.

Table 5-1 Basic properties of the waxy and wax-free bitumen

Material	Property	Binder		Test Method
Bitumen		A	B	
	Penetration 25 °C (0.1 mm)	80	16	EN1426
	Softening point (°C)	45.8	61.1	EN1427
	Penetration index, Ip	-1.20	-1.06	EN12591

The two binders, A and B, were further tested in DSC cooling/heating cycles and after annealing as well as at ambient temperature and cooling/heating cycles in WAXD. To follow the microstructure evolution on CLSM, an in-house thermal fixture was assembled by the Road Engineering Research Section (Figure 5-2), consisting of electrical variable resistors that were fixed accordingly to obtain the required temperature on top of a metallic plate. The temperature of this small heating element was adjusted based on calibrated thermocouples inserted in the bituminous sample on the glass plate. Investigations on the waxy bitumen's microstructure were conducted in cooling and heating cycles, in a range of temperatures between 10 to 80 °C at a cooling/heating cycle of 1.25 °C/min and a lower cooling/heating cycle using 0.5 °C/min rate. Preliminary investigations showed featureless surfaces for temperatures above 65 °C in both cycles as well as for the wax-free bitumen B which was not investigated further. Additionally, the effect of annealing at room temperature was also investigated for the waxy bitumen after 24 hours in a heating scan.

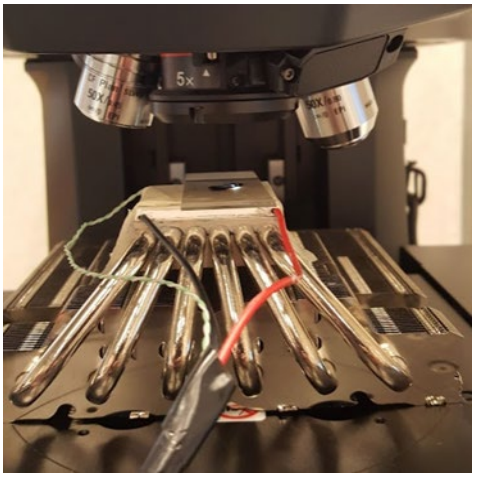

Figure 5-2 Bituminous sample placed on the in-house heating element under CLSM

Differential Interference Contrast (DIC) CLSM images with a laser and white light source on the surface of the bituminous samples were recorded during real-time microstructure evolution. A DIC CLSM image has the advantage of introducing moderated contrast to optical images, producing a pseudo-3D effect. To additionally assess the evolution of the bee structures a meaningful, scale-free metric was used, namely the bee area percentage (bee coverage). The image post-processing is based on a 90-95% height or depth threshold, using the height differences between the valleys and peaks of the bee structures and the rest of the bituminous surface [174]. More specifically, masks of the bee structures are created based on these height thresholds both for valleys and peaks and division with the total image area allows the determination of the bee area coverage.

5.4 Mechanisms of bitumen microstructure

5.4.1 *DSC*

DSC scans obtained during cooling/heating for both binders and heating after 24 hours annealing temperature at 25 °C for bitumen A are shown in Figure 5-3. The cooling scan of bitumen A shows an exothermic transition with a maximum at around +30 °C, which is attributed to the wax crystallisation. This transition is indicated by the area A in Figure 5-3 [top]. It continues down to the glass transition which appears for bitumen A at around -30 °C. The cooling scan of the wax-free bitumen B confirms the absence of crystallisable components as no exothermic transition can be observed whereas the glass transition temperature for this bitumen can be found around -15 °C.

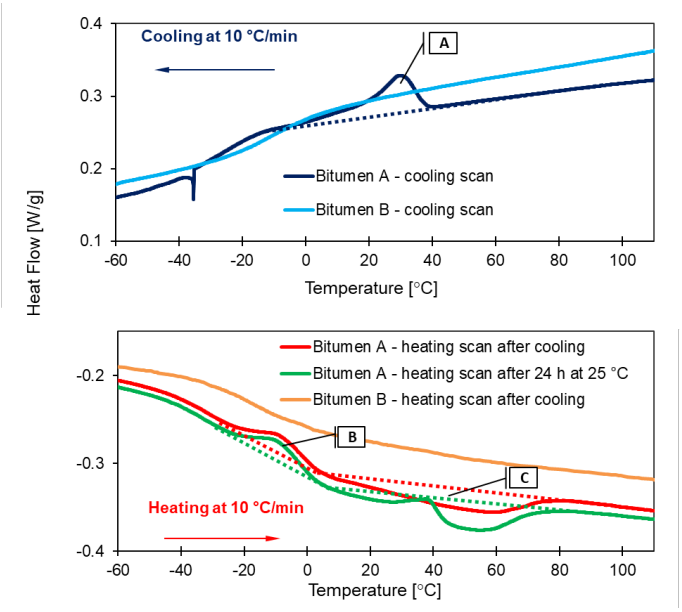

Figure 5-3 DSC cooling scan [top], DSC heating scan for bitumen A and B and heating after annealing at 25 °C for 24 hours for bitumen A [bottom]

In the subsequent heating ramp of the waxy bitumen A, denoted as 'heating scan after cooling', an endothermic transition can be clearly observed (area C), which is related to wax melting. The melting end temperature is much higher than the corresponding crystallisation onset temperature for this bitumen indicating the need of nucleation at a certain degree of undercooling. The heating scan of bitumen A also reveals a small exothermic signal close to the glass transition, which is associated with a cold crystallisation in the literature [175,176], denoted as area B in Figure 5-3 [bottom]. Both heating and cooling scans of bitumen A show wide temperature ranges for crystallisation and melting, potentially indicating large differences between the crystals' sizes and perfection. Changing wax concentrations in the liquid while the crystallisation is progressing, may also have contributed to the width of the transition. Indeed, as the crystallinity progresses upon cooling, the remaining melt becomes wax depleted by which lower temperatures are needed to induce further crystallisation [177]. This effect, which is common for crystallisation from mixed melts is mirrored for melting upon heating. On the other hand, bitumen B appears to have no apparent transition phenomena which occur during the heating scan.

Further, the melting scan recorded after the annealing for bitumen A presents a different shape as illustrated by the green curve in Figure 5-3 [bottom]. In this case, the melting signal consists of two peak temperatures, with the annealing temperature being located between these two peak temperatures of melting, indicating that during

the annealing period, recrystallisation takes place forming crystals with a higher melting temperature.

In Table 5-2, the onset and peak crystallisation temperatures (Tc), the peak and end melting temperatures (Tm) and the crystallisation and melting enthalpies (ΔH) are presented. The main difference between the crystallisation and melting enthalpy is mainly due to the additional cold crystallisation during the heating scan. The undercooling effects are again obvious since Tm-end is much higher than the Tc-onset. Furthermore, the melting temperature range of bitumen A before and after annealing slightly differs in accordance with the results of a Round Robin study where the same bitumen was used [74]. This past study also presented the repeatability and reproducibility between the different laboratories before and after annealing and the melting, crystallisation onset and peak of the current study lie adequately well within the previously reported range. In the current study of Chapter 5 changes in the shape of the melting after the second heating were additionally observed, while the annealing procedure does not influence significantly the melting enthalpy. This witnesses the small effects of annealing on the overall transition phenomena.

Table 5-2 Summary of DSC thermal transition data of binders A and B

Material	Cooling cycle			Heating cycle		
Bitumen	Tc-onset [°C]	Tc-peak [°C]	ΔH [J/g]	Tm-end [°C]	Tm-peak [°C]	ΔH [J/g]
A	42.0	29.4	4.5	84.0	54.0	7.2
A after annealing	N/D	N/D	N/D	91.0	52.6	6.7
B	N/A	N/A	N/A	N/A	N/A	N/A

N/D=Not determined, N/A=Not applicable

5.4.2 *WAXD*

Initially, a WAXD investigation for both bituminous binders was performed at room temperature. As can be seen in Figure 5-4 in contrast to bitumen B only bitumen A contains two sharp crystalline reflections in the WAXD patterns which are due to orthorhombically organised paraffins as described by Bunn and of which the labelled 110 and 200 reflections are most prominent [178]. The data are shifted along the intensity axis to avoid overlap and reflections are labelled with their Miller indices. This observation is in line with the absence of crystallinity expected from the wax-free crude and initially confirmed with DSC.

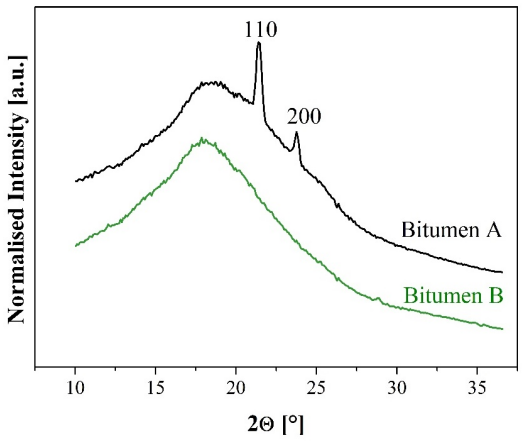

Figure 5-4 Normalised synchrotron WAXD patterns of bitumen A and B at room temperature (25 °C)

In a second experiment, WAXD patterns for bitumen A, which showed crystalline reflections at room temperature, were recorded during cooling and heating. A representation of the temperature-dependent WAXD patterns during the cooling scan is shown in Figure 5-5, in which the scattered intensities are presented by means of a grey scale. Darker regions correspond to lower scattering intensities while the 110 and 200 reflections are labelled accordingly. It appears that the orthorhombic 110 and 200 reflections are present between roughly +35 and -40 °C and increase upon cooling.

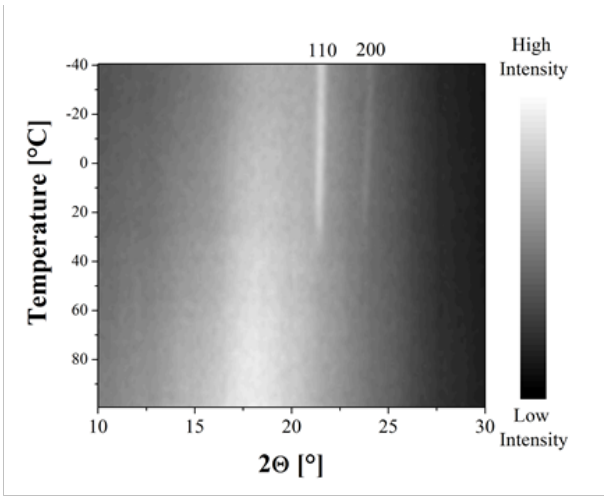

Figure 5-5 Time-temperature resolved synchrotron WAXD patterns during cooling at 10 °C/min from 100 to -40 °C for bitumen A

From the integral of the 110 and 200 reflections, a crystallinity index can be obtained as described in Chapter 2. The index was arbitrarily normalised to its value at -40 °C during the heating run. In Figure 5-6 this crystallinity index is plotted during the cooling (black data) and heating (red data) scans. For better visualisation of the crystallinity

evolution within bitumen A, a smooth sigmoidal fitting curve was added. At low temperatures, both the cooling and heating scans show a plateau of the crystallinity up to 10 and 30 °C respectively, followed by a steep decrease in intermediate temperatures. At high temperatures, the wax within bitumen A is fully molten and the crystallinity equals zero. The end melting temperature is around 70 °C for the heating scan which is in agreement with the DSC reported temperature. Similar to DSC, undercooling effects are observed by WAXD and the onset of crystallinity at around 50 °C corresponds very well to the DSC temperatures. The starting value of the crystallinity in the heating run also seems to be slightly higher than the end value of the cooling run, indicating that additional crystallinity was generated during the short isothermal stay at -40 °C.

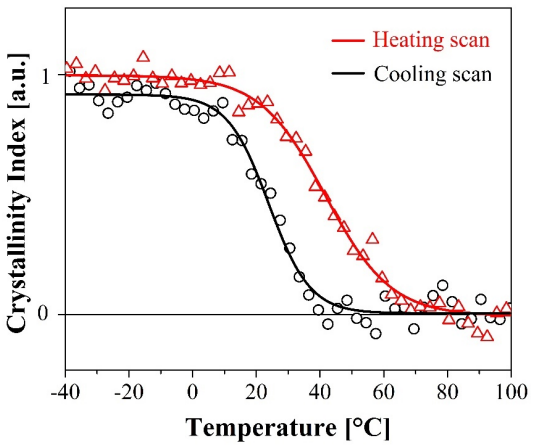

Figure 5-6 Evolution of synchrotron WAXD-based crystallinity index of bitumen A during cooling and heating, where dots are experimental data points and full lines are sigmoidal guides

5.5 Evolution of bitumen microstructure

5.5.1 *CLSM*

With CLSM the percentage of the bee structures (% of their total area) for bitumen A is given in Figure 5-7, within the temperature range between +10 to +80 °C, during cooling and heating at two different rates. Only the microstructure evolution of bitumen A was investigated, as the non-waxy bitumen B showed no microstructural characteristics in accordance with other studies [72,174].

The analysis of the CLSM images shows that during the faster cooling/heating rate the bees start to form at +50 °C and their percentage increases quickly when cooling further between +50 and +30 °C. In the subsequent heating cycle, the bee percentage

decreases in a slightly larger temperature range, between +30 and +60 °C. For the cooling and subsequent heating cycle recorded at a slower rate, the effects are very similar but the temperatures are shifted to higher values. This indicates that during a slow cooling, there is more time to form larger and more perfect crystals which in the corresponding heating cycle have a higher melting temperature. In addition, in the slower heating and cooling scan the bee percentage seems to develop in two steps, a steep change between 0 and 2% and then a less steep change up to 2.7% bee area Some possible reasons for this observation could be related to the parallel viscosity increase/decrease in the binder upon cooling/heating which at a certain point may start to hinder the crystallinity formation or the phase separation of the melt in paraffin rich and paraffin poor phases before crystallisation.

In general, the observations support that the appearance/disappearance of WAXD patterns, coincide well with the observed changes in the bee structures and with the thermal observations in DSC. Especially, if one considers that the experimental conditions are not exactly the same, as cooling rates are much slower in CLSM compared to DSC and WAXD and that microscopy is following a surface feature while DSC and WAXD are measuring bulk properties.

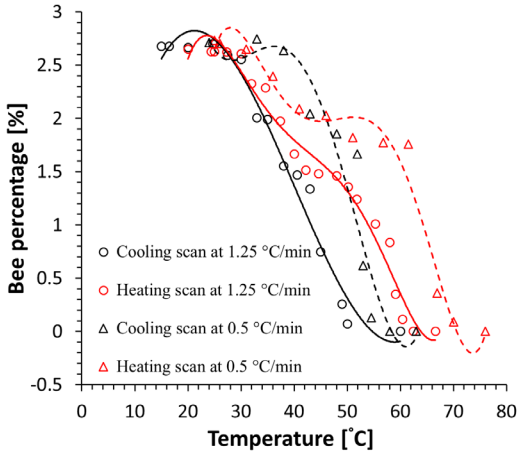

Figure 5-7 Evolution of CLSM bee structures during heating and cooling scans, where markers are experimental data points whereas full and dash lines are polynomial guides

In Figure 5-8 and Figure 5-9, selected temperatures of the cooling respectively heating scan for bitumen A (rate 1.25 °C/min) are represented. It can be seen in Figure 5-8 that progressively the bee structures are formed during cooling. The bee structures appear at temperatures below 50 °C and they can be clearly seen at 45 °C. Similarly, as shown in Figure 5-9, the bee structures disappear from the surface at temperatures greater than 60 °C during heating, in line with the end melting temperature of DSC. Apart from the bee structure formation upon cooling, it was noticed that the surface becomes

coarser upon further cooling, whereas any potential vertical-like artefacts are due to small sample movements during cooling/heating.

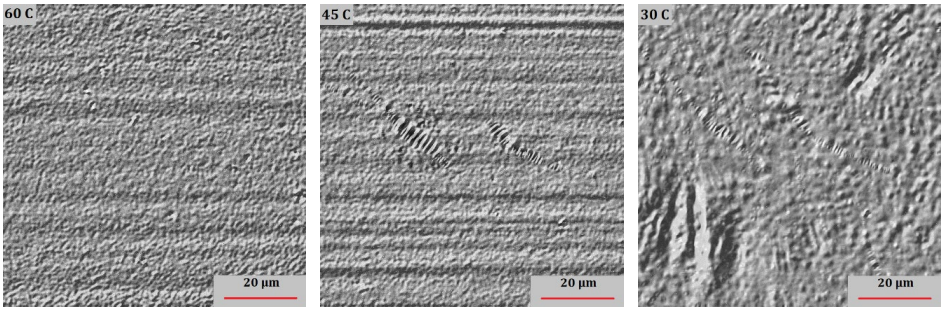

Figure 5-8 CLSM-DIC images of bitumen A at selected temperatures during the fast cooling scan (1.25 °C/min)

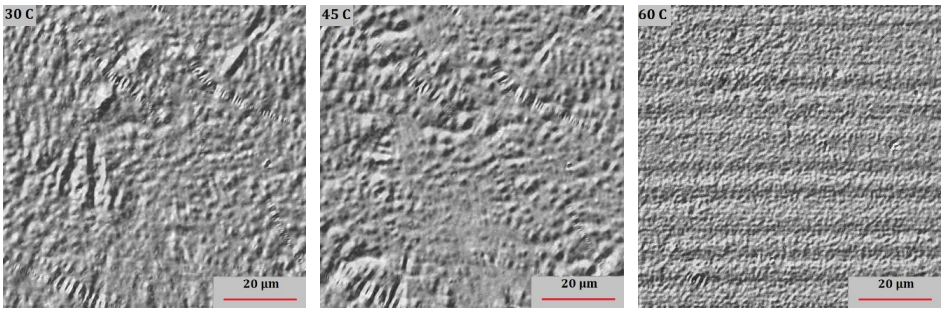

Figure 5-9 CLSM-DIC images of bitumen A at selected temperatures during the fast heating scan (1.25 °C/min)

For the sample that was annealed 24 hours at room temperature (Figure 5-10), this was prepared by placing a drop of binder on a hot plate (120 °C) and cooling it almost immediately to room temperature. When heating this binder at 1.25 °C/min, it was noted that in this case, the bees disappeared already at 55 °C, so even faster as observed in the case of Figure 5-8 and Figure 5-9, where a sample was first cooled and subsequently heated at 1.25 °C/min rate. Hence, it seems that the cooling rate before recording the heating scan, rather than an isothermal annealing, determines at what temperature the bees disappear in the subsequent heating scan.

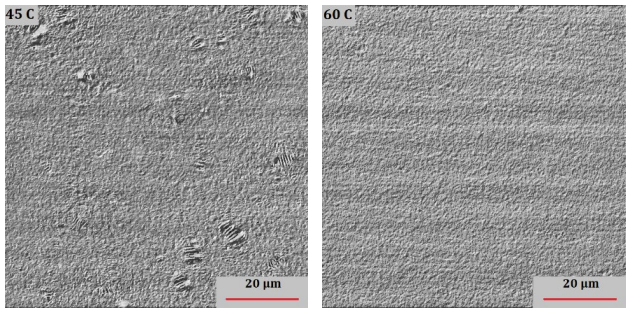

Figure 5-10 CLSM-DIC images of bitumen A at selected temperatures during the heating scan (1.25 °C/min) after 24 hours annealing at 25 °C

5.6 **Highlights of the chapter**

- DSC and WAXD relate thermal transitions to changes in the X-ray diffraction pattern.
- The correspondence between the DSC, WAXD and CLSM and the temperature ranges, where patterns are formed and disappear, confirm that wax crystallinity is the reason for the endo- and exothermic transitions and support, based on a wax hypothesis, the bee structure formation in bitumen.
- The wax-free bitumen displayed a glass transition and no other thermal effects or surface structure.
- Annealing affects the shape of the broad DSC endotherm of the waxy bitumen with a negligible effect on the melting enthalpy.
- The WAXD results at room temperature showed crystalline diffractions for the waxy binder.
- The diffraction pattern by WAXD showed that the crystalline material in the waxy bitumen has an orthorhombic unit cell.
- Heating and cooling scans revealed that the WAXD pattern for the waxy bitumen disappeared at around 70 °C (in heating) and was formed at around 50 °C (in cooling).
- The CLSM indicates that on the surface of the waxy binder bee structures are formed, upon cooling, which disappear upon heating.
- The cooling/heating rate has an influence on the temperatures where bee structures are formed or disappear.

6

EFFECT OF LAB AGEING ON BITUMEN MICROSTRUCTURE

6.1 **Summary**[*]

Some theories postulate the effect of crystalline wax on the so-called bee structures of bitumen's microstructure while others support that asphaltenes is the governing reason for such structures in bitumen. Although it is widely accepted that ageing has an effect on this unique microstructure yet conflicting literature exists on clear trends. Chapter 6 explores the effect of lab ageing on the bee structures of bitumen, employing two advanced microscopic techniques: an AFM and a CLSM. Having supported to some extent a certain hypothesis about the mechanisms that govern the bitumen microstructure in a previous Chapter, here four waxy and two wax-free bituminous binders are investigated before and after sequential laboratory short- and long-term ageing. Chapter 6 demonstrates that the number of bees per μm^2 and the bee area coverage decrease with ageing, whereas their size is increasing, contributing to the hypothesis that ageing has a clear effect on the microstructure. A systematic analysis of the waveform characteristics is also provided for the peaks and valleys as well as the shape probabilistic values of the bee structures. In conclusion, the results of the two techniques are in good agreement, reporting similar trends upon ageing for the bee coverage. Differences are mainly identified in the waveform calculations. Additionally, the efforts undertaken to capture bitumen's microstructure via deep learning and advanced image processing techniques are conceptually explained. The systematic investigation in this work (commercial image processing or sophisticated machine learning) assists in enhancing the understanding of the effect of ageing on the surface microstructure.

[*]*This chapter is redrafted from: G. Pipintakos et al., Coupling AFM and CLSM to investigate the effect of ageing on the bee structures of bitumen, Micron (2021). https://doi.org/10.1016/j.micron.2021.103149*

6.2 **Objectives**

Although considerable research has been devoted to the identification of the bee-like structures and their accompanying phases there is no consensus on how these are affected by ageing. Typically, 3 to 4 phases can be identified in bitumen's surface with AFM imaging: the catanaphase (bee structure), the periphase (around catanaphase), and the perpetua phase which can be distinguished in the paraphase (solvent regions) and the salphase (high phase contrast spots) [74,179]. A simplified example of this phase detection is given in the example Figure 6-1 before and after ageing.

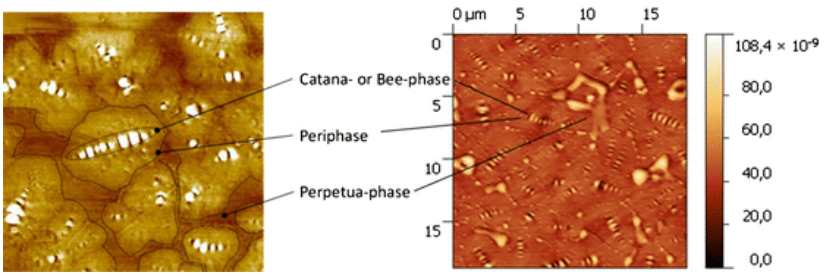

Figure 6-1 Typical phases of surface bitumen microstructure before [left] and after ageing [right] in AFM phase contrast and topography respectively (reprinted by permission from [74]*)*

Yet controversy exists whether prolonged and more severe ageing increases [124,180–184], decreases [185,186] or fluctuates [90,126,187] i.e. the length and area of the bee structures. On the other hand, a number of studies [124,126,183–185,188–191] found consistent changes with ageing on the surface stiffness, adhesive and cohesive strength and force, with most of them claiming an increase of these properties. Consequently, no clear view exists about the wavelength, height and roughness of the sequence of peaks and valleys of the catanaphase of the bee structures as well as the bee area percentage and length in bitumen upon ageing.

Acknowledging this gap in the literature, Chapter 6 aims to systematically examine the change of the most apparent bitumen surface microstructure, widely known as bee structures, upon ageing. Based on the hypothesis that wax crystallinity may be the reason for such structures, it examines four bituminous binders containing natural wax with respect to their bee characteristics of the catanaphase and two control wax-free binders before and after long-term laboratory ageing by utilising AFM and CLSM. This analysis adds a clearer view to the existing literature and attempts to establish links between the observations of the two microscopic techniques and their convergence. The experimental flowchart together with the objectives of Chapter 6 is given in Figure 6-2.

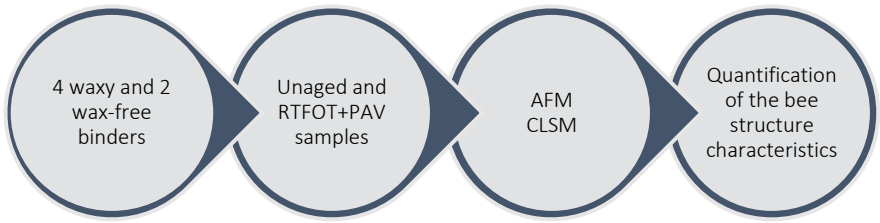

Figure 6-2 Flowchart of the experimental part of Chapter 6 and objectives

6.3 **Materials and Methods**

The bituminous binders of this Chapter were selected to contain surface bee structures, based on the partial support provided for the wax hypothesis about the mechanisms of bitumen's microstructure in Chapter 5. Preliminary microscopic investigations on several wax-free binders confirmed that such binders display featureless surface topography before as well as after ageing, independent of the bitumen type.

Thus, four waxy binders designated with letters A to D, having similar empirical properties were chosen as well as two wax-free control binders E and F, of different penetration classes. For consistency, the images of only one of the two wax-free binders are presented hereafter.

The waxy binders differ in the refinery process, more specifically, bitumen B, C and D are derived after a mild form of thermal cracking, namely visbreaking. Bitumen C was further treated in an air-blowing unit at elevated temperatures, a process that results in an increase in stiffness and softening point making the product more suitable for road applications. For bitumen A, the exact production details were not available. All four waxy binders contained natural wax (crystallisable compounds) which was confirmed by the melting enthalpies derived from DSC heating scans. Wax-free binders, like binders E and F, do not show endo- or exothermic transitions. Basic empirical properties and DSC melting enthalpies of all the binders are given in Table 6-1.

Routine laboratory ageing simulations were performed for all the binders according to the European standards for short- and long-term ageing [40,41] simulated with RTFOT followed by PAV for 20 hours. For all the subsequent microscopic observations the bitumen in the unaged state was designated as 'X unaged' and as 'X aged' after the

sequence of RTFOT and PAV, where X refers to the letter representing one of the binders.

Table 6-1 Empirical and DSC properties of the bituminous binders in the unaged state

Property	Bitumen						Test Method
	A	B	C	D	E	F	
Penetration 25 °C (0.1 mm)	42	52	52	67	187	64	EN1426
Softening point (°C)	51.3	49.0	49.8	46.8	38.5	47.7	EN1427
Penetration index, Ip	-1.27	-1.37	-1.17	-1.36	-1.80	-1.23	EN12591
Melting enthalpy (J/g)	2.8	6.8	6.2	7.6	0.0	0.0	[107]

Next, images were captured in the two ageing states for all the examined binders with AFM and CLSM. After sample preparation, as described in Chapter 2, scans are performed in air at 25 °C after a storage time of 24 hours, to allow the microstructures to develop and stabilise [73].

For the AFM image processing, a flat baseline plane was first obtained for the images. Then the contour scale was fixed according to the height of each topographical image to stress the height differences. For the identification of the bee structure, different masks were applied for the peaks and valleys of the topographical image, by imposing specific boundaries for the height and slope. Consequently, the total bee microstructure area was assessed. Bee profiles, wave properties and statistics were additionally evaluated before and after ageing. An example of the bee detection for bitumen A original is shown in Figure 6-3. The two colours represent the peaks and valleys while the overlapping is excluded by implying the height threshold above or below the reference plane where no bees occur. For the CLSM image processing, first, the same procedure described in Chapter 5 was followed for the bee characteristics of the topographical CLSM images, whereas additionally a deep learning-based object-detection model that can detect the bee patterns in the DIC CLSM images was proposed.

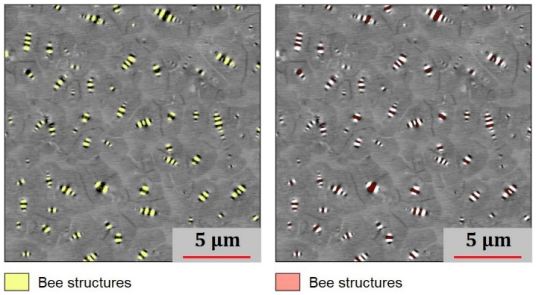

Figure 6-3 Example of the masks applied in AFM topography for peaks [left] and valleys [right] in bitumen A unaged

6.4 **Morphology and bee coverage**

AFM images of topography, phase contrast and 3D views are presented before and after ageing in Figure 6-4. The corresponding topography and 3D views are given for CSLM in Figure 6-5. As expected, the reference wax-free binder E is featureless before and after long-term lab ageing as witnessed both by AFM and CLSM topography images and can be seen in Figure 6-6. The same featureless bitumen surface displayed also the wax-free binder F. Furthermore, a visual inspection of the AFM phase images for bitumen A and D shows that they present two distinguished phases namely the so-called catanaphase, which is the bee structures, and the periphase surrounding the bee structures. These phases are becoming more pronounced upon ageing. For bitumen A the periphase forms an elliptical shape before and after ageing, while for bitumen D a star shape can be seen before ageing transforming into a spherulite phase after ageing. The elongated bee structures of bitumen C are also striking for the catanaphase of bitumen C before ageing, turning into a spherulite phase after ageing.

A-unaged

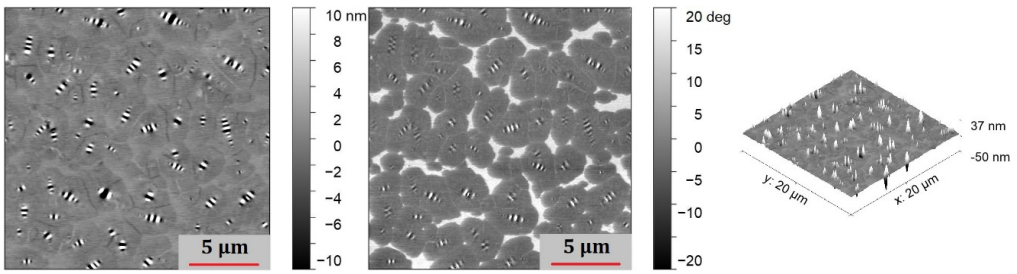

A-aged

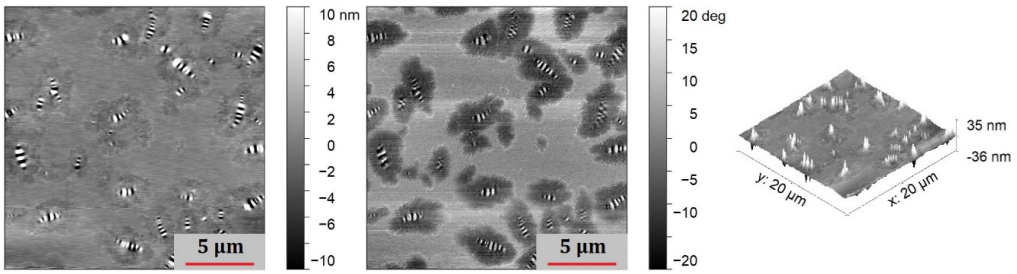

B-unaged

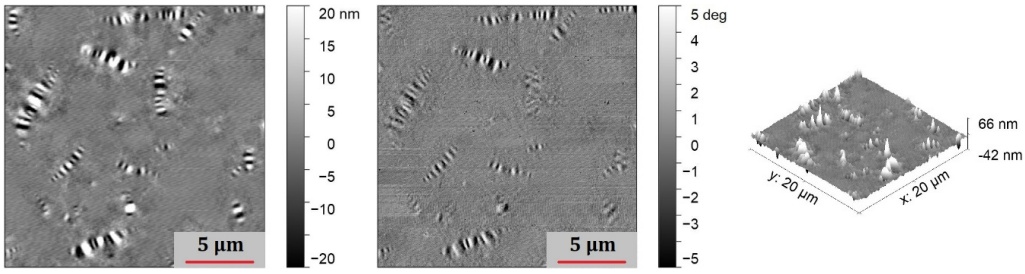

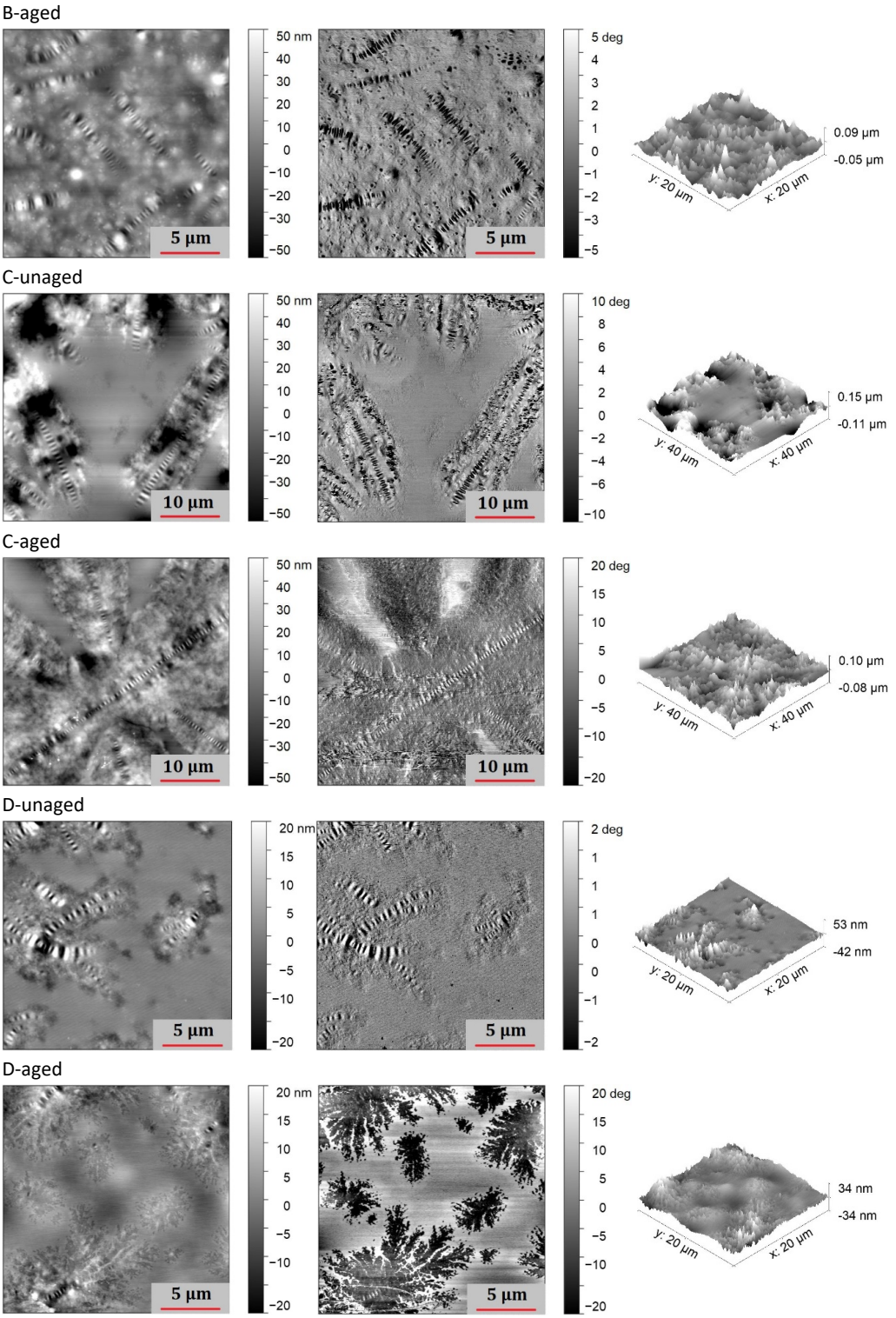

Figure 6-4 AFM topography [left], phase contrast [middle] and 3D view [right] images of waxy binders before and after long-term lab ageing

On the other hand, CLSM is not able to detect the surrounding environment of the bee structures, although the apparent catanaphase is observable. The height of the valleys and peaks of the catanaphase seems to be higher for bitumen B and C as can be revealed by the height extrema of the 3D views in AFM and CLSM. A detailed analysis of the wave characteristics of the bee structures is provided in the following section of this Chapter.

A-unaged

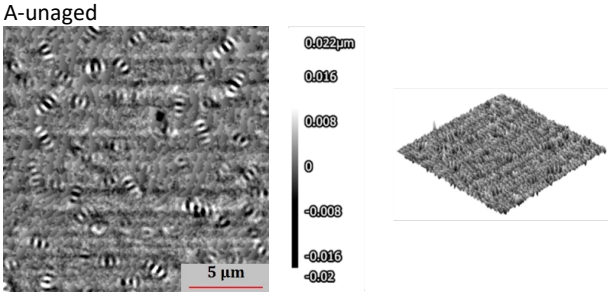

A-aged

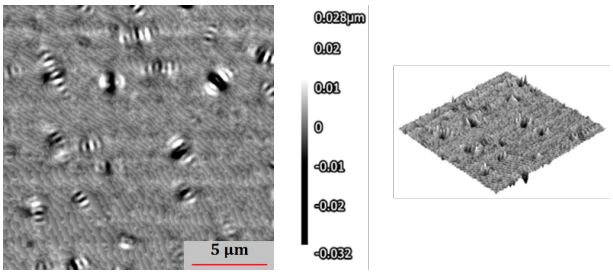

B-unaged

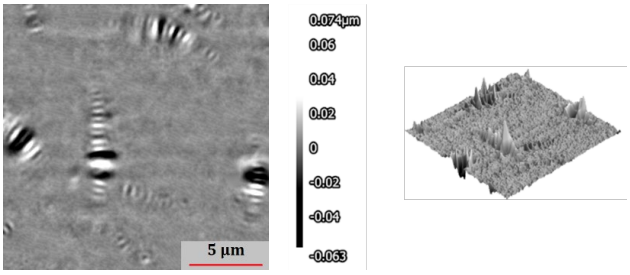

B-aged

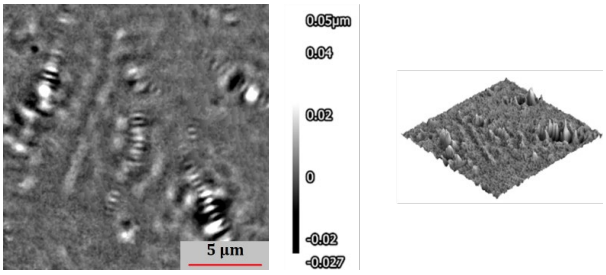

C-unaged

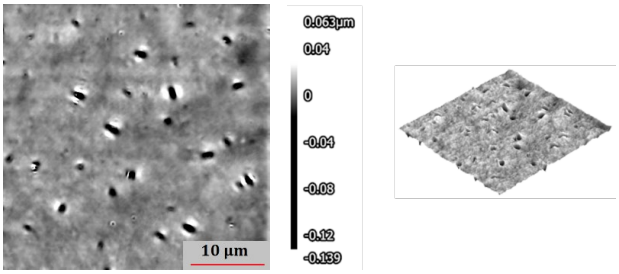

C-aged

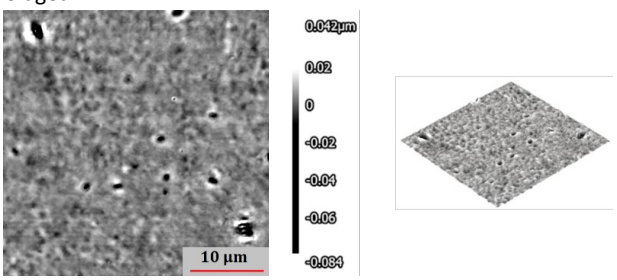

D-unaged

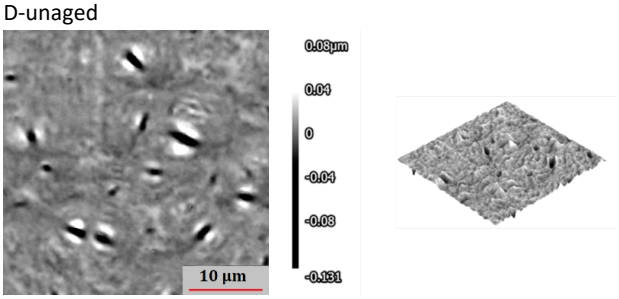

D-aged

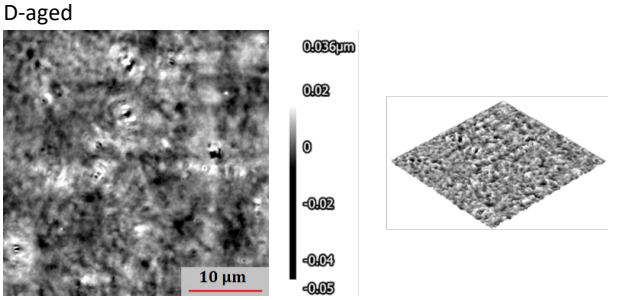

Figure 6-5 Topography [left] and 3D view [right] CLSM images of waxy binders before and after long-term lab ageing

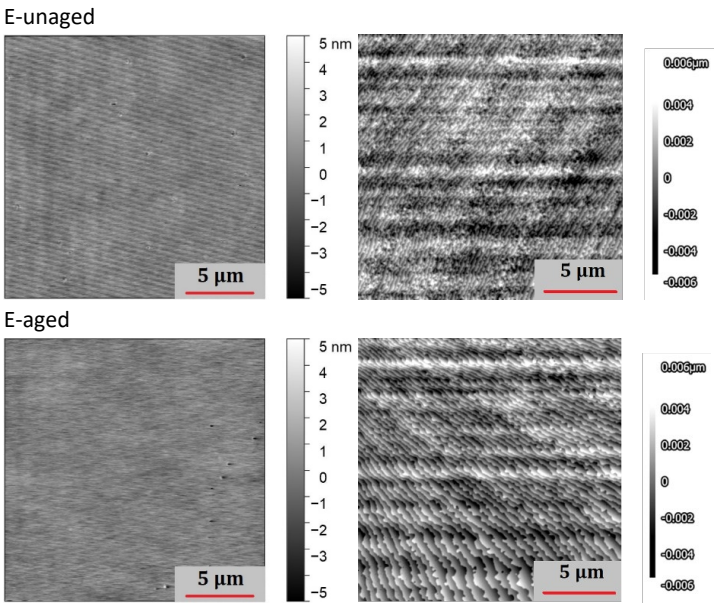

Figure 6-6 Topography of wax-free binder E before [up] and after long-term lab ageing [down] for AFM [left] and CLSM images [right]

When it comes to the effect of ageing, it can be easily observed from Figure 6-4 and Figure 6-5 that for bitumen A, B and D long-term lab ageing results in a decrease in the number of independent bees per µm^2 and an increase in their size in line with limited observations in literature [184]. To clarify these visual observations the processing of the masks, applied with commercial image processing software packages, for the catanaphase is discussed further. In Table 6-2, the relative bee density is expressed via the total bee area percentage (bee coverage) and the number of identified bees per µm^2. Table 6-2 indicates that the number of bees per µm^2, as well as their bee coverage, are reduced for all the waxy binders after long-term lab ageing. The data additionally support that ageing has the same decreasing trends on certain characteristics of the bee structures, independently of the bitumen type.

Based on the results of the previous Chapter 5, the change of the bee properties can be interpreted as additional crystallisation of the present wax due to ageing and additional investigation into the changes of melting enthalpy upon ageing needs to be performed to confirm it. For the unaged state, it seems that the wax content as expressed indirectly via the melting enthalpy in Table 6-1 has a weak link with the total bee area. Moreover, the compatibility of the aged bitumen matrix and the wax should be investigated i.e. by doped wax content into aged wax-free binders to obtain a clear view of the reason for the changes in the bitumen microstructure.

Table 6-2 Bee coverage and number of bee structures per µm² before and after lab ageing

Bitumen	Bee coverage (%)				Number of bees/µm²			
	Unaged		Aged		Unaged		Aged	
	AFM	CLSM	AFM	CLSM	AFM	CLSM	AFM	CLSM
A	3.85	3.43	1.97	2.83	0.084	0.147	0.052	0.067
B	4.08	4.01	3.46	3.03	0.023	0.045	0.014	0.028
C	3.17	3.29	2.71	2.75	0.006	0.005	0.004	0.003
D	3.12	2.75	0.96	1.13	0.004	0.023	0.003	0.005

The average size of bee structures was calculated from the bee coverage and the number of bees per µm², which is shown in Figure 6-7 [top]. The results of Figure 6-7 [top] demonstrate that for all the waxy binders the average size of the bee structures is increasing upon lab ageing as expected from an initial visual inspection, with the exception of bitumen D via CLSM. Overall, the average bee size varies between 0.5 and 8 µm² and a larger size seems to be associated with a higher melting enthalpy and wax content. For the latter care should be taken for the existing differences in thermal history between DSC and image acquisition. It is also apparent from the linear correlations in Figure 6-7 [bottom] that the two microscopic techniques, AFM and CLSM, are showing similar information.

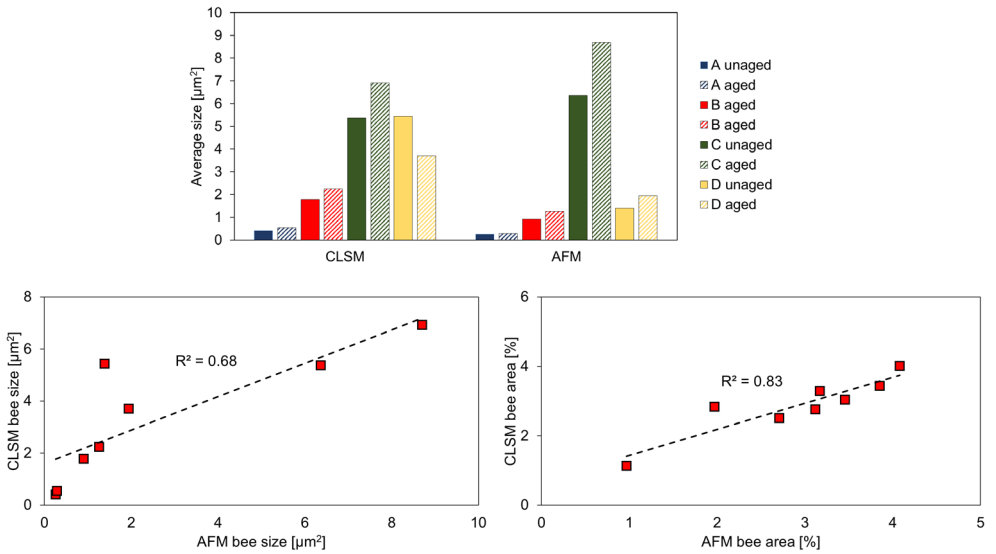

Figure 6-7 Average bee size derived from AFM and CLSM before and after lab ageing [top] and their relationships [bottom]

6.5 **Waveform characteristics of bee structures**

The typical wavy shape of the bee structures was further assessed. An example of such a wave profile along with its calculated waveform characteristics is shown in Figure 6-8. In the statistical analysis, for each valley and peak of all the bee structures the peak height, the valley depth, the wavelength and the projected length were measured. Average data with their standard deviation are presented in Figure 6-9.

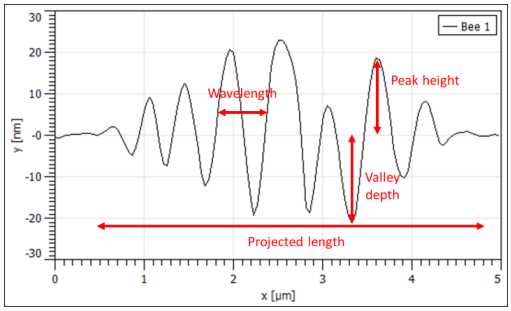

Figure 6-8 Schematic picture of a bee profile and its waveform characteristics in bitumen B

The analysis of these characteristics for the two microscopic techniques examines further their convergence. In Figure 6-9 [left] AFM shows that bitumen C presents the most elongated bee microstructure indicated by the highest average projected length for bitumen C followed by bitumen D, B and A. The projected length from the AFM data seems to decrease with lab ageing. CLSM on the other hand presents an average projected length that is similar for bitumen B, C and D, whereas bitumen A shows the smallest bee length from both microscopies. The effect of ageing in CLSM projected length is not consistent as bitumen A and C increase in length whereas B and D decrease upon ageing. The resolution of the two microscopies may have affected the comparison of the length and wavelength between them. Given this, the bee structure length size ranges between 2000-20000 nm from AFM analysis whereas the CLSM images range between 2000-7000 nm.

Of significant importance is to elucidate the effect of ageing on the wavelength of the waveform that this microstructure presents. AFM demonstrates a wavelength between 500-1100 nm whereas the CLSM findings show a wavelength between 550 and 3500 nm. Bitumen A and B seem unaffected by ageing concerning the distance of the valleys and peaks since their wavelength remains the same, whereas bitumen D reduces its wavelength with ageing. These observations are confirmed by both techniques.

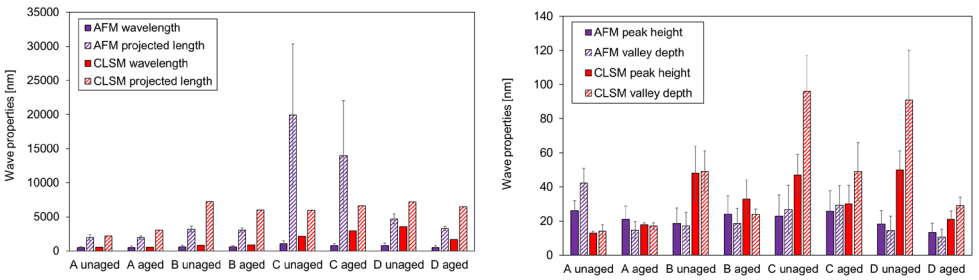

Figure 6-9 Wavelength and projected length [left] and wave height and depth [right] and for all waxy binders before and after lab ageing

The average peak height in Figure 6-9 [right] exhibits values as captured from AFM between 15-30 nm whereas CSLM shows relatively higher values 15-50 nm for the examined binders. Similarly, the valley depth ranges between 10-30 nm for AFM while CLSM reports a depth between 15-100 nm. The direction of ageing is not clear for these two wave characteristics, however, each technique shows a consistent decrease or increase of both values upon ageing.

It is also critical to appreciate the true impact of ageing on the waveform shape for each binder. Therefore, typical shape probability distribution measures were utilised, namely kurtosis, skewness and roughness. Kurtosis originates from the Greek word 'kyrtos' which translates as curved, and a value around 3 shows a normal distribution shape of a wave with a few outliers, whereas negative values indicate a so-called platykurtic distribution with shorter tails. The latter is the case of the wavy formations obtained via AFM images as can be seen in Figure 6-10 [left]. On the other hand, CLSM (Figure 6-10 [right]) shows a relatively normal shape distribution of the waveforms as the values are around 3. The effect of ageing is not consistent between the waxy binders for this characteristic. Skewness provides also some insights into the probability distribution of the wave asymmetry with a value equal to 0 showing a balanced and symmetric waveform. The results of Figure 6-10 show that the skewness, as extracted by AFM, presents a slightly positive value, which assumes the tail is on the left of wave distribution when CLSM fluctuates with regard to this measure. Finally, the surface roughness was consistently reduced upon ageing for bitumen B and D both from AFM and CSLM data. It should be noted that although kurtosis and skewness are unitless the roughness estimations are given in nm and are merged in the same Figure 6-10.

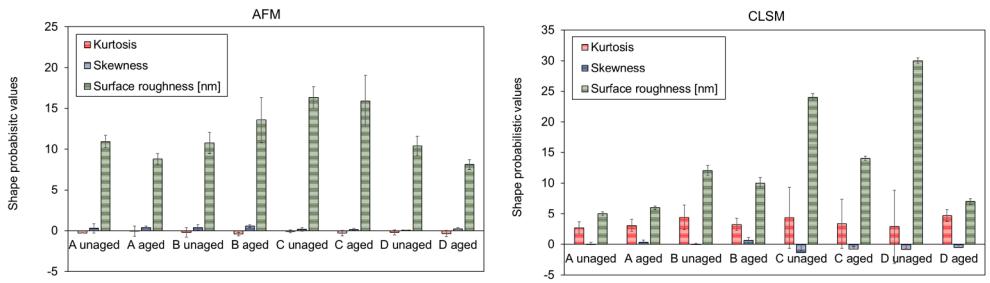

Figure 6-10 Shape probabilistic values with lab ageing for all the waxy binders via AFM [left] and CLSM [right]

6.6 **Bee detection using deep learning and 2-D FFT**

The two microscopic tools proved robust enough to analyse the characteristics of the bee structures before and after lab ageing using commercial software packages for image processing. However, their convergence is worth to be discussed. First of all, AFM can capture clearly in phase contrast the different phases, whereas CLSM cannot identify phases other than the catanaphase. It was found that both techniques agree with regard to the bee coverage and show a sufficient relationship for the bee size. Through waveform characteristics, it becomes possible to highlight the differences between AFM and CLSM for the average peak height, wavelength and length with CLSM reporting in general higher values. From the shape probabilistic measures, clear differences can be seen for kurtosis and surface roughness. The observed differences can originate either from the microscopic technique itself or they can depend on the image processing.

Therefore, Chapter 6 proposes additionally a more sophisticated deep learning algorithm to detect the location of the bee structures in order to investigate their surface roughness. It also suggests a new method based on two-dimensional Fast Fourier Transform (2-D FFT) [192] to identify in the most precise way the wavy characteristics of the bee structures. This additional analysis of Chapter 6 offers to the existing literature a versatile image detection tool and serves towards overcoming a longstanding challenge with respect to the true impact of ageing on the bee structures.

Deep learning is a popular computational method that enables computers to learn from experience and is a subset of machine learning that uses a hierarchical artificial neural network to carry out the desired tasks. This powerful technique has dramatically improved the state-of-the-art in many domains such as visual object recognition and object detection [193]. In this Chapter, deep learning was used for DIC CLSM images of a reference waxy bitumen to detect the bee structures on the surface of the bitumen microstructure before and after long-term lab ageing. A YOLOv3-based

algorithm developed in a Matlab environment is trained and used [194]. Contrary to many other object detection methods, YOLOv3 applies a single neural network to the full image and by dividing the image into multiple regions it predicts bounding boxes and their probabilities for each region. These bounding boxes are weighted by the predicted probabilities.

As presented in Figure 6-11, the proposed deep learning network structure in this Chapter consists of the feature extraction network in SqueezeNet, followed by two detection heads at the end, with the second detection head able to detect smaller bee structures. The network input size is selected to be (277, 277, 3), and all the DIC CLSM images and the bounding boxes are resized to match the input size. Next, with the help of the estimateAnchorBoxes function of Matlab, the number of anchor boxes is selected equal to six with the three larger ones used in the first detection head and the smaller ones assigned to the second detection head. Anchor boxes are a set of predefined bounding boxes of a certain height and width that can help improve the speed and efficiency of the detection portion of the network. Finally, the system is trained on GPU of a laptop with Intel Core(TM) i7-9850H with a clock speed of 2.60 GHz, 32.0 GB RAM, and a GPU of NVIDIA GeForce MX150.

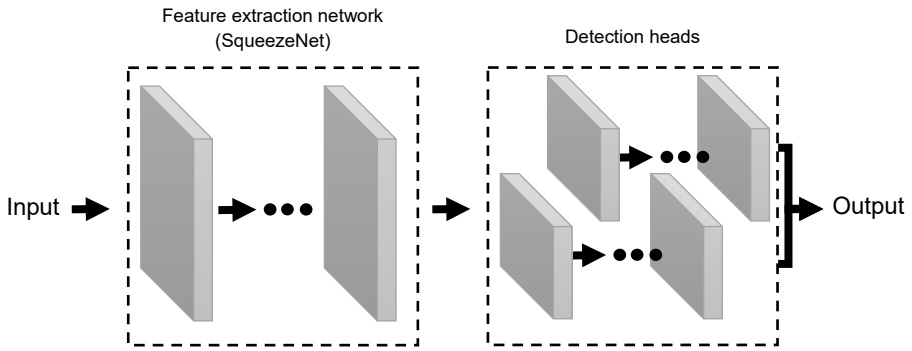

Figure 6-11 Flowchart of the deep learning network used for the bee structures detection

Next, the bee structures on 21 DIC CLSM images are labelled using the Image Labeler application in Matlab. Afterwards, using a data augmentation procedure including random rotation, up to 10% scaling of the images and colour jitter (with no saturation), the number of labelled structures is increased. This allows to increase the variety of the training data, which can improve the accuracy of the trained network. The trained algorithm is finally run for all the images captured from the bitumen surfaces, detecting eventually the present bee structures. After bee detection, the number and the area of the bounding boxes in each image can be calculated and compared in different ageing states. For the reference waxy bitumen used for this detection, the trends with ageing were the same as with commercial image processing.

Certain bee characteristics, such as roughness, can be calculated by the proposed deep-learning bee detection. However, another bee characteristic, prone to human error with commercial image processing, is the wavelength. To overcome this obstacle and automate this process it is necessary to develop a method that can estimate the orientation of each bee (angle of the axis of the bee with respect to the x-axis) in an image. This is done by developing an algorithm based on 2-D FFT, which is an efficient and popular method to remove periodic noise from digital images [195]. More specifically, 2-D FFT in digital image processing is a tool allowing to decompose an image into its sine and cosine components. The output of this transformation represents the image in the frequency domain. After applying a 2-D FFT on an image and plotting the magnitude of the output in the logarithmic scale, two spots with higher values along the direction of the bee structure were visible. All the main frequency contributors to this image in all directions are found by calculating the radially averaged power spectrum. However, it is not possible to obtain the main frequency contributing to the bee pattern in the desired direction. Therefore, it was required to find the direction of the bee in a DIC CLSM image. To find this direction, the image is rotated from 0 to 180 degrees and the averages of the spectrum of the middle 22 pixels (selected based on the range of the bee dimensions) on the x-axis are calculated for each rotation angle. An example of it is depicted in Figure 6-12. Hence, the maximum value shows the direction of the bee. After the bee is rotated, the values along the axis of each bee are selected. Then, the spectrum of this height data is calculated using a one-dimensional Fast Fourier Transform (1-D FFT). The maximum value in the expected region provides the dominant frequency and, consequently, the wavelength of the bee.

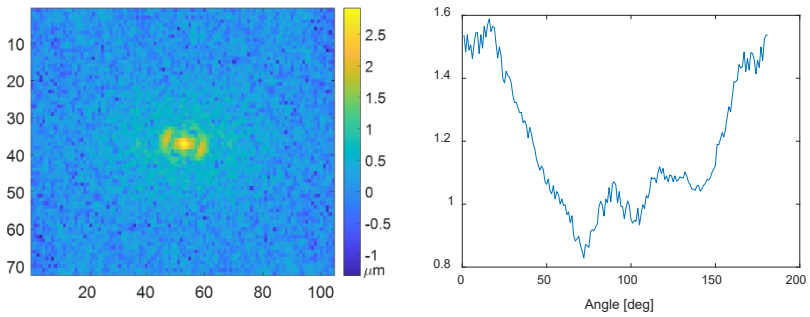

Figure 6-12 CLSM DIC in frequency domain (magnitude of the 2D FFT) [left] and average of the middle 22 pixel values on the x-axis of the spectrum image rotated between 0 to 180 degrees [left]

Using the developed methodology, the wavelength of all detected bee structures can be more accurately estimated showing now a more consistent increasing trend with ageing (from 0.50 µm in the unaged state to 0.55 µm after PAV) for the reference waxy

bitumen, whereas the values with commercial image processing were rather overestimated (see Figure 6-10).

6.7 Highlights of the chapter

- The effect of ageing on the bee structures of waxy binders is systematically investigated using commercial image processing techniques for AFM and CLSM.
- Lab ageing results consistently in a decrease in the number of bees per μm^2 and the bee coverage percentage.
- AFM and CLSM indicate an increased size of the bees with lab ageing.
- Assumptions for the change in the bee properties can be attributed to additional wax crystallisation due to ageing or/and the compatibility of the aged bitumen matrix with the wax.
- A systematic waveform evaluation for the peak height, the valley depth, the projected length of the bee and the wavelength is provided, while there is no clear tendency that can be found with lab ageing.
- Basic probabilistic measures such as kurtosis, skewness and surface roughness of the bee waveform are provided, whereas the effect of ageing on them is not clear.
- A comparison of the AFM and CLSM highlights some differences in certain bee characteristics i.e. wavelength and kurtosis.
- Advanced image processing techniques, based on a deep learning network and 2-D FFT, are developed in this Chapter to more accurately detect and analyse the bee structures in bitumen.

7

CHEMISTRY AND RHEOLOGY OF BITUMEN WITH AGEING

7.1 **Summary**[*]

The ageing of bitumen has received great attention both from a chemical and rheological perspective due to its direct impact on asphalt performance. However, open questions with respect to the convergence of the synchronous ageing changes in rheology and chemistry of bitumen still exist. Chapter 7 addresses these alterations of chemistry and rheology and attempts to propose a phenomenological link fed by fundamental chemical information. To that end, three binders of different type were used in four different laboratory ageing states. A number of spectroscopic techniques and rheological testing were employed to derive corresponding chemical and rheological parameters. In parallel, various statistical methods (Bivariate analysis, Wilcoxon test, Factor analysis) assisted in identifying the relationships among the chemo-rheological parameters and simplifying the number of variables. The results of this Chapter demonstrate clearly that chemistry and rheology are following similar changes when considering laboratory ageing based on the fast-rate phase of a dual oxidation scheme and short-term lab ageing. Finally, this work manages to establish an exclusive linking framework, by means of a training dataset, for a number of newly-introduced rheological parameters. All in all, the results of this Chapter might be particularly interesting for future interventions in the chemical composition of bitumen, considering its effect on performance.

[*]*This chapter is redrafted from: G. Pipintakos et al., Do chemistry and rheology follow the same laboratory ageing trends in bitumen?, Materials and structures (2022). https://doi.org/10.1617/s11527-022-01986-w*

7.2 Objectives

Alternative lab ageing simulations in thin bitumen films under constant conditions of temperature and pressure at different time intervals offer the advantage of oxidation kinetics and have been proven appropriate to track the time evolution of ageing chemistry and the transition point of the rate-determining phases [30,196]. For this transition point (completion of the fast- and initiation of the slow-rate phase) in kinetics, it is still uncertain whether also chemistry would converge if similar rheological performance with standardised lab protocols can be obtained. Hence, the aim of the current Chapter is twofold.

On one hand, Chapter 7 addresses the open question of whether chemistry and rheology follow the same laboratory ageing trends independent of the conditions of the laboratory ageing protocol which is used and, on the other hand, aims to provide a statistical linking framework for advanced rheological parameters using fundamental chemistry of bitumen as input.

The chemo-rheological analyses and statistical methods used for the binders of Chapters 3 and 4 alongside the objectives of Chapter 7 are schematically given in Figure 7-1.

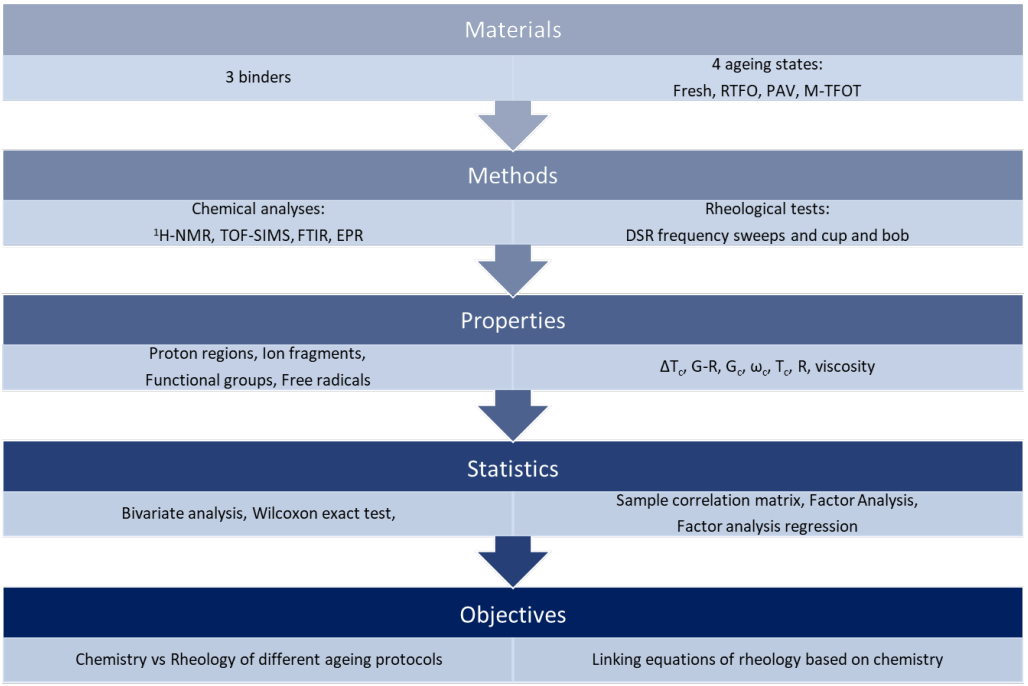

Figure 7-1 Flowchart of the experimental part, statistical analysis and objectives of Chapter 7

7.3 Materials and Methods

The same three bituminous binders A, B and C of Chapters 3 and 4, differing in crude source, distillation and penetration grade were examined to compare their changes in rheology and chemistry during ageing. The reader is referred to Table 3-1 for the basic properties of these binders. Four different laboratory ageing states (unaged state (fresh), RTFO, RTFO+PAV and one time interval of kinetics) were utilised with the primary goal to reveal possible simulation-related differences in bitumen's chemistry and rheology. More specifically, in the initial investigation of Chapter 3, the binders were aged with a M-TFOT up to 56 days at different time intervals and oxidation kinetics were studied and revealed that the completion of the fast-rate oxidation phase and the initiation of the slow-rate oxidation phase for all the three binders was found to be around 8 days. This time interval was additionally used to evaluate the chemical and rheological level of this transition point between the two rate-determining phases with standard lab protocols. In all the subsequent analyses the binder designation is followed by the laboratory ageing simulation used whereas all the parameter values are the average of two replicates for the rheological and three replicates for the chemical values.

Fundamental information derived in Chapters 3 and 4 from advanced spectroscopy is used as chemical input in a statistical framework. The COI, SOI, and ARI indices were eventually utilised for FTIR, the carbon-cased organic radicals CBOR and vanadyl centres (VO^{2+}) for EPR, the chemical distribution of methyl (MetP), methylene (MtlP), α-alkyl (AlkP), olefinic (OleP) and aromatic (AroP) protons for ^{1}H-NMR, as well as representative positive and negative ions for each category of $(OH)_x$, SO_x-containing and PAH TOF-SIMS ion fragments, (OH^-, C_2OH^-, C_4OH^-), ($CHSO^-$, $C_2H_3SO^-$), and ($C_9H_7^+$, $C_{10}H_8^+$, $C_{13}H_9^+$) respectively.

The Chapter is additionally designed with the optimum goal to account for the DSR extracted rheological parameters of R, ΔT_c, Glover-Rowe (G-R), ω_c, G_c, T_c and viscosity. After deriving all the necessary chemical and rheological parameters, the Wilcoxon exact test and the Pearson's r of a bivariate analysis are used as metrics for the equivalence of the properties between standardised ageing and the reaction-rate transition point in kinetics. Employing multivariate statistics by means of sample correlation matrix and factor analysis, the number of original chemical and rheological variables is reduced and further implemented into fitting equations of rheology as a training dataset, using a so-called factor analysis regression. This work finally stresses the goodness of the existing fit between the latent variables of chemistry and the advanced parameters of rheology. In order to accommodate for the potential reader

the use of the utilised statistical methods, their theoretical background and application of them are briefly revisited in the following subsections.

7.3.1 *Pearson's r and Sample Correlation Matrix*

In multivariate data analysis, the association or relationship between the different variables is key. There are different measures to express the linear relationship between two variables. Unlike the sample covariance, the Pearson's product-moment correlation coefficient (*r*) is scale-invariant. That is, its value does not depend on the units or dimensions used. Therefore, the relationships between the different chemical and different rheological parameters between the ageing states were first inspected by the Pearson's *r*, using the statistical software JMP Pro 16. From a mathematical point of view, Pearson's r_{ij} between two variables X_i and X_j is defined according to Equation 7-1.

$$r_{ij} = r_{ji} = \frac{s_{ij}}{\sqrt{s_{ii}}\sqrt{s_{jj}}} \qquad \textit{Equation 7-1}$$

where s_{ij} is the sample covariance between X_i and X_j. If $0 << r_{ij} < 1$ then a positive linear relationship holds between the two variables, while $r_{ij} \sim 0$ indicates no linear relationship. On the other extrema, for values $-1 < r_{ij} << 0$ the variables correlate linearly with a negative relationship. To judge additionally if the assumed correlation is strong or weak the p-value is employed in sample statistics. It shows, in simple words, the probability that a difference has been generated by a random chance. A significance level is usually set (< 0.05) indicating the percentage of risk to reject a certain hypothesis, known as the null hypothesis. For p-values greater than the significance level, they report that the null hypothesis is most likely to occur. For Pearson's r and the accompanying correlation between the variables X_i and X_j the $p < 0.05$ witnesses that the null hypothesis ($r = 0$) in this case is not true, and therefore gives evidence for a certain relationship. In the second phase of the analysis, the chemical and rheological variables were used to construct sample correlation matrices containing as elements the Pearson's r between the different variables.

7.3.2 *Non-parametric Wilcoxon Rank Sum exact test*

Non-parametric statistical hypothesis tests are commonly used for small samples, typically with a number of observations $n < 15$, and especially when assumptions about the underlying data distribution cannot be done. The Wilcoxon exact test is used to test the null hypothesis for each pair of the two levels of a variable *X*. It is the non-

parametric version of the equivalent parametric two-sample t-test. Also in this case the p-value is the key factor for rejecting or not the null hypothesis. Using a significance level of *0.05* for a two-tailed test the null hypothesis is rejected when $p < 0.05$ which can be interpreted as the fact that the medians of the two populations differ significantly, otherwise for $p > 0.05$ the null hypothesis cannot be rejected and therefore provide evidence that the medians tend to be equal. The Wilcoxon exact test was used in this work to examine together with the Pearson's r the two pairs (RTFO and M-TFOT) of each rheological and chemical index.

7.3.3 *Multivariate Factor Analysis*

Exploratory factor analysis is a common method for re-expressing multivariate data. The main assumption in this analysis is that the observed variance in the multivariate data is attributable to a relatively small number of common factors, the so-called latent factors. Prior to this analysis some conditions should be met and scrutinised, such as the existence of one or more groups of variables that are highly correlated as witnessed by a correlation matrix. In general, the mathematical framework of this analysis is based on the idea that for p variables $X = (X_1, X_2, ..., X_p)$ certain correlations exist and depend on $m<p$ common factors $F = (F_1, F_2, \dots F_m)$ as well as on the corresponding p error terms U. Each of the p variables is linearly dependent to the m factors in the common factor analysis which in matrix notation can be written in Equation 7-2.

$$X = LF + U \qquad \textit{Equation 7-2}$$

where L is the loading matrix containing the factor loadings l_{ij} which vary between *-1* and *+1* and can be interpreted as correlations between the original variables and the factors. Of particular interest is that the squared factor loading l_{ij}^2 is the percentage of variance in variable X_i explained by the factor F_j, while the sum of the different squared factor loadings for a variable X_i is known as communality. In other words, communality shows the proportion of the variation in X_i accounted by all the common factors. Additionally, in factor analysis, the given m number of factors is, initially, based on the researcher's choice and later is verified by the cumulative percentage of the total variance explained by the selected number of factors. As a rule of thumb, the number of factors is chosen in such a way that can explain more than 70% of the total variation and has also a meaningful interpretation [93]. Simplifying the interpretation of the factors is also necessary as obtained by the factoring method i.e. principal axis, because the obtained factors are not unique. One possible simplification method is by

rotating the factors i.e. by the Varimax rotation method, which is used in the statistical software JMP Pro 16.

7.3.4 *Factor analysis regression*

Frequently the factor analysis is not an end step but rather an intermediate step to further data analysis. One useful application of the factors is to use them as independent variables in multiple linear regression, which is called factor analysis regression. The goal is to model the linear relationship between the independent factors derived from chemistry and a response variable, in this case, a rheological value. Hence, the location of each of the original chemical variables in the reduced factor space is needed, which is alternatively called the factor scores for the latent factors. JMP Pro 16 allows exporting the factor scores which are used as independent variables in a factor analysis regression described in Equation 7-3.

$$Y_i = b_o + b_1 \cdot F_{i1} + b_2 \cdot F_{i2} + \ldots b_m \cdot F_{im} + \varepsilon \qquad \textit{Equation 7-3}$$

where Y_i is the dependent rheological variable *i*, F_{ij} is the independent chemical factor score *j* for the prediction of the dependent variable *i,* b_0 is the y-intercept (constant term), b_j are the slope coefficients for each independent chemical factor score *j* and ε is the residual (error term). Some assumptions such as the linearity, the independence of observations, the normality of the residuals and the homoscedasticity should also hold here for a factor analysis regression. Finally, a statistical metric to explain the degree of variation of the outcome based on the variation of the independent variables is the coefficient of determination (R^2) with values close to 1 indicating a small prediction error.

7.4 **The effect of lab ageing protocol**

The rheological behaviour of the binders is depicted by means of master curves in Figure 7-2. A master curve is a useful illustration providing an overview of the effect of the different ageing states on a broader frequency/temperature domain. Consistent with previous works this study affirms that ageing increases the complex modulus and decreases the phase angle of bitumen. This can be seen mainly in the low-frequency/high-temperature domain of the master curves and the differences because of ageing become more apparent for bitumen C in a wider frequency range. Besides this, binder A as expected based on its bitumen grade presents higher values of complex modulus in a wider low-temperature/high-frequency domain compared to

binders B and C. In general, it is believed that ageing at low temperatures, like the one used in M-TFOT, affects to a greater level the low-temperature properties compared to ageing performed at higher temperatures, like in RTFO. Moreover, high-temperature ageing changes mainly the shape parameters of a master curve. Counterbalancing these changes due to different ageing temperatures can be possibly achieved with an appropriate selection of the ageing duration.

Of particular importance is the convergence of the M-TFOT and RTFO master curves for all the binders. It has been shown that the transition point between the two rate-determining oxidation phases under the specific conditions of M-TFOT occurs around 8 days. The findings here support an association between this ageing state (8 days M-TFOT at 50 °C) and the standardised laboratory simulation for short-term ageing (RTFO at 163 °C), while the binders exhibited their most extreme values after PAV ageing. The comparability of the two ageing states is further investigated using statistical analysis.

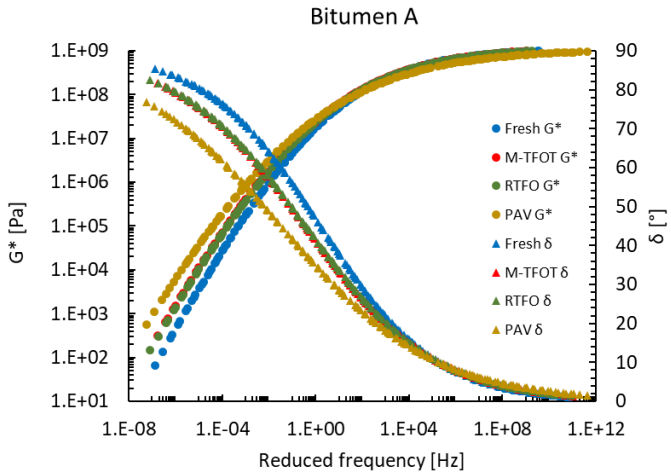

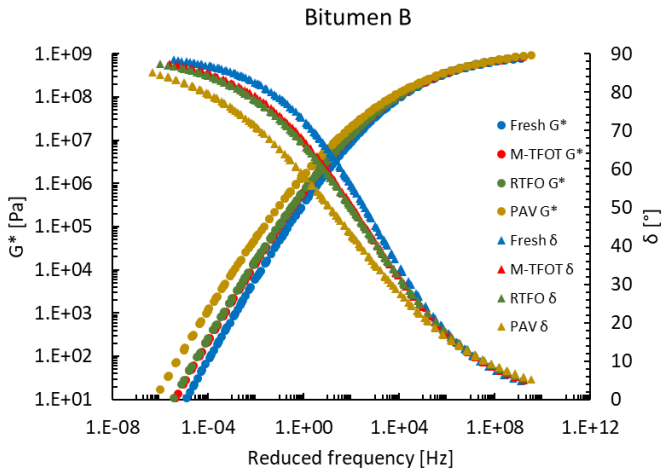

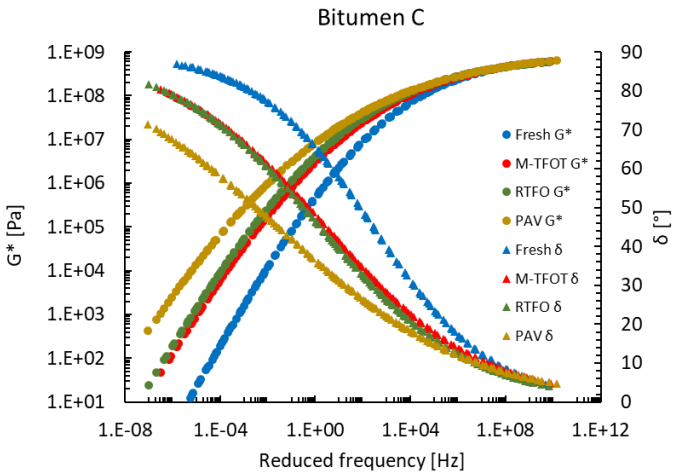

Figure 7-2 CA master curves shifted to a reference temperature of 15 °C for all the binders and ageing states

To examine the initial observation of the rheological convergence of M-TFOT and RTFO as well as the corresponding evolution of the chemical parameters, bivariate analysis was first used. This analysis will allow concluding whether binders that differ in terms of type follow the same evolution separately for their rheological and their chemical changes, irrespective of the ageing simulation. The two ageing states are treated as a dependent and independent variable with two sets of values (domains), namely chemical and rheological, including all three binders. The chemical parameters include all the parameters investigated and explained in the previous section, whereas the rheological parameters extracted from the master curves are used as another domain. Differentiation between the binders from a chemical perspective can be mainly seen in their intensity as depicted in Figure 7-3 [top], something which is particularly pronounced for the CBOR and ARI of bitumen C. Moreover, since the values differ in terms of magnitude two bivariate plots are performed for each domain to exclude the effect of magnitude errors. Figure 7-3 shows these bivariate plots per domain as well as the bivariate fits that are performed. This analysis can be helpful in testing simple convergence between the two states. As can be seen, the parameters of the two states seem to fit well in a linear relationship between them. It can also be seen that with regard to the radical formation of binder C the convergence of the two ageing states is lower than the other two binders. The reason for this observation may be found in the considerably different type of this binder considering its origin and refinery process.

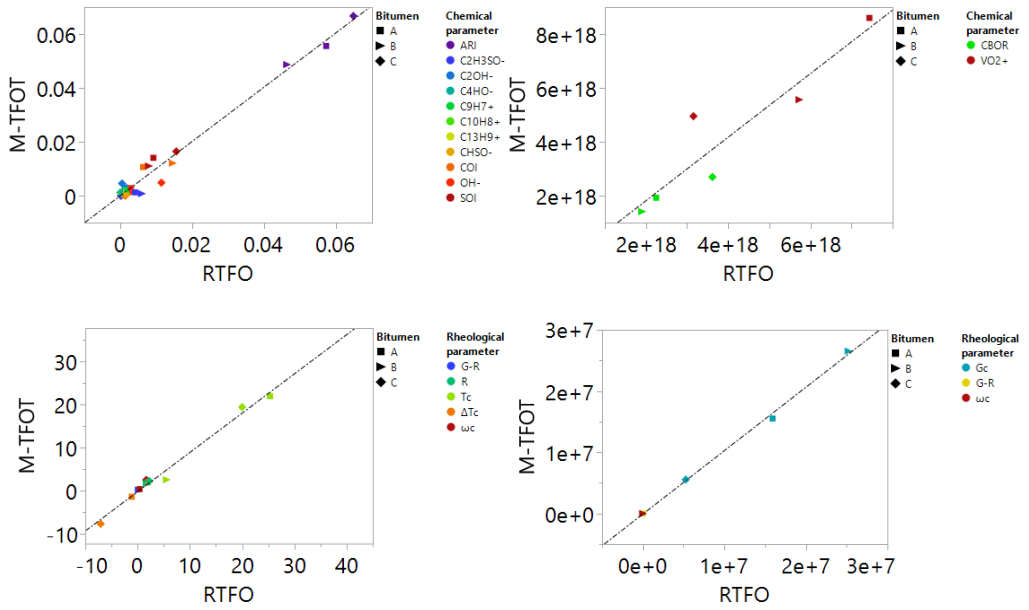

Figure 7-3 Bivariate plots of all chemical [top] and rheological parameters [bottom] between M-TFOT and RTFO

To further clarify the relationship between M-TFOT and RTFO the statistics of the bivariate analysis are provided in Table 7-1. The number of observations is based on the average values for each chemical or rheological parameter, thus, it is much higher in reality. The parameter estimation for coefficient *b* of the bivariate fits presents values close to the unit which means that they correlate in a fashion *y=x* with the intercept *a* interpreted here as the error between the values for each state. This holds both for the rheological and the chemical parameters, as well as for low and high magnitude values. In addition, the Pearson's *r* shows a strong positive correlation of this relationship with values close to 1. The significance of this positive correlation between the two states for both sets of parameters is further justified by the p-values, which are much lower than the threshold level of 0.05**.** The coefficient of determination ($R^2 \sim 1$) for the suggested fits is adequate to support the fitting choice and establish a reliable relationship between the two states. That is, not only the initial observation of the convergence of the master curves is valid but also the bivariate analysis for the rheological values confirms this claim. In parallel, the chemical parameters for the same ageing states show a significant level of convergence which implies that chemistry can follow the rheological ageing trends in bitumen for different ageing simulations and vice versa.

Table 7-1 Summary of bivariate statistics between M-TFOT and RTFO

Parameters	Fit	Magnitude of parameters	Parameter estimates		Pearson's r	Significance (p-value)	R^2	Observations N
			a	b				
Chemical	RTFO= a + b·M-TFOT	Low	3.43E-6	1.009	0.933	<0.0001	0.979	33
		High	-5.38E+17	1.079	0.932	0.0068	0.868	6
Rheological	RTFO= a + b·M-TFOT	Low	-0.227	0.912	0.997	<0.0001	0.994	13
		High	-87610	1.037	0.999	<0.0001	0.997	5

To further ensure that each parameter in the previous domains for all the binders is at least comparable in terms of distribution of values between the two ageing states, the Wilcoxon Rank Sum exact test was performed. The selection of this test is explained by the small number of observations for each numerical parameter. Table 7-2 shows that the p-values for all the parameters suggest in favour of the null hypothesis (*$p > 0.05$*), therefore pointing to similar centres of location between the two levels of the grouping variable of ageing state, in this case, M-TFOT and RTFO. The lowest p-values which can be interpreted here as having the highest probability to show different distribution between the two states were found for the $(OH)_x$ and SO_x-containing ion fragments as well as the SOI. This test strengthens the existence of convergence between the two ageing states not only for their domains but also for the individual parameters.

Together the two statistical approaches show that similar levels of rheological and chemical parameters can be succeeded between the transition point (8 days) of the oxidation kinetics with M-TFOT and routine lab simulation of short-term ageing. It is fair enough to consider that although the ageing protocol differs i.e. RTFO incorporates airflow and rotation contrary to M-TFOT, once the same ageing level has been reached in terms of rheological performance, the chemistry of bitumen can follow the same trend and vice-versa, by means of a balance of ageing temperature and time.

Another point, worth to be highlighted here, is the fact that although the temperature difference in the two protocols differs significantly when examining more meaningful derived rheological parameters, it seems that the change in duration can well compensate for the temperature difference.

In the following statistical analysis, to avoid overloading the analysis with similar values of RTFO and M-TFOT which converge to similar ageing severity both for rheology and chemistry, only the chemorheological values of RTFO are utilised.

Table 7-2 Output of Wilcoxon tests for each parameter of M-TFOT and RTFO

Statistical method	Grouping variable with 2 levels	Parameter	Analysis of numerical parameter	p-value
Wilcoxon Rank Sum exact test	RTFO & M-TFOT	Chemical	SOI	0.4
			COI	1.0
			ARI	1.0
			CBOR	0.7
			VO^{2+}	1.0
			OH-	0.4
			C_2OH^-	0.1
			C_4OH^-	0.1
			$CHSO^-$	0.4
			$C_2H_3SO^-$	0.4
			$C_9H_7^+$	0.7
			$C_{10}H_8^+$	0.7
			$C_{13}H_9^+$	1.0
		Rheological	G_c	1.0
			T_c	0.7
			ω_c	1.0
			R	1.0
			ΔT_c	0.7
			G-R	1.0

7.5 **Link between chemistry and rheology by ageing state**

It remains to be seen if the fundamental information can be used to estimate certain rheological values and their change with ageing. Three ageing states (unaged, RTFO and PAV) for all different binder types were chosen within the framework of multivariate statistics in this study. Preliminary investigation of relationships is a requirement so that one is able to apply more sophisticated exploratory analysis i.e. factor analysis.

Hence, the parameters are first grouped into chemical and rheological. Correlation matrices are formed and shown in Table 7-3 and Table 7-4. Typically a correlation matrix is a symmetric matrix including as elements the exact correlations, as realised by the Pearson's r, between two parameters. This is particularly useful to decide on a specific threshold under which correlations are important. For consistency, only one part of the symmetric correlation matrices is given as well as only the strong correlations ($|r| > 0.7$) are presented with increasing intensity of redish colour for values of $|r|$ between 0.7-0.8, 0.8-0.9 and 0.9-1.0 respectively. It is demonstrated numerically that several correlations exist between the different chemical parameters, a fact that suggests that multivariate exploratory factor analysis can be performed for this category.

Possible explanations for the different chemical correlations can be found based on the chemical family that the compounds belong to or on their role in the ageing process. To name some of them, the SOI and CBOR have been used to distinguish the two rate-determining changes and can explain well the transition point of a fast-rate followed by a slow-rate oxidation phase. PAH of $C_{13}H_9^+$, $C_{10}H_8^+$ and $C_9H_7^+$ seem to correlate well with ARI of the same chemical family. The SO_x-containing fragments show also a strong correlation between them. Possible explanations behind the strong positive or negative correlations of specific protons with OH_x-containing fragments may be found in the change of molecular associations which needs to be revealed in further studies. In general, it is believed that the individual contribution of each chemical change could have a significant effect on rheological performance although the relative increase may not be the same between the ageing states for rheology and chemistry.

Table 7-3 Correlation matrix of chemical parameters

	SOI	COI	ARI	CBOR	VO^{2+}	OH^-	C_2OH^-	C_4HO^-	CHSO-	$C_2H_3SO^-$	$C_9H_7^+$	$C_{10}H_8^+$	$C_{13}H_9^+$	AlkP	MetP	OleP	MtlP	AroP
SOI	1.00																	
COI		1.00																
ARI			1.00															
CBOR	0.75			1.00														
VO^{2+}					1.00													
OH^-				0.87		1.00												
C_2OH^-			-0.73		0.70		1.00											
C_4HO^-			-0.77		0.81		0.96	1.00										
$CHSO^-$									1.00									

$C_2H_3SO^-$									0.99	1.00								
$C_9H_7^+$			-0.77	-0.79	0.79	-0.72	0.85	0.94			1.00							
$C_{10}H_8^+$			-0.82	-0.76	0.81		0.86	0.95			0.99	1.00						
$C_{13}H_9^+$			-0.89		0.78		0.88	0.94			0.95	0.98	1.00					
AlkP			0.72				-0.75							1.00				
MetP			-0.93				0.91	0.93			0.86	0.90	0.96	-0.80	1.00			
OleP							-0.74							0.79	-0.76	1.00		
MtlP	0.82			0.83													1.00	
AroP			0.78		-0.83		-0.72	-0.81			-0.79	-0.86	-0.91		-0.88			1.00

Next, to minimise the number of independent variables, i.e. chemical parameters, in order to implement them in a fitting scheme of dependent ones i.e. rheological, possible relationships of the dependent variables should also be identified. Previous scholars have already reported a variety of relationships between these rheological parameters. Taking into account these well-documented relationships, the correlation matrix provided in Table 7-4 and the meaningful interpretation of the parameters explained previously in Chapter 2, the governing and most important rheological parameters were selected. Therefore, the crossover value G_c together with the R, ΔT_c and η_{135} $^{\circ}C$ are chosen that can capture the viscoelastic response, the relaxation, ageing-induced cracking and workability issues that occur due to ageing.

Table 7-4 Correlation matrix of rheological parameters

	G_c	T_c	ω_c	R	ΔT_c	G-R	η_{135oC}
G_c	1.00						
T_c	-0.74	1.00					
ω_c	0.78		1.00				
R	-0.87	0.84		1.00			

ΔT_c	0.88	-0.78		-0.90	1.00		
G-R						1.00	
η_{135oC}						0.95	1.00

Given that the conditions to perform a factor analysis are supported by the correlation matrix of the chemical parameters, these parameters are further incorporated in the statistical software JMP Pro 16. After investigating the number of factors that can explain the total variance of the parameters, three factors proved satisfactorily to explain the total variance of the chemical parameters. The cumulative percentage of the variance explained by the three factors is 87.26% indicating that the three factors can adequately describe the total variance according to a threshold level of 70%. The rotated factor loading matrix and the communality estimates are also considered crucial to better understand and interpret the formulation of the factors which are able to reduce the number of the original chemical parameters. Table 7-5 clearly indicates the borders of the three factors that are highlighted for the parameters with a high factor load. More specifically, the rotated factor loadings (Varimax rotation method) in Table 7-5 support that Factor 1 loads heavily on $C_{13}H_9^+$, COI, MetP, $C_{10}H_8^+$, C_4HO^-, $C_9H_7^+$, $VO^{2+,}$ C_2OH^-, ARI, AroP, OleP and AlkP and can account for 43.84% of the total variance. This factor explains primarily the formation and consumption of the ageing products. $C_{13}H_9^+$, COI, MetP, $C_{10}H_8^+$, C_4HO^-, $C_9H_7^+$, VO^{2+}, C_2OH have a positive effect on this Factor 1 while the proton regions have a negative effect. On the other hand Factor 2 loads on SOI, MtlP, CBOR, OH^- which are factors that have been shown to have an association with the transition between the fast and slow-rate phase of an oxidation scheme [30,97]. This Factor accounts for 24.79% of the total variance while Factor 3 explains 18.64% of the total variance. Factor 3 loads heavily on the sulfoxide-related products of $CHSO^-$ and $C_2H_3SO^-$. Furthermore, the total proportion of the variation per chemical variable by all the factors can be understood by the communality of each variable. The total communality estimates (Table 7-5) are acceptable (> 0.7) for all the parameters accounted for by the three factors. The lowest communality can be found for the vanadyl species VO^{2+}, where a possible explanation for this observation can be the differences that have been observed for binders of different crude sources for this value; a fact that the multivariate statistics are not able to capture adequately.

Table 7-5 Rotated factor loading and final communality of factor analysis for the chemical parameters

Chemical Parameter	Rotated factor loading			Final communality estimates
	Factor 1	Factor 2	Factor 3	
$C_{13}H_9^+$	0.884	-0.407	0.190	0.982

COI	0.854	0.162	0.023	0.756
MetP	0.846	-0.318	0.384	0.965
$C_{10}H8^{+}$	0.843	-0.512	0.096	0.981
$C4HO^{-}$	0.782	-0.478	0.349	0.961
$C_9H_7^{+}$	0.772	-0.594	0.106	0.959
$VO2^{+}$	0.740	-0.320	-0.061	0.653
C_2OH^{-}	0.709	-0.367	0.546	0.936
SOI	0.041	0.901	-0.252	0.877
MtlP	-0.120	0.883	-0.259	0.861
CBOR	-0.405	0.872	0.004	0.924
OH-	-0.399	0.723	0.159	0.707
ARI	-0.761	0.331	-0.302	0.779
AroP	-0.932	0.149	-0.033	0.891
OleP	-0.750	-0.019	-0.511	0.684
AlkP	-0.788	-0.186	-0.647	0.926
$CHSO^{-}$	0.114	-0.146	0.956	0.948
$C_2H_3SO^{-}$	0.055	-0.167	0.941	0.917

Up to this point, it was possible to minimise the number of chemical parameters for all the binders and ageing states in three factors by means of factor analysis. The factor scores of this analysis were extracted and successively implemented in a factor analysis regression, where the independent factors are the factors scores for each ageing state of each bitumen and the dependent factors are the rheological parameters that have been chosen from the correlation matrix (Table 7-4). The coefficients of the factor analysis regression are shown in Table 7-6 together with the corresponding coefficient of determination.

The advantage of these linking equations is among others that the number of independent variables is relatively small and the goodness of fit is evidenced to be high enough by the R^2 values for the G_c, R and ΔT_c rheological parameters. The viscosity fit is characterised as weak. The linking framework seems to differentiate the rheological properties derived in different temperature ranges, where the higher testing temperature results in a weaker fitting equation. It is also possible that the incorporation of a variety of factors in the binder's resistance to flow may overload the fitting equation since this rheological parameter is rather simple compared to the more advanced parameters derived from the master curves and can be fitted by fewer chemical parameters i.e. carbonyls [6,90] . The estimation of the parameters of this training dataset also shows the strength of the chemical parameters per binder and their effect on rheology.

Table 7-6 Factor regression analysis between chemical and rheological parameters

Rheological parameter	Factor analysis regression	Parameter estimates				R^2
		a	b	c	d	
G_c	y = a + b·FS1 + c·FS2 + d·FS3	15919191	2671103.7	-8653879	2144094.8	0.741
R		1.981	-0.055	0.335	-0.137	0.825
ΔT_c		-1.763	1.738	-3.021	1.391	0.914
$\eta_{135\,^oC}$		1467.022	738.742	235.789	-447.663	0.288

Finally, the actual and predicted (via the chemical analysis) rheological parameters are plotted in Figure 7-4. The graphs highlight the convergence of the actual and predicted values for three of the four parameters. Moreover, since correlations exist between the crossover values one is able to estimate the rest of the rheological values. The fact that the ageing effect can be taken into account in these values shows that fundamental chemistry plays a significant role in bitumen's performance. Looking back to the fundamentals of bitumen chemistry and its evolution with ageing, as well as the effect on the latent factors and the factor analysis regression will allow for the understanding of the chemical indices that deserve special attention. Moreover, the necessity to further support these observations, so that a clear quantification of the crucial chemical components can be done, should be tackled by additional validation datasets.

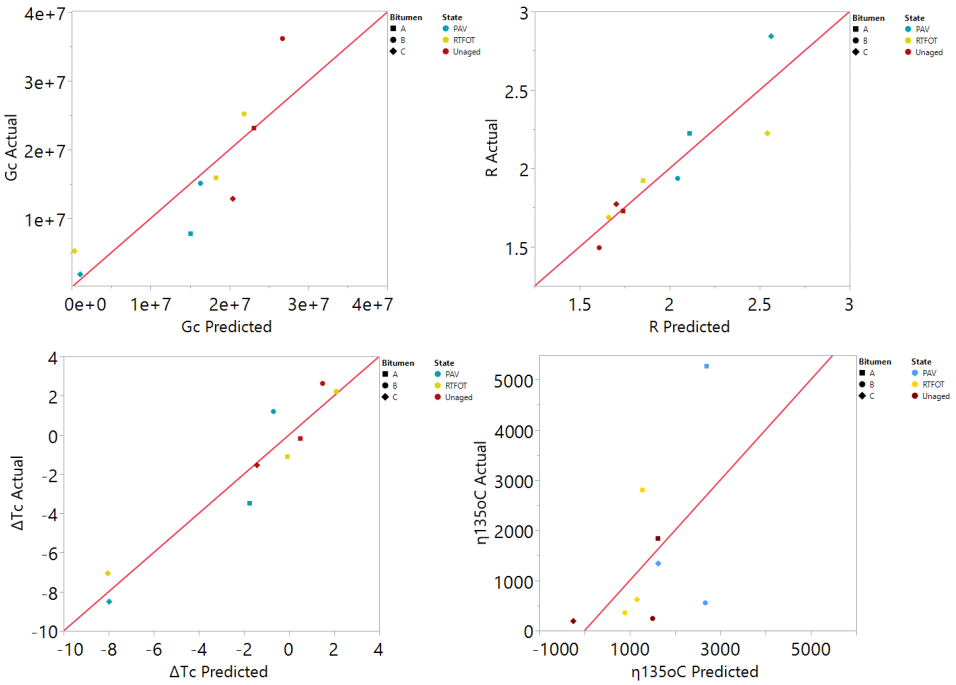

Figure 7-4 Statistically predicted and actual rheological values in bivariate plots of the training dataset

7.5 Highlights of the Chapter

- A linking framework of a training dataset between the rheological performance and bitumen's fundamental chemistry is established.
- A variety of statistical methods are utilised such as bivariate analysis, correlation matrices, the Wilcoxon exact test, Factor analysis and regression for the different variables.
- This Chapter explores the convergence of bitumen chemistry among different ageing simulations. In particular, investigation of two short-term ageing simulations indicates for the examined dataset that besides rheology also bitumen chemistry can follow similar ageing trends.
- The phenomenological framework of this Chapter supports that advanced rheological values, such as ΔT_c, can be fairly accurately estimated (R^2 = 0,91) only if a number of fundamental chemical parameters is taken into account.
- For more basic rheological properties, i.e. viscosity, the number of chemical parameters needed for an acceptable estimation may be less.
- Multivariate statistics show their great potential to understand the association of the laboratory ageing changes in bitumen's chemistry and rheology.

8

THERMODYNAMICS MODELLING OF AGEING MECHANISMS IN BITUMEN

8.1 **Summary**[*]

Reaction-diffusion models derived within the frame of continuum thermodynamics of irreversible processes (TIP) for reacting mixtures enjoy a number of advantages over purely phenomenological models. Chapter 8 explores the potential of this approach by means of a particular model for the fast rate-determining phase of oxidation in bitumen. Film ageing experiments are simulated considering different bitumen compositions in terms of SARA fractions. The predicted fast-rate phase completion times are contrasted with parameters characterising the initial composition and the results demonstrate the consistency of the model accounting for the fast-rate oxidative mechanisms of bitumen.

8.2 **Objectives**

In phenomenological modelling efforts, like the ones described in Chapter 7, interrelationships between the different scales are captured almost exclusively by purely empirical relations and phenomenological parameters. A concept for modelling the oxidative ageing of bitumen which rests on TIP is proposed in this Chapter, adopting a continuum perspective [24,197,198]. This model aims to establish direct

[*]*This chapter is redrafted from: U. Mühlich et al., Mechanism based diffusion-reaction modelling for predicting the influence of SARA composition and ageing stage on spurt completion time and diffusivity in bitumen, Construction and Building Materials (2020). https://doi.org/10.1016/j.conbuildmat.2020.120592*

links with the underlying molecular structure and the oxidative mechanisms of bitumen, reviewed experimentally in Chapters 3 and 4, by means of physically meaningful parameters such as solubility and molar volumes. The model presented in this Chapter attempts additionally to distinguish between different SARA compositions. Finally, to judge the capabilities of this model, the predicted oxidation times are contrasted with experimental results and trends reported in the literature.

8.3 Materials and Methods

Two bituminous binders A and B of Chapters 3, 4 and 7 were chosen to track the progress of oxidation for the sulfoxide evolution, depicted previously in Figure 3-4. As mentioned in Chapter 3, a M-TFOT for bituminous films of 1 mm thickness, at 50 °C was used for the ageing kinetics and the chemical fingerprinting of them was recorded by FTIR at different time intervals.

To design reasonable SARA compositions as input for TIP modelling, the possible ranges for the individual fractions in the literature were taken into account [26,52,199]. As such the interval between zero and hundred percent is partitioned into fragments of five percent. Three groups are defined with saturates content of 5, 10 and 15 %, respectively. Compositions are generated using standard combinatorics, more specifically by generating combinations with repetitions excluding cases with less than four individual fractions, i.e. compositions with only saturates and resins or only saturates, resins and aromatics are excluded. In total, there are 1076 possible compositions. However, the number reduces to 49 when applying the constraints given in Table 8-1.

Table 8-1 Data in terms of SARA fractions with known constraints from literature

SARA fraction	Range [wt. %]	Constraints based on literature
Saturates	5-15	Saturates < Aromatics
Aromatics	40-65	Saturates ≤ Resins
Resins	20-45	Aromatics > Asphaltenes
Asphaltenes	5-25	Resins ≥ Asphaltenes

$$I_c = \frac{Asphaltenes + Saturates}{Resins + Aromatics} \qquad \textit{Equation 8-1}$$

A further reduction is achieved by using the Gaestel index (I_c) in Equation 8-1 [200]. This index has been used in several studies as an indicator of the colloidal instability of bitumen. It is believed that the increase of asphaltenes (included in the numerator of this index) can lead to an unstable colloidal system, as this fraction and its representative molecules are of the highest polarity in bitumen. Previous studies utilising binders from different crude oils suggested limits for this index, within which

the bitumen is considered to perform adequately well [50]. Excluding all SARA compositions with an I_c, not within 0.1 and 0.6, yields eventually 14 virtual compositions, presented in Figure 8-1.

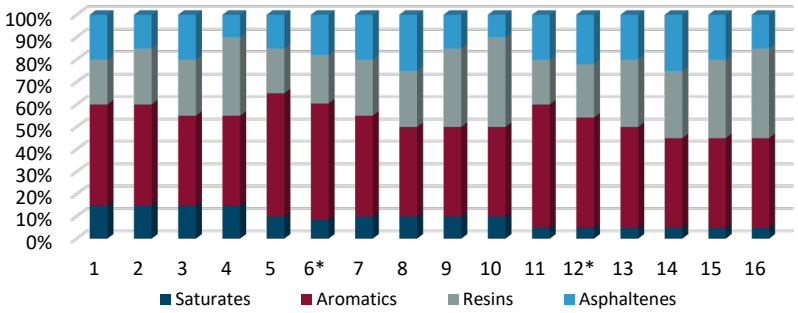

Figure 8-1 SARA compositions used in this study, where columns 6 and 12 refer to the compositions of the real bitumens A and B, respectively, whereas all other compositions are generated artificially

In addition, the SARA composition of the two real binders A and B was determined by the Thin Layer Chromatography-Flame Ionisation Detector (TLC-FID) method using an IATROSCAN MK-6s. The fractionation was performed according to IP 469/01 [48]. For this method, the bitumen sample is diluted in dichloromethane solutions, after which the solution is applied on a silica-coated quartz rod. Then, different solvents are used for the development of the bitumen sample. Three rods were prepared for each bitumen and the rods were passed, afterwards, through the flame ionisation detector inside the analyser. The chromatograph produced indicated four main peaks attributed to each of the calculated SARA fractions used for this Chapter.

8.4 Mechanism-based reaction-diffusion model

The model proposed in this work considers a simplified version of the fast-rate oxidation phase and its mechanisms. The corresponding reaction can be simplified as follows. An oxygen molecule comes close to a saturated ring, situated between two aromatic rings. Two hydrogen atoms are taken off from the saturated ring, which converts the latter into an aromatic ring. If sulfur atoms are available, then the oxygen and the two hydrogen atoms form a water molecule and sulfoxide.

To incorporate this mechanism into a reaction-diffusion model, the following five species are defined, numbered in the following by $\alpha=1,\ldots,5$: oxygen (1), water (2), aromatised compounds (ARA^*) with one S=O (3), aromatisable compounds with traces of sulfur (*ARA*) (4) and saturates (5). Each *ARA* member can only participate once in the following simplified chemical reaction

$$1O_2 + 1ARA \rightarrow 1ARA^* + H_2O \qquad \textit{Equation 8-2}$$

ARA denotes an average molecule accounting for the effects of asphaltenes, aromatics and resins. Saturates are considered separately because they do not participate in the reaction. For the chemical potentials of the individual species Equation 8-3 is used with the chemical potential of the pure species being μ_α^0, molar fractions χ_α, and activity coefficient γ_α.

$$\mu_\alpha = \mu_\alpha{}^0 + \ln \chi_\alpha + \ln \gamma_\alpha \qquad \textit{Equation 8-3}$$

Regarding the activity coefficient, the most simple available model which accounts for differences in size between the representative species is chosen [201] in Equation 8-4.

$$\ln \gamma_\alpha = \frac{v_\alpha^*}{RT}[\delta_\alpha - \overline{\delta}]^2 \qquad \textit{Equation 8-4}$$

The presence of physically meaningful parameters such as molar volumes of pure species in liquid state v_α^*, and solubilities δ_α, allows for establishing direct links between molecular level and continuum scale. The mean solubility of the mixture, $\overline{\delta}$ is given by Equation 8-5

$$\overline{\delta} = \frac{\sum_{\alpha=1}^{N} \delta_\alpha v_\alpha{}^* \chi_\alpha}{\sum_{\beta=1}^{N} v_\beta{}^* \chi_\beta} \qquad \textit{Equation 8-5}$$

Due to Equation 8-2, all molar fractions can be expressed in Equation 8-6 based on the molar fractions of oxygen and water (χ_1, χ_2) and the initial molar fractions of saturates $\chi_5{}^0$.

$$\begin{aligned} \chi_3 &= \chi_2 \\ \chi_5 &= \chi_5{}^0[1-\chi_1-\chi_2] \\ \chi_4 &= [1-\chi_5{}^0][1-\chi_1-\chi_2]-\chi_2 \end{aligned} \qquad \textit{Equation 8-6}$$

Assuming that only oxygen diffuses implies that all other species remain on average in their spatial locations. Therefore, the model reduces to two essential mass balances in Equation 8-7, which read in terms of molar concentrations

$$\begin{aligned} \partial_\tau c_1 + \frac{1}{M_1}\mathrm{div}\vec{J} &= -\Lambda \\ \partial_\tau c_2 &= \Lambda \end{aligned} \qquad \textit{Equation 8-7}$$

with molar mass of oxygen, M_1, diffusion flux vector $\vec{J}$ and reaction rate density Λ. The partial derivative with respect to time is indicated by ∂_τ while div is used for the spatial divergence operator. The components of $\vec{J}$ with respect to a Cartesian coordinate system defined by coordinates x_j, j = 1, 2, 3 read in terms of molar fractions as follows.

$$J_{1j} = -L[j_1\chi_{1,j} + j_2\chi_{2,j}] \qquad \textit{Equation 8-8}$$

where $\chi_{\alpha,k}$ indicates the gradient of a quantity χ_α with respect to the spatial coordinate χ_k. The terms j_1, j_2 in Equation 8-8 are given by

$$j_1 = 1 + \frac{\chi_1}{1-\chi_1-\chi_2} + \chi_1\frac{\partial A_{15}}{\partial\chi_1},\ j_2 = 1 + \frac{\chi_1}{1-\chi_1-\chi_2} + \chi_1\frac{\partial A_{15}}{\partial\chi_2}, \qquad \textit{Equation 8-9}$$

$$\text{with } A_{15} = \frac{v_1^*[\delta_1-\bar{\delta}]^2 - v_5^*[\delta_5-\bar{\delta}]^2}{RT} \qquad \textit{Equation 8-10}$$

Concerning the reaction rate density, the methodology proposed in [202] is used, which relies on representing the reaction rates by polynomials in activities. Hence, similar to the diffusion part, molecular level and activity models can be linked by means of activity models with physically meaningful parameters and information about the SARA fractions. As such, the final result for the reaction rate density is expressed in

$$\Lambda = B_{14}\chi_1[[1-\chi_5{}^0][1-\chi_1-\chi_2]-\chi_2]\exp\left(\frac{v_1^*[\delta_1-\bar{\delta}]^2}{RT}+\frac{v_4^*[\delta_4-\bar{\delta}]^2}{RT}\right) \qquad \textit{Equation 8-11}$$

where B_{14} is the reaction parameter, R is the ideal gas constant and T is the absolute temperature. To simplify the discussion, only problems which are captured sufficiently well by a one-dimensional version of the model are considered in the following. In this case, there is only one active component of the diffusion flux vector in Equation 8-8 which is simply called J in the following and it reads

$$J = -L[j_1\chi_1' + j_2\chi_2'] \qquad \textit{Equation 8-12}$$

where the prime indicates the derivative with respect to the spatial coordinate denoted by z.

8.5 SARA compositions and fast-rate oxidation phase

To estimate the properties of the *ARA*-species, a pure *ARA*-mixture with mass fractions β_{4k} is considered, where k =1, 2, 3 refer to asphaltenes, resins and aromatics,

respectively. The average molecular weight assigned to an ARA-molecule is computed by means of the weighted arithmetic mean

$$M_4 = \sum_{k=1}^{3} \beta_{4k} \mathrm{M}_{4k}, \text{ where } \beta_{4k} = \frac{{w_{4k}}^0}{1 - {w_5}^0} \qquad \textit{Equation 8-13}$$

and the molar volume is computed analogously. The *ARA*-solubility, δ_4, is estimated by adjusting the concept of mean solubility in Equation 8-5. Hence,

$$\delta_4 = \frac{\sum_{k=1}^{3} \delta_{4k} {v_{4k}}^* {\chi_{4k}}^0}{\sum_{m=1}^{3} {v_{4m}}^* {\chi_{4m}}^0} \qquad \textit{Equation 8-14}$$

where the molar fractions χ_{4k} are obtained from initial mass fractions w_{4k}^0. The values of δ_4 given in Table 8-2 differ only slightly from the arithmetic mean δ_4^*=63246 $\sqrt{g/cms^2}$. In addition, assumptions that the properties of ARA and ARA* are the same in terms of molecular mass, volume and solubility are made. Literature values [203,204] used for all the subsequent computations are given in Table 8-3.

Table 8-2 Initial compositions and average parameters of an ARA-molecule used in simulations

SARA number	Initial composition in mass fractions				Parameters used in simulations			
	Saturates	Asphaltenes	Resins	Aromatics	χ_5^0	M_4	v_4^*	δ_4
	w_5^0	w_{41}^0	w_{42}^0	w_{43}^0		[g/mol]	[cm³/mol]	$[\sqrt{g/cms^2}]$
1	0.150	0.200	0.200	0.45	0.421	1525	1335	63155
2	0.150	0.150	0.250	0.45	0.386	1318	1170	62807
3	0.150	0.200	0.250	0.40	0.426	1557	1364	62967
4	0.150	0.100	0.350	0.40	0.353	1144	1034	62277
5	0.100	0.150	0.200	0.55	0.271	1239	1101	63008
6	0.082	0.187	0.217	0.52	0.247	1356	1197	63036
7	0.100	0.200	0.250	0.45	0.310	1495	1313	62983
8	0.100	0.250	0.250	0.40	0.341	1721	1497	63137
9	0.100	0.150	0.350	0.40	0.285	1331	1185	62479
10	0.100	0.100	0.400	0.40	0.254	1136	1029	62156
11	0.050	0.200	0.200	0.55	0.167	1411	1240	63165
12	0.052	0.220	0.238	0.49	0.184	1520	1332	63095
13	0.050	0.200	0.300	0.45	0.173	1468	1293	62830
14	0.050	0.250	0.300	0.40	0.193	1682	1468	62974
15	0.050	0.200	0.350	0.40	0.176	1497	1320	62662
16	0.050	0.150	0.400	0.40	0.157	1313	1172	62353

Table 8-3 Parameter values of each species used in simulations

Species	Density	Molecular mass	Molar volume	Solubility	
	g/cm³	*g/mol*	*cm³/mol*	*√MPa*	$\sqrt{g/cms^2}$

Oxygen	1.114	32	28.0	14.0	44272.2
Water	0.988	18	18.2	48.0	151790.4
Asphaltene	1.200	4500	3750.0	20.0	63246.0
Resins	1.054	990	940.0	19.0	60083.7
Aromatics	1.006	440	437.0	21.0	66408.3
Saturates	0.887	370	417.0	16.5	52177.9

Next, in order to estimate the required time for the completion of the fast-rate oxidation phase (spurt completion time t_{SCT}), the compositions of the two real binders A and B and their ageing kinetics by means of sulfoxide evolution are contrasted. In parallel, virtual film ageing experiments are performed by simulating the reaction-diffusion process using the model presented in the previous section. The oxygen uptake (C_{O_2}) can be computed by integrating the spatial distribution of oxygen concentration in a bituminous film of thickness h at a given time t based on Equation 8-15.

$$C_{O_2}(t) = \int_0^h c_1(z,t)dz \qquad \textit{Equation 8-15}$$

Furthermore, the simulated spurt completion time t_{SCT}^{sim} is defined as the time at which oxygen uptake stops. The simulations require proper estimates regarding the parameters L and B_{14} of Equation 8-8 and Equation 8-11 that control the diffusion speed and reaction rate respectively, which can be derived from the FTIR kinetics of Chapter 3 for binders A and B. As such, thin films of h =1 mm are used in M-TFOT and the oxygen uptake is estimated for similar films via the developed reaction-diffusion model, whereas for the free oxygen surface the molar concentration value c_1^s = 8.1E-07 mol/cm^3 from literature, is used [19]. The parameters L and B_{14} are eventually estimated by applying a least square method for the two binders A and B, comparing their experimental t_{SCT}^{exp} (where the change of the initial rapid increase is followed by an almost constant slope during the slow-rate phase) and the t_{SCT}^{sim}. This demands that

$$[t_{SCT,A}{}^{sim} - t_{SCT,A}{}^{sim}]^2 + [t_{SCT,B}{}^{sim} - t_{SCT,B}{}^{sim}]^2 \rightarrow \min \qquad \textit{Equation 8-16}$$

The convergence of the experimental and simulated t_{SCT} in order to back-calculate the required parameters is presented schematically in Figure 8-2.

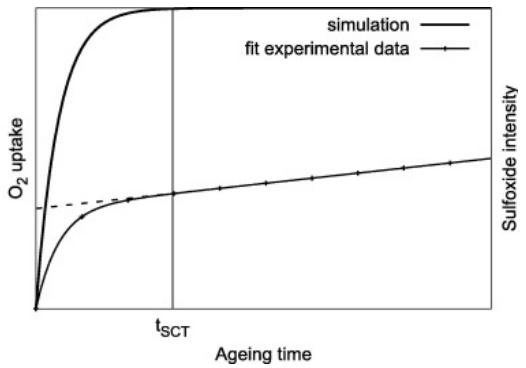

Figure 8-2 Schematic illustration for the determination of the spurt completion time via experiments and simulations

After providing as input to the model reliable parameters by coupling it with experimental results, the effect of SARA fractions on the t_{SCT}^{sim} was investigated for a sensitivity analysis of the compositions of Table 8-2. Figure 8-3 [left] shows the predicted spurt completion time t_{SCT}^{sim} for all virtual compositions as a function of the molecular mass of an *ARA* molecule M_4 and the initial weight percentage of saturates w_5^0. It should be noted that all simulations are performed with the same L and B_{14}. Hence, pressure, density and volume are kept constant. Therefore, an increase in M_4 implies less ARA molecules per reference volume, in other words, less molecules to be oxidised. As Figure 8-3 [left] illustrates, the model predicts consistently a decrease in spurt completion time for given w_5^0 and increasing M_4. On the other hand, increasing w_5^0 while keeping M_4 constant causes certainly a decrease in the number of *ARA* molecules, but simultaneously the number of saturates molecules increases. Due to the difference between the molecular masses of saturates and *ARA*, one *ARA* molecule corresponds to about four saturates. Since individual mass fractions have to sum up to one, increasing w_5^0 by adding four saturates, for example, requires to remove only one ARA molecule from the system. Therefore, diffusion becomes more time-consuming because an oxygen molecule may need to pass more saturates to come close to an ARA molecule. Thus, the model predicts an increase in spurt completion time with increasing w_5^0 which is consistent. Furthermore, Figure 8-3 [left] depicts that the spurt completion time depends in a non-linear manner on M_4 and w_5^0. This is to be expected because diffusion flux (Equation 8-8) and reaction rate density (Equation 8-11) are highly nonlinear.

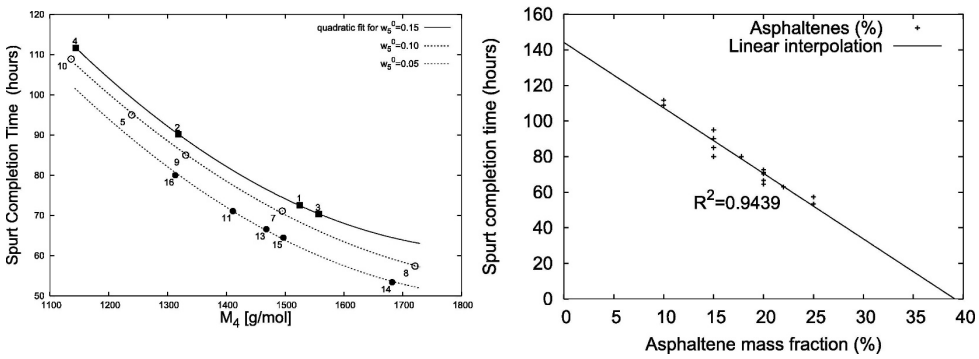

Figure 8-3 Spurt completion time as a function of the molecular mass of the ARA molecule for different initial weight percentages of saturates [right] and asphaltene content [left].

The spurt completion time in Figure 8-3 [right] was found to decrease with increasing asphaltene content. Assuming the same bitumen in two different ageing states, according to experimental observations, the asphaltene content is evidenced to be increased in the more severe ageing state. Thus, it can be suspected that in this ageing state a sufficient amount of O_2 has at least reacted with the hypothesised average ARA molecule, indicating that the remaining time upon ideal spurt completion time will be reduced compared to the initial less aged state. This is also adequately captured by the model in Figure 8-3 [right].

8.6 Highlights of the chapter

- Contrary to purely phenomenological reaction-diffusion models, models developed within the TIP framework can account for bitumen's composition in terms of SARA fractions.
- Hypotheses about oxidation mechanisms at the molecular scale are implemented in a continuum thermodynamics model in this Chapter by means of activity models.
- The developed mechanism-based model captures expected trends in terms of the completion time of the fast-rate oxidation phase in bitumen.
- Coupling of experiments and modelling allows for the estimation of reliable parameters that control the reaction rate and diffusion speed.

9

CONCLUSIONS AND RECOMMENDATIONS

9.1 **Conclusions**

The conclusions that can be drawn from the current doctoral thesis considering the initial research objectives are summarised below per thematic section as given in Figure 1-2.

To revisit briefly these objectives, this thesis explored via a number of spectroscopic, gravimetric, thermoanalytical, microscopic techniques and rheological characterisation, the oxidative ageing mechanisms in bitumen. This was investigated both for ageing kinetics and lab ageing simulations taking into account the origin, manufacturing and performance differences between different binders and their fractions. Moreover, this work examined the reason behind the surface microstructure in bitumen and the effect of oxidative ageing on it. Finally, efforts to link the fundamental chemistry with the rheological response were presented and a novel thermodynamics reaction-diffusion model was shown in this dissertation.

9.1.1 ***Molecular level***

In this part, at the molecular level, three binders varying in distillation, origin, wax content and empirical performance as well as their fractions were used as the reference material. Specific answers, as extracted by the experimental program (FTIR, EPR, TOF-SIMS, ^{1}H-NMR, DSC and DVS) of Chapters 3 and 4, are given with regard to the objectives set initially for this research project.

I. It became possible to support via EPR and FTIR a dual-oxidation scheme that consisted of two rate-determining phases. The formation of organic carbon-centred radicals and sulfoxide formation was in line with hypotheses about the ageing mechanisms of bitumen supporting the existence of a fast and a slow rate-determining phase.

II. Both ageing kinetics and routine lab ageing simulations of RTFOT and PAV showed that in bitumen the relative amount of vanadyl-porphyrin metal species remained constant, a fact that can be used to trace back the origin of the crude source.

III. Oxygenated products after the completion of the fast-rate phase included sulfoxide, nitrogen, aliphatic, PAHs and oxygen-containing compounds as revealed by TOF-SIMS analyses, regardless of the bitumen type. For the latter, these can be alcohols or carboxylic acids.

IV. The EPR analyses demonstrated that after RTFOT and PAV ageing the organic carbon-centred radicals show a similar effect as with ageing kinetics, for the underlying ageing mechanisms. The fast-rate phase governs the formation of carbon-centred radicals which provokes the continuation of the slow-rate phase in bitumen.

V. A chemical classification of bitumen via ^{1}H-NMR was shown. Slight changes were found with lab ageing for the relative proton distribution on bitumen, irrespective of the bitumen type.

VI. SARA fractionation showed that asphaltenes after PAV are more oxidised and aromatised than the corresponding aged maltenes as supported by FTIR.

VII. Chemical classification of the polarity-based fractions showed that bitumen and maltenes change similarly with ageing when it comes to their relative proton distribution.

VIII. The effect of crystallisable compounds in the bitumen composition was apparent on the bitumen surface via high-resolution images of TOF-SIMS, realised as aliphatics. Besides this the effect of bitumen's source, refinery process and type were minor when it comes to the ageing mechanisms. The crystallisable compounds after SARA fractionation are gathered mainly in the maltenes as investigated with DSC, with this effect being more obvious upon PAV ageing.

IX. Exploration of different film thicknesses and temperatures allowed the estimation of activation energies and reaction rates in bitumen. More

specifically, the thinner the bitumen film, the more pronounced the reaction contribution of the coupled reaction-diffusion and thus the higher the reaction rate.

X. A novel technique, namely DVS, was used in combination with an inert filler to estimate the coupled reaction-diffusion parameters. Diffusion coefficients for bitumen and oxygen solubility were able to be back-calculated using a modified Fickian law and FE simulations.

9.1.2 *Microscale*

In this second part, consisting of the outcome of Chapters 5 and 6, a waxy and a wax-free binder were used for supporting one of the hypotheses in the literature, based on the presence of wax in bitumen, about the mechanisms of the bitumen microstructure via DSC, WAXD and CLSM. Later, this batch was expanded into four waxy and two wax-free binders to comprehensively evaluate microscopically (AFM and CLSM) the effect of ageing on them and give answers to the initial objectives of this dissertation.

I. Considering the wax theory about bitumen's surface, the crystallisable compounds if present in bitumen may be the reason for the so-called bee-structures. This was experimentally investigated following real-time microstructure evolution with CLSM and utilising thermoanalytical techniques of DSC and WAXD. Interrelationships of the endothermic and exothermic DSC transitions, the X-ray diffraction patterns and the bee structures were identified within the same temperature ranges, a fact that shows, based on a certain hypothesis (wax theory), that crystallinity may be the reason behind the bee structures' formation.

II. Only the waxy bitumen presented thermal transitions and crystalline diffractions, while with WAXD it was shown that the crystalline material is organised in an orthorhombic unit cell consisting most likely of n-alkanes.

III. The real-time microstructure evolution of the relative bee structure coverage was investigated with an in-house heating/cooling apparatus and was in good correspondence with the WAXD patterns and the relative crystallinity. The cooling/heating rate affected the appearance/disappearance of the bee structures.

IV. A systematic analysis of the long-term lab ageing with PAV was performed in this project for four waxy binders with CLSM and AFM. Two image processing methods of commercial software packages and a deep learning algorithm for bee detection were proposed. It appeared that the normalised to the unaged

state relative bee area coverage is a suitable metric for the effect of ageing on the crystallisable compounds as it is scale-free.

V. Consistently, all the considered binders presented an increased size of the bee structures after PAV, a decreased relative bee coverage and normalised number of bee structures. Possible reasons for these changes may be found in the additional crystallisation of the waxes with ageing and their compatibility with the bitumen matrix.

VI. AFM and CLSM were in good agreement regarding the morphological characteristics of the bee structures, whereas differences were observed for some of their waveform characteristics (wavelength) and probabilistic measures (kurtosis). This was attributed to the working principle of each technique, with AFM being a near-contact method compared to CLSM.

9.1.3 *Phenomenological and mechanism-based modelling*

In the last part of this dissertation, in Chapter 7 the results of molecular level were combined statistically for the three types of binders and were linked with their rheological performance to shed light on the relationships of different ageing simulations and the role of chemistry on performance. A thermodynamics model was also formed in Chapter 8 accounting for the SARA composition via a sensitivity analysis for sixteen different binders. Both Chapters 7 and 8 managed to meet the objectives imposed at the beginning of this doctoral project.

I. The severity of the oxygenated products (free radicals, ions, protons and other chemical compounds) after the completion of the fast rate-determining phase of oxidation kinetics and RTFOT were compared with bivariate analysis, correlation matrices and the Wilcoxon exact test. This analysis showed that similar levels can be achieved between these ageing states.

II. Similarly, advanced rheological properties such as the crossover values and ΔTc also converged when chemistry reached similar levels independent of the ageing simulation used. This enables a direct comparison of the oxidation phases with lab ageing simulations, in other words, RTFOT can adequately account for the short-term ageing phase, although different time duration, air flow and temperatures are used compared to the M-TFOT.

III. A phenomenological framework to link the changes in fundamental chemistry taking into account the oxidation mechanisms and the rheological response by means of advanced DSR parameters was selected for a training dataset. It employed useful multivariate statistical tools such as the Factor analysis and eliminated the number of variables to only three.

IV. The results of this phenomenological model supported that, first, the ageing effect can be sufficiently incorporated, while secondly, for basic rheological properties, like viscosity, the model should be simplified in terms of chemistry input parameters.

V. In order to account for a scheme which dives into the ageing mechanisms and its SARA properties, a thermodynamics of irreversible processes model was constructed in this project. The fast rate-determining phase and its mechanisms were considered in this model and linked the chemical potentials, the activity coefficients and the solubilities of the SARA fractions.

VI. A sensitivity analysis of the SARA fractions was performed and M-TFOT lab simulations were combined with the mechanism-based model to back-calculate realistic parameters to feed the model. This allowed discussing the bitumen's composition, accounting simultaneously for the oxidation mechanisms.

VII. The designed model is able to efficiently predict trends for the completion time of the fast rate-determining phase. For example, it demonstrated that a more oxidised bitumen will contain more asphaltenes and thus the time until the completion of the fast-rate phase will be reduced.

9.2 **Recommendations**

Based on the extensive work conducted around the fundamental chemistry of bitumen and its microstructure, some potential improvements are identified at the end of this project. Specific recommendations for ongoing and future studies are given in the following.

I. The fundamental understanding of the ageing mechanisms in bitumen was based on a limited number of unmodified and waxy binders of different crude sources and refinery processes. A wider batch of binders including not only the oxidative ageing effect on the bitumen matrix but also the polymer degradation is recommended to be studied by future scholars to unravel the balance between the two; the ageing and the polymer degradation. The current dissertation can work as a guideline for newly proposed experimental techniques used in order to further understand the ageing phenomenon from a fundamental basis in binders modified with plastics, renewable, rejuvenated and other sustainable bio-binders.

II. Out of this thesis, it is recommended to use the currently available lab ageing protocols only for comparative studies between binders and the effect of

certain additives. The effects of reactive oxygen species, humidity, and ultraviolet radiation are not considered in the current standardised lab protocols. However, researchers worldwide work independently on these specific factors and it is recommended to bridge the independent findings for the development of a more realistic model, closer to field ageing. This model could contain a more precise conditioning and duration of the slow-rate/long-term oxidation phase from a fundamental point of view, in order to predict more accurately the in-situ ageing.

III. A global dataset will be of great importance to be made not only for researchers but also for authorities and producers when designing new asphalt mixtures and their components. This will assist in improving the bitumen composition and prolong eventually the target of each stakeholder, the lifetime of pavement. Initiating by this, in-situ binders can be extracted and used as a reference with standard lab simulations. At least the binder type, the date of paving, the polymer percentage and other information regarding the bitumen's composition and rheology should be recorded in a global database by the contractors so that the role of each can be better understood and quantified. Given that this information will be made available the phenomenological model constructed in this dissertation can be validated and enhanced by such datasets.

IV. The modelling results of this dissertation can be used in ongoing monitoring programs within and outside the Road Engineering Research Section (like the Fibre Bragg Gratings project) in order to back-calculate the chemical/rheological behaviour of bitumen. In addition, to scale up in upper mortar and mixture levels by including the rest components (filler, sand and aggregates), it should be first made clear if the examined oxidised binder is part of the coating of aggregates or of the 'free' binder in the mix. This can be possibly achieved by making use of FTIR microscopy, or following techniques used in the current dissertation such as the TOF-SIMS. Additionally, a more sophisticated processing of NMR spectra can be used together with in-situ EPR monitoring of asphalt.

V. In this project relationships between fundamental chemistry and rheology were proposed via appropriate modelling. In the literature, empirical limits for advanced rheological parameters such as the cracking initiation exist i.e. *G-R* and *ΔTc*. Following the same rationale and the phenomenological framework proposed herein, limits for the bitumen's chemistry can be imposed. This means that future intervention via additives, antioxidants, and

rejuvenators can be manufactured with the optimum goal to reach this target. Therefore, this thesis can be used as a reference and guideline in order to compare the impact of different additives to each other and the reference binder. The potential chemical limits will be strengthened when more validation datasets will become available in the scientific community. Validation datasets can also point towards the oxygenated products that are affected primarily by oxidative ageing as expressed by the predictive model coefficients.

VI. Conflicting recommendations exist until nowadays for the sample preparation of bitumen for microscopic and spectroscopic investigations. The current dissertation, after extensive CLSM and AFM microscopic imaging, suggests a consistent sample preparation of such specimens between different labs in order to keep the obtained images free from additional ageing and artefacts. Similar sample preparation can be followed for the different spectroscopic techniques, without necessarily the need for a heating plate and a flat specimen. Additionally, at least three samples should be investigated in different spots of the specimen to avoid bias in the interpretations. The current dissertation recommends the following step-by-step sample preparation:

   a. The microscopic sample preparation should start with a high-temperature treatment to create a workable and homogenous material. The temperature and heating time are chosen based on bitumen type and ageing state and is often between 110 and 160 °C. Even though higher temperatures have also been used in the literature, this can cause additional ageing in the material and is not recommended.

   b. A sample holder (microscopic slide) is placed horizontally on a heating plate set at a temperature 140 - 160 °C. A bitumen drop is placed on the sample holder and left until a smooth surface (1-2 minutes) with sufficient thickness is obtained.

   c. The sample is left inside a dust-free environment for two hours to cool down to the ambient temperature. If applicable, the cooling rate is kept between 2 °C/min and 3.4 °C/min to obtain similar cooling conditions of bitumen during asphalt mixture compaction.

   d. Finally, images can be taken at different time intervals, using a non-contact microscopic technique, to keep the surface of the samples free of any artefacts.

VII. The interpretation of the microstructure should be based in the near future not only on human interpretations but also on image processing of the obtained images which provides useful information with regard to meaningful metrics affected by ageing. Following the different image processing methods of this work, similar methods can be applied to modified binders as well as rejuvenated ones.

VIII. In this research project, it was not possible to study the effect of nanoscale of the multiscale ageing phenomenon. This should be taken into account by future peers in order to link existing theories of bitumen's structure i.e. nanoaggregation model with bulk information. WAXD and SAXS are recommended to be used before and upon ageing for this purpose and can be modelled by molecular dynamic simulations.

IX. Finally, the thermodynamics model developed in this dissertation in Chapter 8 can be expanded to incorporate both the fast and the slow rate-determining phase. Although the slow-rate phase can follow various chemical paths compared to the fast-rate, with reasonable simplifications the fundamental mechanisms can be finally used as the basis to scale up to the bitumen's performance

REFERENCES

[1] Eurobitume, The Bitumen Industry: A Global Perspective, 2011.

[2] Asphalt Institute Inc. and European Bitumen Association-Eurobitume, The bitumen industry: A global perspective, 2015.

[3] J.S. Moulthrop, M. Massoud, The SHRP Materials Reference Library, Washington DC, 1993.

[4] X. Lu, P. Sjövall, H. Soenen, Structural and chemical analysis of bitumen using time-of-flight secondary ion mass spectrometry (TOF-SIMS), Fuel. 199 (2017) 206–218. https://doi.org/10.1016/j.fuel.2017.02.090.

[5] J.C. Petersen, R.E. Robertson, J.F. Branthaver, P.M. Harnsberger, J.J. Duvall, S.S. Kim, H.U. Bahia, R. Dongre, C.E. Antle, M.G. Sharma, Binder Characterization and Evaluation Volume 4 : Test Methods, Washington DC, 1994.

[6] J.C. Petersen, R. Glaser, Asphalt Oxidation Mechanisms and the Role of Oxidation Products on Age Hardening Revisited, Road Mater. Pavement Des. 12 (2011) 795–819. https://doi.org/10.1080/14680629.2011.9713895.

[7] L.M. De Carvalho, C.S. Grassmann, C. Paulo, D. Bohrer, A.C. Fröhlich, C.K. Hoinacki, F.R. Adolfo, L.E. Claussen, M. Cravo, L.F.M. Leite, Distribution of sulfur compounds in Brazilian asphalt cements and its relationship to short-term and long-term aging processes, Constr. Build. Mater. 117 (2016) 72–79. https://doi.org/10.1016/j.conbuildmat.2016.04.111.

[8] P.E.Y. Wang, Y. Wen, K. Zhao, D. Chong, A.S.T. Wong, Evolution and locational variation of asphalt binder aging in long-life hot-mix asphalt pavements, Constr. Build. Mater. 68 (2014) 172–182. https://doi.org/10.1016/j.conbuildmat.2014.05.091.

[9] F. Wang, Y. Xiao, P. Cui, J. Lin, M. Li, Z. Chen, Correlation of asphalt performance indicators and aging Degrees : A review, Constr. Build. Mater. 250 (2020) 118824. https://doi.org/10.1016/j.conbuildmat.2020.118824.

[10] X. Lu, U. Isacsson, Effect of ageing on bitumen chemistry and rheology, Constr. Build. Mater. 16 (2002) 15–22. https://doi.org/10.1016/s0950-0618(01)00033-2.

[11] M.C. Cavalli, M. Zaumanis, E. Mazza, M.N. Partl, L.D. Poulikakos, Aging effect on rheology and cracking behaviour of reclaimed binder with bio-based rejuvenators, J. Clean. Prod. 189 (2018) 88–97. https://doi.org/10.1016/j.jclepro.2018.03.305.

[12] X. Hou, F. Xiao, J. Wang, S. Amirkhanian, Identification of asphalt aging characterization by spectrophotometry technique, Fuel. 226 (2018) 230–239.

https://doi.org/10.1016/j.fuel.2018.04.030.

[13] A.A.A. Molenaar, E.T. Hagos, M.F.C. van de Ven, Effects of Aging on the Mechanical Characteristics of Bituminous Binders in PAC, J. Mater. Civ. Eng. 22 (2010). https://doi.org/10.1061/(ASCE)MT.1943-5533.0000021.

[14] J. Mirwald, D. Maschauer, B. Hofko, H. Grothe, Impact of reactive oxygen species on bitumen aging – The Viennese binder aging method, Constr. Build. Mater. 257 (2020) 119495. https://doi.org/10.1016/j.conbuildmat.2020.119495.

[15] A. Sreeram, A. Masad, Z. Sootodeh Nia, D. Maschauer, J. Mirwald, B. Hofko, A. Bhasin, Accelerated aging of loose asphalt mixtures using ozone and other reactive oxygen species, Constr. Build. Mater. 307 (2021) 124975. https://doi.org/https://doi.org/10.1016/j.conbuildmat.2021.124975.

[16] A. Margaritis, G. Pipintakos, G. Jacobs, D. Hernando, M. Bruynen, J. Bruurs, W. Van den bergh, Evaluating the role of recycling rate and rejuvenator on the chemo-rheological properties of reclaimed polymer-modified binders, Road Mater. Pavement Des. (2021). https://doi.org/10.1080/14680629.2021.1905700.

[17] B. Hofko, M.Z. Alavi, H. Grothe, D. Jones, J. Harvey, Repeatability and sensitivity of FTIR ATR spectral analysis methods for bituminous binders, Mater. Struct. 50 (2017) 187. https://doi.org/10.1617/s11527-017-1059-x.

[18] J.C. Petersen, A Review of the Fundamentals of Asphalt Oxidation (E-C140), Transp. Res. Rec. J. Transp. Res. Board. (2009). https://doi.org/10.17226/23002.

[19] P.R. Herrington, Diffusion and reaction of oxygen in bitumen films, Fuel. 94 (2012) 86–92. https://doi.org/10.1016/j.fuel.2011.12.021.

[20] J. Mirwald, S. Werkovits, I. Camargo, D. Maschauer, B. Hofko, H. Grothe, Understanding bitumen ageing by investigation of its polarity fractions, Constr. Build. Mater. 250 (2020) 118809. https://doi.org/10.1016/j.conbuildmat.2020.118809.

[21] M. Zhang, P. Hao, S. Dong, Y. Li, G. Yuan, Asphalt binder micro-characterization and testing approaches : A review, Measurement. 151 (2020) 107255. https://doi.org/10.1016/j.measurement.2019.107255.

[22] L. Eberhardsteiner, J. Füssl, B. Hofko, F. Handle, M. Hospodka, R. Blab, H. Grothe, Influence of asphaltene content on mechanical bitumen behavior: experimental investigation and micromechanical modeling, Mater. Struct. 48 (2015) 3099–3112. https://doi.org/10.1617/s11527-014-0383-7.

[23] H.R. Fischer, A. Cernescu, Relation of chemical composition to asphalt microstructure – Details and properties of micro-structures in bitumen as seen by thermal and friction force microscopy and by scanning near-filed optical

microscopy, Fuel. 153 (2015) 628–633. https://doi.org/https://doi.org/10.1016/j.fuel.2015.03.043.

[24] U. Mühlich, G. Pipintakos, C. Tsakalidis, Mechanism based diffusion-reaction modelling for predicting the influence of SARA composition and ageing stage on spurt completion time and diffusivity in bitumen, Constr. Build. Mater. 267 (2021). https://doi.org/10.1016/j.conbuildmat.2020.120592.

[25] X. Yu, N.A. Burnham, M. Tao, Surface microstructure of bitumen characterized by atomic force microscopy, Adv. Colloid Interface Sci. 218 (2015) 17–33. https://doi.org/10.1016/j.cis.2015.01.003.

[26] The Shell Bitumen Handbook, 6th edition, ICE Publishing, 2015. https://doi.org/10.1680/tsbh.58378.

[27] L. Loeber, G. Muller, J. Morel, O. Sutton, Bitumen in colloid science: A chemical, structural and rheological approach, Fuel. 77 (1998) 1443–1450. https://doi.org/10.1016/S0016-2361(98)00054-4.

[28] S. Ren, X. Liu, P. Lin, R. Jing, S. Erkens, Toward the long-term aging influence and novel reaction kinetics models of bitumen, Int. J. Pavement Eng. (2022) 1–16. https://doi.org/10.1080/10298436.2021.2024188.

[29] X. Jin, R. Han, Y. Cui, C.J. Glover, Fast-rate-constant-rate oxidation kinetics model for asphalt binders, Ind. Eng. Chem. Res. 50 (2011) 13373–13379. https://doi.org/10.1021/ie201275q.

[30] G. Pipintakos, H.Y. Vincent Ching, H. Soenen, P. Sjövall, U. Mühlich, S. Van Doorslaer, A. Varveri, W. Van den bergh, X. Lu, Experimental investigation of the oxidative ageing mechanisms in bitumen, Constr. Build. Mater. 260 (2020) 119702. https://doi.org/10.1016/j.conbuildmat.2020.119702.

[31] J. Knotnerus, Oxygen uptake by bitumen solutions as a potential measure of bitumen durability, Am. Chem. Soc. Div. Pet. Chem. 16 (1971) D37–D59.

[32] T. Mill, The role of hydroaromatics in oxidative aging in asphalt, ACS Div. Fuel Chem. Prepr. 41 (1996) 1245–1248.

[33] G. King, Oxycyclics : Understanding catalyzed oxidation mechanisms in bitumen and other petroleum products, Fuel Sci. Technol. Int. 11 (1993) 201–238. https://doi.org/10.1080/08843759308916063.

[34] P. Herrington, B. James, T.F.P. Henning, Validation of a Bitumen Oxidation Rate Model, Transp. Res. Rec. J. Transp. Res. Board. 2632 (2017) 110–118. https://doi.org/10.3141/2632-12.

[35] J. Petersen, P. Harnsberger, Asphalt Aging: Dual Oxidation Mechanism and Its Interrelationships with Asphalt Composition and Oxidative Age Hardening, Transp. Res. Rec. J. Transp. Res. Board. 1638 (1998) 47–55. https://doi.org/10.3141/1638-06.

[36] P.K. Das, R. Balieu, N. Kringos, B. Birgisson, On the oxidative ageing mechanism and its effect on asphalt mixtures morphology, Mater. Struct. 48 (2014) 3113–3127. https://doi.org/10.1617/s11527-014-0385-5.

[37] B. Hofko, L. Porot, A.F. Cannone, L. Poulikakos, L. Huber, X. Lu, H. Grothe, K. Mollenhauer, FTIR spectral analysis of bituminous binders : reproducibility and impact of ageing temperature, Mater. Struct. 51 (2018). https://doi.org/10.1617/s11527-018-1170-7.

[38] L.D. Poulikakos, C.F. A, D. Wang, L. Porot, B. Hofko, Impact of asphalt aging temperature on chemomechanics, RSC Adv. 9 (2019) 11602–11613. https://doi.org/10.1039/C9RA00645A.

[39] P.R. Herrington, Thermal decomposition of asphalt sulfoxides, Fuel. 74 (1995) 1232–1235. https://doi.org/10.1016/0016-2361(95)00039-8.

[40] EN12607-1, Bitumen and bituminous binders. Determination of the resistance to hardening under the influence of heat and air–Part 1: RTFOT method, 2007.

[41] EN14769, Bitumen and Bituminous Binders. Accelerated Long-term Ageing Conditioning by a Pressure Ageing Vessel (PAV), 2012.

[42] K. Zhao, Y. Wang, F. Li, Influence of ageing conditions on the chemical property changes of asphalt binders, Road Mater. Pavement Des. (2019) 1–29. https://doi.org/10.1080/14680629.2019.1637771.

[43] F. Liu, Z. Zhou, X. Zhang, Y. Wang, On the linking of the rheological properties of asphalt binders exposed to oven aging and PAV aging, Int. J. Pavement Eng. 0 (2019) 1–10. https://doi.org/10.1080/10298436.2019.1608992.

[44] N.A. Al-Azri, S.H. Jung, K.M. Lunsford, A. Ferry, J.A. Bullin, R.R. Davison, C.J. Glover, Binder oxidative aging in Texas pavements: Hardening rates, hardening susceptibilities, and impact of pavement depth, in: Transp. Res. Rec., 2006: pp. 12–20. https://doi.org/10.3141/1962-02.

[45] J. Lamontagne, P. Dumas, V. Mouillet, J. Kister, Comparison by Fourier transform infrared (FTIR) spectroscopy of different ageing techniques : application to road bitumens, Fuel. 80 (2001) 483–488. https://doi.org/10.1016/S0016-2361(00)00121-6.

[46] G. Tarsi, A. Varveri, C. Lantieri, A. Scarpas, C. Sangiorgi, Effects of Different Aging Methods on Chemical and Rheological Properties of Bitumen, J. Mater. Civ. Eng. 30 (2018). https://doi.org/10.1061/(asce)mt.1943-5533.0002206.

[47] L.W. Corbett, R.E. Merz, Asphalt Binder Hardening in the Michigan Test Road After 18 Years of Service, Transp. Res. Rec. (1975) 27–34.

[48] E. Institute, IP 469/01: Determination of saturated, aromatic and polar Flame, compounds in petroleum products by thin layer chromatography and ionization detection, 2006.

[49] N. Sakib, A. Bhasin, N. Sakib, Measuring polarity-based distributions (SARA) of bitumen using simplified chromatographic techniques, Int. J. Pavement Eng. 8436 (2019) 1–28. https://doi.org/10.1080/10298436.2018.1428972.

[50] M. Paliukaitė, A. Vaitkus, A. Zofka, Evaluation of bitumen fractional composition depending on the crude oil type and production technology, in: 9th Int. Conf. Environ. Eng. ICEE 2014, 2014. https://doi.org/10.3846/enviro.2014.162.

[51] P. Mikhailenko, H. Baaj, Comparison of Chemical and Microstructural Properties of Virgin and Reclaimed Asphalt Pavement Binders and Their Saturate , Aromatic , Resin , and Asphaltene Fractions, Energy & Fuels. 33 (2019) 2633–2640. https://doi.org/10.1021/acs.energyfuels.8b03414.

[52] D. Lesueur, The colloidal structure of bitumen: Consequences on the rheology and on the mechanisms of bitumen modification, Adv. Colloid Interface Sci. 145 (2009) 42–82. https://doi.org/10.1016/j.cis.2008.08.011.

[53] P. Redelius, H. Soenen, Relation between bitumen chemistry and performance, Fuel. 140 (2015) 34–43. https://doi.org/10.1016/j.fuel.2014.09.044.

[54] D. Lesueur, Evidence of the Colloidal Structure of Bitumen, in: ISAP Int. Work. Chemo-Mechanics Bitum. Mater., 2009. https://doi.org/10.1016/j.cis.2008.08.011.

[55] A. Rosinger, Beiträge zur Kolloidchemie des Asphalts, Kolloid-Zeitschrift. 15 (1914) 177–179. https://doi.org/10.1007/BF01427821.

[56] F.J. Nellensteyn, The constitution of asphalt, J. Inst. Pet. Technol. 10 (1924) 311–323.

[57] J.M. Swanson, A Contribution to the Physical Chemistry of the Asphalts., J. Phys. Chem. 46 (1942) 141–150.

[58] J.P. Pfeiffer, R.N.J. Saal, Asphaltic bitumen as colloid system., J. Phys. Chem. 44 (1940) 139–149.

[59] J.P. Pfeiffer, The properties of asphaltic bitumen, (1950).

[60] C. Gaestel, R. Smadja, K.. Lamminan, Contribution à la connaissance des propriétés des bitumes routiers, Rev. Générale Des Routes Aérodromes. 466 (1971) 85–97.

[61] J.C. Petersen, R.E. Robertson, J.F. Branthaver, P.M. Harnsberger, J.J. Duvall, S.S. Kim, D.A. Anderson, D.W. Christiansen, H.U. Bahia, Binder characterization and evaluation: Volume 1, Rep. No. SHRP-A-367, Strateg. Highw. Res. Program, Natl. Res. Counc. Washington, DC. (1994).

[62] D. Christensen, DW Anderson, Rheological evidence concerning the molecular architecture of asphalt cements., in: Proc. Chem. Bitumen, Vol 2, Rome, Pp., 1991: pp. 568–95.

[63] P.G. Redelius, The structure of asphaltenes in bitumen, Road Mater. Pavement

Des. 7 (2006) 143–162. https://doi.org/10.1080/14680629.2006.9690062.

[64] B. Schuler, Y. Zhang, F. Liu, A.E. Pomerantz, A. Ballard, L. Gross, V. Pauchard, S. Banerjee, O.C. Mullins, Overview of Asphaltene Nanostructures and Thermodynamic Applications, (2020). https://doi.org/10.1021/acs.energyfuels.0c00874.

[65] O.C. Mullins, The Modified Yen Model, Energy & Fuels. (2010) 2179–2207. https://doi.org/10.1021/ef900975e.

[66] O.C. Mullins, H. Sabbah, J. Eyssautier, A.E. Pomerantz, L. Barré, A.B. Andrews, Y. Ruiz-Morales, F. Mostowfi, R. McFarlane, L. Goual, R. Lepkowicz, T. Cooper, J. Orbulescu, R.M. Leblanc, J. Edwards, R.N. Zare, Advances in asphaltene science and the Yen-Mullins model, in: Energy and Fuels, 2012: pp. 3986–4003. https://doi.org/10.1021/ef300185p.

[67] J. Eyssautier, P. Levitz, D. Espinat, J. Jestin, I. Grillo, L. Barr, Insight into Asphaltene Nanoaggregate Structure Inferred by Small Angle Neutron and X-ray Scattering, J. Phys. Chem. B. (2011) 6827–6837. https://doi.org/https://doi.org/10.1021/jp111468d.

[68] A. Ramm, M.C. Downer, N. Sakib, A. Bhasin, Morphology and kinetics of asphalt binder microstructure at gas, liquid and solid interfaces., J. Microsc. 276 (2019) 109–117. https://doi.org/10.1111/jmi.12842.

[69] G. Pipintakos, N. Hasheminejad, C. Lommaert, A. Bocharova, J. Blom, Application of Atomic Force (AFM), Environmental Scanning Electron (ESEM) and Confocal Laser Scanning Microscopy (CLSM) in bitumen: A review of the ageing effect, Micron. 147 (2021) 103083. https://doi.org/10.1016/j.micron.2021.103083.

[70] L. Loeber, O. Sutton, J. Morel, J.M. Valleton, G. Muller, New direct observations of asphalts and asphalt binders by scanning electron microscopy and atomic force microscopy, J. Microsc. 182 (1996) 32–39. https://doi.org/10.1046/j.1365-2818.1996.134416.x.

[71] A. Jäger, R. Lackner, C. Eisenmenger-Sittner, R. Blab, Identification of four material phases in bitumen by atomic force microscopy, Road Mater. Pavement Des. 5 (2004) 9–24. https://doi.org/10.1080/14680629.2004.9689985.

[72] G. Pipintakos, J. Blom, H. Soenen, W. Van den bergh, Coupling AFM and CLSM to investigate the effect of ageing on the bee structures of bitumen, Micron. 151 (2021) 103149. https://doi.org/10.1016/j.micron.2021.103149.

[73] H. Fischer, L.D. Poulikakos, J.-P. Planche, P. Das, J. Grenfell, Challenges While Performing AFM on Bitumen, in: N. Kringos, B. Birgisson, D. Frost, L. Wang (Eds.), Multi-Scale Model. Charact. Infrastruct. Mater., Springer Netherlands, Dordrecht, 2013: pp. 89–98. https://doi.org/10.1007/978-94-007-6878-9_7.

[74] H. Soenen, J. Besamusca, H.R. Fischer, L.D. Poulikakos, J. Planche, P.K. Das,

Laboratory investigation of bitumen based on round robin DSC and AFM tests, Mater. Struct. (2014). https://doi.org/10.1617/s11527-013-0123-4.

[75] J. Blom, H. Soenen, N. Van den Brande, W. Van den bergh, New evidence on the origin of 'bee structures' on bitumen and oils, by atomic force microscopy (AFM) and confocal laser scanning microscopy (CLSM), Fuel. 303 (2021) 121265. https://doi.org/10.1016/j.fuel.2021.121265.

[76] J. Blom, H. Soenen, A. Katsiki, N. Van Den Brande, H. Rahier, W. Van den bergh, Investigation of the bulk and surface microstructure of bitumen by atomic force microscopy, Constr. Build. Mater. 177 (2018) 158–169. https://doi.org/10.1016/j.conbuildmat.2018.05.062.

[77] X. Lu, P. Redelius, Compositional and Structural Characterization of Waxes Isolated from Bitumens, Energy & Fuels. 20 (2006) 653–660. https://doi.org/10.1021/ef0503414.

[78] L. Carbognani, L. DeLima, M. Orea, U. Ehrmann, Studies on large crude oil alkanes. II. Isolation and chracterization of aromatic waxes and waxy asphlatnes., Pet. Sci. Technol. 18 (2000) 607–634. https://doi.org/10.1080/10916460008949863.

[79] M. Djabourov, J. Volle, M. Kane, J. Lechaire, G. Frebourg, Morphology of paraffin crystals in waxy crude oils cooled in quiescent conditions and under flow, Fuel. 82 (2003) 127–135. https://doi.org/10.1016/S0016-2361(02)00222-3.

[80] P. Claudy, J.M. Letoffe, G.N. King, J.P. Plancke, Characterization of asphalts cements by thermomicroscopy and differential scanning calorimetry: correlation to classic physical properties, Fuel Sci. Technol. Int. 10 (1992) 735–765. https://doi.org/10.1080/08843759208916019.

[81] X. Lu, M. Langton, P. Olofsson, P. Redelius, Wax morphology in bitumen, J. Mater. Sci. 40 (2005) 1893–1900. https://doi.org/10.1007/s10853-005-1208-4.

[82] P. Claudy, G.N. King, Caractérisation des bitumes routiers par analyse calorimétrique différentielle (ACD). Analyse thermo-optique (ATO). Corrélation entre propriétés physiques et résultats ACD, Bull. Liaison Des Lab. Des Ponts Chaussees. (1992).

[83] P.M. Claudy, J.M. Létoffé, D. Martin, J.P. Planche, Thermal behavior of asphalt cements, Thermochim. Acta. 324 (1998) 203–213.

[84] R. Hajj, S. Young, An analysis of theoretical and empirical relationships between two asphalt binder cracking parameters, Road Mater. Pavement Des. 22 (2021) S180–S196. https://doi.org/10.1080/14680629.2021.1906734.

[85] S. Weigel, D. Stephan, Relationships between the chemistry and the physical properties of bitumen, Road Mater. Pavement Des. 19 (2018) 1636–1650. https://doi.org/10.1080/14680629.2017.1338189.

[86] S.-C. Huang, H. Di Benedetto, Advances in Asphalt Materials, 2015. https://doi.org/978-0-08-100269-8.

[87] R. Tauste, F. Moreno-Navarro, M. Sol-Sánchez, M.C. Rubio-Gámez, Understanding the bitumen ageing phenomenon: A review, Constr. Build. Mater. 192 (2018) 593–609. https://doi.org/10.1016/j.conbuildmat.2018.10.169.

[88] A. Dony, L. Ziyani, I. Drouadaine, S. Pouget, S. Faucon-Dumont, D. Simard, V. Mouillet, J.E. Poirier, T. Gabet, L. Boulange, A. Nicolai, C. Gueit, 1, MURE National Project : FTIR spectroscopy study to assess ageing of asphalt mixtures, in: 6th Eurasphalt Eurobitume Congr., 2016. https://doi.org/dx.doi.org/10.14311/EE.2016.154.

[89] F.J. Ortega, F.J. Navarro, M. Jasso, L. Zanzotto, Physicochemical softening of a bituminous binder by a reactive surfactant (dodecenyl succinic anhydride , DSA), Constr. Build. Mater. 222 (2019) 766–775. https://doi.org/10.1016/j.conbuildmat.2019.06.117.

[90] L.D. Poulikakos, S. Santos, M. Bueno, S. Kuentzel, M. Hugener, M.N. Partl, Influence of short and long term aging on chemical , microstructural and macro-mechanical properties of recycled asphalt mixtures, Constr. Build. Mater. 51 (2014) 414–423. https://doi.org/10.1016/j.conbuildmat.2013.11.004.

[91] Q. Qin, J.F. Schabron, R.B. Boysen, M.J. Farrar, Field aging effect on chemistry and rheology of asphalt binders and rheological predictions for field aging, Fuel. 121 (2014) 86–94. https://doi.org/10.1016/j.fuel.2013.12.040.

[92] J. Mirwald, S. Werkovits, I. Camargo, D. Maschauer, B. Hofko, H. Grothe, Investigating bitumen long-term-ageing in the laboratory by spectroscopic analysis of the SARA fractions, Constr. Build. Mater. 258 (2020) 119577. https://doi.org/10.1016/j.conbuildmat.2020.119577.

[93] A. Margaritis, H. Soenen, E. Fransen, G. Pipintakos, G. Jacobs, J. Blom, W. Van den bergh, Identification of ageing state clusters of reclaimed asphalt binders using principal component analysis (PCA) and hierarchical cluster analysis (HCA) based on chemo-rheological parameters, Constr. Build. Mater. 244 (2020) 118276. https://doi.org/10.1016/j.conbuildmat.2020.118276.

[94] C.J. Glover, R.R. Davison, C.H. Domke, Y. Ruan, P. Juristyarini, D.B. Knorr, S.H. Jung, Development of a New Method for Assessing Asphalt Binder Durability with Field Validation, Texas Dep. Transp. 1872 (2005) 1–334. https://static.tti.tamu.edu/tti.tamu.edu/documents/0-1872-2.pdf.

[95] D.J. Mensching, N.H. Gibson, A. Andriescu, G.M. Rowe, J. Sias, Assessing the Applicability of Rheological Parameters to Evaluate Modified Binders, in: Int. Soc. Asph. Pavements Symp. 53rd Petersen Asph. Res. Conf., 2016: pp. 1–12. https://www.researchgate.net/publication/299804374.

[96] D. Lesueur, M.D. Elwardany, J.P. Planche, D. Christensen, G.N. King, Impact of the asphalt binder rheological behavior on the value of the ΔTc parameter, Constr. Build. Mater. 293 (2021) 123464. https://doi.org/10.1016/j.conbuildmat.2021.123464.

[97] G. Pipintakos, H. Soenen, H.Y.V. Ching, C. Vande Velde, S. Van Doorslaer, F. Lemière, A. Varveri, W. Van den bergh, Exploring the oxidative mechanisms of bitumen after laboratory short- and long-term ageing, Constr. Build. Mater. 289 (2021) 123182. https://doi.org/10.1016/j.conbuildmat.2021.123182.

[98] L.W. Corbett, Relationship between composition and physical properties of asphalt and discussion, in: Assoc. Asph. Paving Technol. Proc, 1970.

[99] X. Yu, N.A. Burnham, S. Granados-Focil, M. Tao, Bitumen's microstructures are correlated with its bulk thermal and rheological properties, Fuel. 254 (2019) 115509.

[100] M.A. Poirier, H. Sawatzky, Changes in chemical component type composition and effect on rheological properties of asphalts, Prepr. Symp. 35 (1990) 301–307.

[101] G. Thenoux, C.A. Bell, J.E. Wilson, Evaluation of physical and fractional properties of asphalt and their interrelationship, Transp. Res. Rec. (1988) 82–97.

[102] B. Hofko, L. Eberhardsteiner, J. Füssl, H. Grothe, F. Handle, M. Hospodka, D. Grossegger, S.N. Nahar, A.J.M. Schmets, A. Scarpas, Impact of maltene and asphaltene fraction on mechanical behavior and microstructure of bitumen, Mater. Struct. Constr. 49 (2016) 829–841. https://doi.org/10.1617/s11527-015-0541-6.

[103] C. Wang, W. Xie, B.S. Underwood, Fatigue and healing performance assessment of asphalt binder from rheological and chemical characteristics, Mater. Struct. Constr. 51 (2018) 1–12. https://doi.org/10.1617/s11527-018-1300-2.

[104] A.T. Pauli, J.F. Branthaver, Relationships between asphaltenes, heithaus compatibility parameters, and asphalt viscosity, Pet. Sci. Technol. 16 (1998) 1125–1147. https://doi.org/10.1080/10916469808949827.

[105] Z. Huang, S. Zheng, H.S. Fogler, Wax deposition: experimental characterizations, theoretical modeling, and field practices, CRC Press, 2015.

[106] H. Ding, S.A.M. Hesp, Quantification of crystalline wax in asphalt binders using variable-temperature Fourier-transform infrared spectroscopy, Fuel. 277 (2020) 118220. https://doi.org/10.1016/j.fuel.2020.118220.

[107] X. Lu, P. Redelius, Effect of bitumen wax on asphalt mixture performance, Constr. Build. Mater. 21 (2007) 1961–1970. https://doi.org/https://doi.org/10.1016/j.conbuildmat.2006.05.048.

[108] H. Soenen, P. Redelius, The effect of aromatic interactions on the elasticity of bituminous binders, Rheol. Acta. 53 (2014) 741–754. https://doi.org/10.1007/s00397-014-0792-0.

[109] H. Ding, Y. Qiu, A. Rahman, Low-Temperature Reversible Aging Properties of Selected Asphalt Binders Based on Thermal Analysis, J. Mater. Civ. Eng. 31 (2019) 4018402. https://doi.org/10.1061/(ASCE)MT.1943-5533.0002625.

[110] R. Jing, Ageing of bituminous materials: Experimental and numerical characterization, (2019).

[111] P. Bruice, Organic Chemistry 4th Edition, (2019).

[112] A. Stoll , S.; Schweiger, EasySpin, a comprehensive software package for spectral simulation and analysis in EPR, J. Magn. Reson. 178 (2006) 42–55. https://doi.org/https://doi.org/10.1016/j.jmr.2005.08.013.

[113] V. Thiel, P. Sjövall, Time-of-flight secondary ion mass spectrometry (TOF-SIMS): Principles and practice in the biogeosciences, RSC Detect. Sci. 2015-Janua (2015) 122–170. https://doi.org/10.1039/9781782625025-00122.

[114] N. Kim, Chemical Characterization of Gilsonite Bitumen, J. Pet. Environ. Biotechnol. 05 (2014). https://doi.org/10.4172/2157-7463.1000193.

[115] J.C. Poveda, D.R. Molina, Journal of Petroleum Science and Engineering Average molecular parameters of heavy crude oils and their fractions using NMR spectroscopy, J. Pet. Sci. Eng. 84–85 (2012) 1–7. https://doi.org/10.1016/j.petrol.2012.01.005.

[116] S. Werkovits, M. Bacher, J. Theiner, T. Rosenau, H. Grothe, Multi-spectroscopic characterization of bitumen and its polarity-based fractions, Constr. Build. Mater. 352 (2022) 128992. https://doi.org/https://doi.org/10.1016/j.conbuildmat.2022.128992.

[117] L. J. O'Neil, P.E. Heckelman, C.B. Koch, K.J. Roman, The Merck Index, an Encyclopedia of Chemicals, Drugs, and Biologicals, Merck Research Laboratories; 14th Edition, 2006.

[118] C.O. Rossi, P. Caputo, G. De Luca, L. Maiuolo, S. Eskandarsefat, C. Sangiorgi, 1H-NMR Spectroscopy : A Possible Approach to Advanced Bitumen Characterization for Industrial and Paving Applications, Appl. Sci. 8 (2018). https://doi.org/10.3390/app8020229.

[119] M.H.J. Koch, J. Bordas, X-ray diffraction and scattering on disordered systems using synchrotron radiation, Nucl. Instruments Methods Phys. Res. 208 (1983) 461–469. https://doi.org/10.1016/0167-5087(83)91169-9.

[120] B. Goderis, H. Reynaers, R. Scherrenberg, V.B.F. Mathot, M.H.J. Koch, Temperature Reversible Transitions in Linear Polyethylene Studied by TMDSC and Time-Resolved, Temperature-Modulated WAXD/SAXS, Macromolecules.

34 (2001) 1779–1787. https://doi.org/10.1021/ma001759y.

[121] G. Binnig, C.F. Quate, C. Gerbe, Atomic Force Microscope, Phys. Rev. Lett. 56 (1986).

[122] P.K. Das, H. Baaj, S. Tighe, N. Kringos, Atomic force microscopy to investigate asphalt binders: a state-of-the-art review, Road Mater. Pavement Des. 17 (2016) 693–718. https://doi.org/10.1080/14680629.2015.1114012.

[123] V. Bellitto, Atomic Force Microscopy - Imaging, Measuring and Manipulating Surfaces at the Atomic Scale, BoD–Books on Demand, 2012. https://doi.org/10.5772/2673.

[124] A. García, J.P. Aguiar-Moya, J. Salazar-Delgado, A. Baldi-Sevilla, L.G. Loría-Salazar, Methodology for estimating the modulus of elasticity of bitumen under different aging conditions by AFM, Road Mater. Pavement Des. 20 (2019) S332–S346. https://doi.org/10.1080/14680629.2019.1588152.

[125] H. Ban, P. Karki, Y.-R. Kim, Nanoindentation test integrated with numerical simulation to characterize mechanical properties of rock materials, J. Test. Eval. 42 (2014) 787–796. https://doi.org/10.1520/JTE20130035.

[126] R.G. Allen, D.N. Little, A. Bhasin, Structural Characterization of Micromechanical Properties in Asphalt Using Atomic Force Microscopy, J. Mater. Civ. Eng. 24 (2012) 1317–1327. https://doi.org/10.1061/(asce)mt.1943-5533.0000510.

[127] S.N. Nahar, A.J.M. Schmets, A. Scarpas, G. Schitter, Temperature and thermal history dependence of the microstructure in bituminous materials, Eur. Polym. J. 49 (2013) 1964–1974. https://doi.org/10.1016/j.eurpolymj.2013.03.027.

[128] D. Nečas, P. Klapetek, Gwyddion: an open-source software for SPM data analysis, Open Phys. 10 (2012) 181–188.

[129] B.V.R. Tata, B. Raj, Confocal laser scanning microscopy: Applications in material science and technology, Bull. Mater. Sci. 21 (1998) 263–278. https://doi.org/10.1007/BF02744951.

[130] W.B. Amos, J.G. White, How the confocal laser scanning microscope entered biological research, Biol. Cell. 95 (2003) 335–342. https://doi.org/10.1016/s0248-4900(03)00078-9.

[131] M. Minsky, Memoir on inventing the confocal scanning microscope, Scanning. 10 (1988) 128–138. https://doi.org/10.1002/sca.4950100403.

[132] N.S. Claxton, T.J. Fellers, M.W. Davidson, Laser Scanning Confocal Microscopy (LSCM), SpringerReference. (2011). https://doi.org/10.1007/springerreference_67032.

[133] S.W. Paddock, Principles and practices of laser scanning confocal microscopy, Mol. Biotechnol. 16 (2000) 127–149. https://doi.org/10.1385/MB:16:2:127.

[134] H. Li, W.K. Wan, Investigation of the asphaltene precipitation process from cold

lake bitumen by confocal scanning laser microscopy, in: SPE Int. Heavy Oil Symp., Society of Petroleum Engineers, 1995: pp. 709–740. https://doi.org/10.2523/30321-ms.

[135] R.J. Mikula, V.A. Munoz, Characterization of emulsions and suspensions in the petroleum industry using cryo-SEM and CLSM, Colloids Surfaces A Physicochem. Eng. Asp. 174 (2000) 23–36. https://doi.org/10.1016/S0927-7757(00)00518-5.

[136] S. Bearsley, A. Forbes, R. G. Haverkamp, Direct observation of the asphaltene structure in paving-grade bitumen using confocal laser-scanning microscopy, J. Microsc. 215 (2004) 149–155. https://doi.org/10.1111/j.0022-2720.2004.01373.x.

[137] E.M. A., S. Saman, M.L. N., H. Marwa, D.W. H., D. Samer, New Approach to Recycling Asphalt Shingles in Hot-Mix Asphalt, J. Mater. Civ. Eng. 24 (2012) 1403–1411. https://doi.org/10.1061/(ASCE)MT.1943-5533.0000520.

[138] D. Großegger, Microstructural aging of bitumen, in: 6th Eurasphalt Eurobitume Congr., 2017. https://doi.org/10.14311/ee.2016.135.

[139] S.J. Rozeveld, E. Eugene Shin, A. Bhurke, L. France, L.T. Drzal, Network morphology of straight and polymer modified asphalt cements, Microsc. Res. Tech. 38 (1997) 529–543. https://doi.org/10.1002/(SICI)1097-0029(19970901)38:5<529::AID-JEMT11>3.0.CO;2-O.

[140] Y.-J. Lee, L.M. France, M.C. Hawley, The Effect of Network Formation on the Rheological Properties of SBR Modified Asphalt Binders, Rubber Chem. Technol. 70 (1997) 256–263. https://doi.org/10.5254/1.3538430.

[141] D. Kaya, A. Topal, T. McNally, Correlation of processing parameters and ageing with the phase morphology of styrene-butadiene-styrene block co-polymer modified bitumen, Mater. Res. Express. 6 (2019) 105309. https://doi.org/10.1088/2053-1591/ab349c.

[142] H. Yin, Y. Zhang, Y. Sun, W. Xu, D. Yu, H. Xie, R. Cheng, Performance of hot mix epoxy asphalt binder and its concrete, Mater. Struct. 48 (2015) 3825–3835. https://doi.org/10.1617/s11527-014-0442-0.

[143] J. Gong, Y. Liu, Q. Wang, Z. Xi, J. Cai, G. Ding, H. Xie, Performance evaluation of warm mix asphalt additive modified epoxy asphalt rubbers, Constr. Build. Mater. 204 (2019) 288–295. https://doi.org/10.1016/j.conbuildmat.2019.01.197.

[144] Y. Liu, Z. Xi, J. Cai, H. Xie, Laboratory investigation of the properties of epoxy asphalt rubber (EAR), Mater. Struct. 50 (2017) 219. https://doi.org/10.1617/s11527-017-1089-4.

[145] Y. Liu, J. Zhang, R. Chen, J. Cai, Z. Xi, H. Xie, Ethylene vinyl acetate copolymer modified epoxy asphalt binders: phase separation evolution and mechanical

properties, Constr. Build. Mater. 137 (2017) 55–65. https://doi.org/10.1016/j.conbuildmat.2017.01.081.

[146] Y. Jiang, Y. Liu, J. Gong, C. Li, Z. Xi, J. Cai, H. Xie, Microstructures, thermal and mechanical properties of epoxy asphalt binder modified by SBS containing various styrene-butadiene structures, Mater. Struct. 51 (2018) 86. https://doi.org/10.1617/s11527-018-1217-9.

[147] Y. Liu, J. Zhang, Y. Jiang, C. Li, Z. Xi, J. Cai, H. Xie, Investigation of secondary phase separation and mechanical properties of epoxy SBS-modified asphalts, Constr. Build. Mater. 165 (2018) 163–172. https://doi.org/10.1016/j.conbuildmat.2018.01.032.

[148] D.W. Christensen, D.A. Anderson, Interpretation of dynamic mechanical test data for paving grade asphalt cements (with discussion), J. Assoc. Asph. Paving Technol. 61 (1992).

[149] L. Garcia Cucalon, F. Kaseer, E. Arámbula-Mercado, A. Epps Martin, N. Morian, S. Pournoman, E. Hajj, The crossover temperature: significance and application towards engineering balanced recycled binder blends, Road Mater. Pavement Des. 20 (2019) 1391–1412. https://doi.org/10.1080/14680629.2018.1447504.

[150] R. Zhang, J.E. Sias, E. V Dave, Correlating Laboratory Conditioning with Field Aging for Asphalt using Rheological Parameters, Transp. Res. Rec. 2674 (2020) 393–404. https://doi.org/10.1177/0361198120915894.

[151] D.W. Christensen, D.A. Anderson, G.M. Rowe, Relaxation spectra of asphalt binders and the Christensen–Anderson rheological model, Road Mater. Pavement Des. 18 (2017) 382–403. https://doi.org/10.1080/14680629.2016.1267448.

[152] W.S. Mogawer, T. Bennert, A. Austerman, C. Ericson, AAPT symposium: Investigating the aging mitigation capabilities of rejuvenators in high RAP mixtures using black space diagrams, binder rheology and mixture tests, in: Asph. Paving Technol. Assoc. Asph. Paving Technol. Tech. Sess., Association of Asphalt Paving Technologist, 2015: pp. 705–738.

[153] D. Wang, A.C. Falchetto, C. Riccardi, L. Poulikakos, B. Hofko, L. Porot, M.P. Wistuba, H. Baaj, P. Mikhailenko, K.H. Moon, Investigation on the combined effect of aging temperatures and cooling medium on rheological properties of asphalt binder based on DSR and BBR, Road Mater. Pavement Des. 20 (2019) S409–S433.

[154] R.M. Anderson, G.N. King, D.I. Hanson, P.B. Blankenship, Evaluation of the relationship between asphalt binder properties and non-load related cracking, Asph. Paving Technol. Assoc. Asph. Paving Technol. Tech. Sess. 80 (2011) 615–662.

[155] D. Christensen, D. Mensching, G. Rowe, R.M. Anderson, A. Hanz, G. Reinke, D.

Anderson, Past, present, and future of asphalt binder rheological parameters: Synopsis of 2017 Technical Session 307 at the 96th Annual Meeting of the Transportation Research Board, Transp. Res. Circ. (2019).

[156] T.W. Kennedy, G.A. Huber, E.T. Harrigan, R.J. Cominsky, C.S. Hughes, H. Von Quintus, J.S. Moulthrop, Superior performing asphalt pavements (Superpave): The product of the SHRP asphalt research program, (1994).

[157] A.M. Hung, A. Goodwin, E.H. Fini, Effects of water exposure on bitumen surface microstructure, Constr. Build. Mater. 135 (2017) 682–688. https://doi.org/10.1016/j.conbuildmat.2017.01.002.

[158] J. Mirwald, D. Nura, B. Hofko, Recommendations for handling bitumen prior to FTIR spectroscopy, Mater. Struct. 55 (2022) 26. https://doi.org/10.1617/s11527-022-01884-1.

[159] H. Soenen, X. Lu, O.-V. Laukkanen, Oxidation of bitumen: molecular characterization and influence on rheological properties, Rheol. Acta. 55 (2016) 315–326. https://doi.org/10.1007/s00397-016-0919-6.

[160] H.R. Fischer, E.C. Dillingh, C.G.M. Hermse, Applied Surface Science On the interfacial interaction between bituminous binders and mineral surfaces as present in asphalt mixtures, Appl. Surf. Sci. 265 (2013) 495–499. https://doi.org/10.1016/j.apsusc.2012.11.034.

[161] S.N. Nahar, A.J.M. Schmets, C. Kasbergen, G. Schitter, A. Scarpas, Self-healing of bituminous materials by damage reversal at the microstructural scale, in: Proc. 94th Annu. Meet. Transp. Res. Board, 2015: pp. 11–15.

[162] F. Mastoras, A. Varveri, M. van Tooren, S. Erkens, Effect of mineral fillers on ageing of bituminous mastics, Constr. Build. Mater. 276 (2021) 122215. https://doi.org/https://doi.org/10.1016/j.conbuildmat.2020.122215.

[163] Y. Cui, C.J. Glover, J. Braziunas, H. Sivilevicius, Further exploration of the pavement oxidation model Diffusion-reaction balance in asphalt, Constr. Build. Mater. 161 (2018) 132–140. https://doi.org/10.1016/j.conbuildmat.2017.11.095.

[164] R. Karlsson, U. Isacsson, Laboratory studies of diffusion in bitumen using markers, J. Mater. Sci. 38 (2003) 2835–2844. https://doi.org/10.1023/A:1024476217060.

[165] R. Han, X. Jin, C.J. Glover, Petroleum Science and Technology Oxygen Diffusivity in Asphalts and Mastics, Pet. Sci. Technol. (2013) 37–41. https://doi.org/10.1080/10916466.2011.559506.

[166] J.H. Tannous, A. De Klerk, Quantification of the Free Radical Content of Oilsands Bitumen Fractions, Energy & Fuels. 33 (2019) 7083–7093. https://doi.org/10.1021/acs.energyfuels.9b01115.

[167] X. Lu, P. Sjövall, H. Soenen, M. Andersson, Microstructures of bitumen observed by environmental scanning electron microscopy (ESEM) and chemical analysis using time-of- flight secondary ion mass spectrometry (TOF-SIMS), Fuel. 229 (2018) 198–208. https://doi.org/10.1016/j.fuel.2018.05.036.

[168] M.F. Libert, I. Walczak, Effect of radio-oxidative ageing and pH on the release of soluble organic matter from bitumen, in: Int. Conf. Sci. Res. Back-End Fuel Cycle 21. Century, France, 2000: pp. 1–4.

[169] G. Boczkaj, A. Przyjazny, M. Kamin, Characteristics of volatile organic compounds emission profiles from hot road bitumens, Chemosphere. 107 (2014) 23–30. https://doi.org/10.1016/j.chemosphere.2014.02.070.

[170] I.-H. Wang, J.L. Boucher, R.A. Romine, R.D. Rowlett, G.-D. Lei, Oxidation chemistry in asphalt, Fuel Sci. Technol. Int. 11 (1993) 1–28. https://doi.org/http://dx.doi.org/10.1080/08843759308916056.

[171] L. Ma, A. Varveri, R. Jing, S. Erkens, Comprehensive review on the transport and reaction of oxygen and moisture towards coupled oxidative ageing and moisture damage of bitumen, Constr. Build. Mater. 283 (2021) 122632. https://doi.org/10.1016/j.conbuildmat.2021.122632.

[172] I. Gabrielle do Nascimento Camargo, B. Hofko, J. Mirwald, G. Hinrich, Effect of Thermal and Oxidative Aging on Asphalt Binders Rheology and Chemical Composition, Materials (Basel). 13 (2020) 4438. https://doi.org/doi:10.3390/ma13194438.

[173] J.F. Branhaver, J.C. Petersen, R.E. Robertson, J.J. Duvall, S.S. Kim, P.M. Harnsberger, T. Mill, E.K. Ensley, F.A. Barbour, J.F. Schabron, SHRP-A-368 Binder Characterization and Evaluation Volume 2 : Chemistry, Washington, DC, 1993.

[174] J. Mirwald, B. Hofko, G. Pipintakos, J. Blom, H. Soenen, Comparison of microscopic techniques to study the diversity of the bitumen microstructure, Micron. 159 (2022) 103294. https://doi.org/10.1016/j.micron.2022.103294.

[175] L.C. Michon, D.A. Netzel, T.F. Turner, D. Martin, J.P. Planche, A 13C NMR and DSC study of the amorphous and crystalline phases in asphalts, Energy and Fuels. 13 (1999) 602–610. https://doi.org/10.1021/ef980184r.

[176] I.N. Frolov, E.S. Okhotnikova, M.A. Ziganshin, A.A. Firsin, Cold crystallization event on DSC heating curves of bitumen, J. Therm. Anal. Calorim. 147 (2022) 5269–5278. https://doi.org/10.1007/s10973-021-10908-x.

[177] V.B.F. Mathot, Calorimetry and thermal analysis of polymers, Hanser Publishers, 1994.

[178] C.W. Bunn, D.R. Holmes, Chain configurations in crystals of simple linear polymers, Discuss. Faraday Soc. 25 (1958) 95–103. https://doi.org/10.1039/DF9582500095.

[179] J. Masson, V. Leblond, J. Margeson, Bitumen morphologies by phase-detection atomic force microscopy, J. Microsc. 221 (2006) 17–29. https://doi.org/10.1111/j.1365-2818.2006.01540.x.

[180] S. Liu, A. Peng, S. Zhou, J. Wu, W. Xuan, W. Liu, Evaluation of the ageing behaviour of waste engine oil-modified asphalt binders, Constr. Build. Mater. 223 (2019) 394–408. https://doi.org/10.1016/j.conbuildmat.2019.07.020.

[181] S. Wu, L. Pang, L. Mo, Y. Chen, G. Zhu, Influence of aging on the evolution of structure , morphology and rheology of base and SBS modified bitumen, Constr. Build. Mater. 23 (2009) 1005–1010. https://doi.org/10.1016/j.conbuildmat.2008.05.004.

[182] W. Zhang, L. Zou, Z. Jia, F. Wang, Y. Li, P. Shi, Effect of thermo-oxidative ageing on nano-morphology of bitumen, Appl. Sci. 9 (2019). https://doi.org/10.3390/app9153027.

[183] L.M. Rebelo, J.S. De Sousa, A.S. Abreu, M.P.M.A. Baroni, A.E.V. Alencar, S.A. Soares, J. Mendes Filho, J.B. Soares, Aging of asphaltic binders investigated with atomic force microscopy, Fuel. 117 (2014) 15–25. https://doi.org/10.1016/j.fuel.2013.09.018.

[184] A. Koyun, J. Büchner, M.P. Wistuba, H. Grothe, Rheological, spectroscopic and microscopic assessment of asphalt binder ageing, Road Mater. Pavement Des. 23 (2022) 80–97. https://doi.org/10.1080/14680629.2020.1820891.

[185] M. Xu, J. Yi, Z. Pei, D. Feng, Y. Huang, Y. Yang, Generation and evolution mechanisms of pavement asphalt aging based on variations in surface structure and micromechanical characteristics with AFM, Mater. Today Commun. 12 (2017) 106–118. https://doi.org/10.1016/j.mtcomm.2017.07.006.

[186] H.L. Zhang, H.C. Wang, J.Y. Yu, Effect of aging on morphology of organo-montmorillonite modified bitumen by atomic force microscopy, J. Microsc. 242 (2011) 37–45. https://doi.org/10.1111/j.1365-2818.2010.03435.x.

[187] A. Chen, G. Liu, Y. Zhao, J. Li, Y. Pan, J. Zhou, Research on the aging and rejuvenation mechanisms of asphalt using atomic force microscopy, Constr. Build. Mater. 167 (2018) 177–184. https://doi.org/10.1016/j.conbuildmat.2018.02.008.

[188] P.E.Y. Wang, K. Zhao, C. Glover, L. Chen, Y. Wen, D. Chong, Effects of aging on the properties of asphalt at the nanoscale, Constr. Build. Mater. 80 (2015) 244–254. https://doi.org/10.1016/j.conbuildmat.2015.01.059.

[189] H.L. Zhang, J.Y. Yu, Z.G. Feng, L.H. Xue, S.P. Wu, Effect of aging on the morphology of bitumen by atomic force, J. Microsc. 246 (2012) 11–19. https://doi.org/10.1111/j.1365-2818.2011.03578.x.

[190] J.P. Aguiar-Moya, J. Salazar-Delgado, A. García, A. Baldi-Sevilla, V. Bonilla-Mora, L.G. Loría-Salazar, Effect of ageing on micromechanical properties of bitumen

by means of atomic force microscopy, Road Mater. Pavement Des. 18 (2017) 203–215. https://doi.org/10.1080/14680629.2017.1304249.

[191] Y. Yuan, X. Zhu, L. Chen, Relationship among cohesion , adhesion , and bond strength : From multi-scale investigation of asphalt-based composites subjected to laboratory-simulated aging, Mater. Des. 185 (2020) 108272. https://doi.org/10.1016/j.matdes.2019.108272.

[192] J. Zhu, R. Balieu, X. Lu, N. Kringos, Microstructure evaluation of polymer-modified bitumen by image analysis using two-dimensional fast Fourier transform, Mater. Des. 137 (2018) 164–175.

[193] A.R. Pathak, M. Pandey, S. Rautaray, Application of Deep Learning for Object Detection, Procedia Comput. Sci. 132 (2018) 1706–1717. https://doi.org/https://doi.org/10.1016/j.procs.2018.05.144.

[194] J. Redmon, A. Farhadi, Yolov3: An incremental improvement, ArXiv Prepr. ArXiv1804.02767. (2018).

[195] A.A.-K.H. Abu-Ein, A novel methodology for digital removal of periodic noise using 2D fast Fourier transforms, Contemp. Eng. Sci. 3 (2014) 103–116.

[196] G. Pipintakos, H.Y.V. Ching, U. Mühlich, H. Soenen, S. Van Doorslaer, P. Sjövall, A. Varveri, C. Vande Velde, X. Lu, Experimental Validation of the Dual-Oxidation Routes in Bituminous Binders, in: H. Di Benedetto, H. Baaj, E. Chailleux, G. Tebaldi, C. Sauzéat, S. Mangiafico (Eds.), RILEM Bookseries, Springer International Publishing, Cham, 2022: pp. 903–909. https://doi.org/10.1007/978-3-030-46455-4_115.

[197] U. Mühlich, G. Pipintakos, C. Tsakalidis, Modelling of Oxidative Ageing in Bitumen Using Thermodynamics of Irreversible Processes (TIP): Potential and Challenges BT - Proceedings of the RILEM International Symposium on Bituminous Materials, in: H. Di Benedetto, H. Baaj, E. Chailleux, G. Tebaldi, C. Sauzéat, S. Mangiafico (Eds.), Springer International Publishing, Cham, 2022: pp. 1359–1365.

[198] U. Mühlich, Towards a continuum thermodynamics framework for mechanism-based modelling of oxidative ageing in bitumen, Int. J. Pavement Eng. 21 (2020) 1419–1428. https://doi.org/10.1080/10298436.2018.1546859.

[199] J. Read, D. Whiteoak, The Shell Bitumen Handbook, 5th edition, Thomas Telford, 2003. https://doi.org/10.1680/sbh.32200.

[200] J.W.H. Oliver, Changes in the Chemical Composition of Australian Bitumens, Road Mater. Pavement Des. 10 (2009) 569–586. https://doi.org/10.1080/14680629.2009.9690214.

[201] J. Vidal, Thermodynamics, Editions OPHRYS, 1971.

[202] M. Pekař, I. Samohýl, The thermodynamics of linear fluids and fluid mixtures,

Springer, 2014.

[203] Diana Paola powers, Characterization and Asphaltene Precipitation Modeling of Native and Reacted Crude Oils, Department of chemical and petroleum engineering, Calgary, Albert, 2014.

[204] K. Akbarzadeh, H. Alboudwarej, W.Y. Svrcek, H.W. Yarranton, A generalized regular solution model for asphaltene precipitation from n-alkane diluted heavy oils and bitumens, Fluid Phase Equilib. (2005). https://doi.org/10.1016/j.fluid.2005.03.029.

RESEARCH DISSEMINATION

Publications related to the dissertation

1. Georgios Pipintakos, H.Y. Vincent Ching, Hilde Soenen, Peter Sjövall, Uwe Mühlich, Sabine Van Doorslaer, Aikaterini Varveri, Wim Van den bergh and Xiaohu Lu. Experimental investigation of the oxidative ageing mechanisms in bitumen. Construction and Building materials (2020).

2. Georgios Pipintakos, Hilde Soenen, Hong Yue Vincent Ching, Christophe Vande Velde, Sabine Van Doorslaer, Filip Lemière, Aikaterini Varveri and Wim Van den bergh. Exploring the oxidative mechanisms of bitumen after laboratory short- and long-term ageing. Construction and building materials (2021).

3. Georgios Pipintakos, Navid Hasheminejad, Caitlin Lommaert, Anastassiya Bocharova and Johan Blom. Application of Atomic Force (AFM), Environmental Scanning Electron (ESEM) and Confocal Laser Scanning Microscopy (CLSM) in bitumen : a review of the ageing effect. Micron (2021).

4. Georgios Pipintakos, Johan Blom, Hilde Soenen and Wim Van den bergh. Coupling AFM and CLSM to investigate the effect of ageing on the bee structures of bitumen. Micron (2021).

5. Georgios Pipintakos, Hilde Soenen, Bart Goderis, Johan Blom and Xiaohu Lu. Crystallinity of bitumen via WAXD and DSC and its effect on the surface microstructure. Crystals (2022).

6. Georgios Pipintakos, Caitlin Lommaert, Aikaterini Varveri and Wim Van den bergh. Do chemistry and rheology follow the same laboratory ageing trends in bitumen? Materials and Structures (2022).

7. Georgios Pipintakos, H.Y. Vincent Ching, Uwe Mühlich, Hilde Soenen, Sabine Van Doorslaer, Peter Sjövall, Aikaterini Varveri, Christophe Vande Velde and Xiaohu Lu. Experimental validation of the dual-oxidation routes in bituminous binders. ISBM 2020: Proceedings of the RILEM International Symposium on Bituminous Materials (2021).

8. Georgios Pipintakos, Lili Ma, Aikaterini Varveri, Ruxin Jing, Hilde Soenen and Wim Van den bergh. Oxidation kinetics and diffusivity in bitumen. AM3P conference, Hong Kong (under review).

9. Uwe Muehlich, **Georgios Pipintakos** and Christos Tsakalidis. Mechanism-based diffusion-reaction modelling for predicting the influence of SARA composition and ageing stage on spurt completion time and diffusivity in bitumen. Construction and building materials (2021).

10. Uwe Muehlich, **Georgios Pipintakos** and Christos Tsakalidis. Modelling of Oxidative Ageing in Bitumen Using Thermodynamics of Irreversible Processes (TIP): Potential and Challenges. ISBM 2020: Proceedings of the RILEM International Symposium on Bituminous Materials (2021).

11. Xiaohu Lu, Hilde Soenen, Peter Sjövall and **Georgios Pipintakos**. Analysis of asphaltenes and maltenes before and after long-term aging of bitumen. Fuel (2021).

12. Navid Hasheminejad, **Georgios Pipintakos,** Cedric Vuye, Thomas De Kerf, Taher Ghalandari, Johan Blom and Wim Van den bergh. Utilizing deep learning and advanced image processing techniques to investigate the microstructure of a waxy bitumen. Construction and building materials (2021).

Co-authored publications during the doctoral trajectory

13. Alexandros Margaritis, Hilde Soenen, Erik Fransen, **Georgios Pipintakos**, Geert Jacobs, Johan Blom and Wim Van den bergh. Identification of ageing state clusters of reclaimed asphalt binders using principal component analysis (PCA) and hierarchical cluster analysis (HCA) based on chemo-rheological parameters. Construction and Building materials (2020).

14. Alexandros Margaritis, **Georgios Pipintakos,** Geert Jacobs, David Hernando, Mats Bruynen, Jeroen Bruurs and Wim Van den bergh. Evaluating the role of recycling rate and rejuvenator on the chemo-rheological properties of reclaimed polymer-modified binders. Road Materials and Pavement Design (2021).

15. Alexandros Margaritis, **Georgios Pipintakos,** Aikaterini Varveri, Geert Jacobs, Navid Hasheminejad, Johan Blom and Wim Van den bergh. Towards an enhanced fatigue evaluation of bituminous mortars. Construction and Building materials (2021)**.**

16. Alexandros Margaritis, Navid Hasheminejad, **Georgios Pipintakos,** Geert Jacobs, Johan Blom and Wim Van den bergh. The impact of reclaimed asphalt rate on the healing potential of bituminous mortars and mixtures. International Journal of Pavement Engineering (2021).

17. Alexandros Margaritis, Geert Jacobs, **Georgios Pipintakos,** Johan Blom, and Wim Van den bergh. Fatigue Resistance of Bituminous Mixtures and Mortars Containing High Reclaimed Asphalt Content. Materials (2020).

18. I. Rocha Segundo, S Jr. Landi, A. Margaritis, **Georgios Pipintakos**, E. Freitas, C. Vuye, J. Blom, S. Tytgat, S. Denys and J. Carneiro. Physicochemical and Rheological Properties of a Transparent Asphalt Binder Modified with Nano-TiO2. Nanomaterials (2021).

19. S. R. Omranian, Hamzah, M.O., **Georgios Pipintakos,** W. Van den bergh, C. Vuye and M.R.M. Hasan. Effects of Short-Term Aging on the Compactibility and Volumetric Properties of Asphalt Mixtures Using the Response Surface Method. Sustainability (2020)**.**

20. Thomas De Kerf, **Georgios Pipintakos**, Zohreh Zahiri, Steve Vanlanduit and Paul Scheunders. Identification of Corrosion Minerals Using Shortwave Infrared Hyperspectral Imaging. Sensors (2022).

21. Johannes Mirwald, Bernhard Hofko, **Georgios Pipintakos**, Johan Blom and Hilde Soenen. Comparison of Microscopic Techniques to study the Diversity of the Bitumen Microstructure. Micron (2022).

22. Alexandros Margaritis, **Georgios Pipintakos,** Li Ming Zhang, Geert Jacobs, Cedric Vuye, Johan Blom and Wim Van den Bergh. Introducing an Improved Testing Method to Evaluate the Fatigue Resistance of Bituminous Mortars. ISBM 2020: Proceedings of the RILEM International Symposium on Bituminous Materials (2021).

23. Seyed Reza Omranian, Michiel Geluykens, Myrthe Van Hal, Navid Hasheminejad, Iran Rocha Segundo, **Georgios Pipintakos**, Siegfried Denys, Tom Tytgat, Elisabete Fraga Freitas, Joaquim Carneiro, Sammy Verbruggen and Cedric Vuye. Assessing the Potential of Titanium Dioxide Application on Asphalt Pavements to Degrade Soot Deposition. Construction and Building materials (2022).

24. Dheeraj Adwani, Anand Sreeram, **Georgios Pipintakos**, Johannes Mirwald, Yudi Wang, Ramez Hajj, Ruxin Jing and Amit Bhasin. Interpreting the Effectiveness of Antioxidants to Increase the Resilience of Asphalt Binders: First of its Kind Global Interlaboratory Study. Construction and Building materials (under review).

25. Geert Jacobs, **Georgios Pipintakos**, Xander Van den Buijs and Wim Van den bergh. Chemo-rheological equivalence of bitumen between different lab ageing

procedures: from binder to mixture. Road Materials and Pavement Design, Special Issue: EATA 2023 (under review).

26. Michael Elwardany, Nusnin Akter, Panos Apostolidis, Terry Arnold, Mike Aurilio, Lorena Garcia-Cucalon, Hamzeh Haghshenas, Kamal Hossain, David Mensching, Johannes Mirwald, Virginie Mouillet, **Georgios Pipintakos**, Laurent Porot, Nibert Saltibus, Pezhouhan Tavassoti-Kheiry, Sandra Weigel, Gayle King, Jean-Pascal Planche, Gerald Reinke and Jack Youtcheff. A Review of FT-IR Spectroscopy for Asphalt Bitumen Engineers and Scientists. Transportation Research Board E-Circular (under review).